

UNIVERSITY OF OSLO
Department of
Geosciences

**Is there a positive
feedback between
Arctic stratus and
Arctic sea ice
changes?**

Master thesis in
Geosciences
Meteorology and
oceanography

Mari Fenn
Kristiansen

1st June 2015



*Rows and flows of angel hair
and ice cream castles in the air
and feather canyons
everywhere,
I've looked at clouds that way.*

JONI MITCHELL

Abstract

The influence of diminishing sea ice and increased aerosol number concentration on low clouds over the Beaufort Sea, north of Canada and Alaska, has been investigated by use of a formulation of the Weather Research and Forecasting (WRF) model called the Advanced Research WRF (ARW).

The model was run for the five first days of September 2012, of which the discussion focuses on days 1 and 5. There the first day is most like an off line run, representing near instantaneous changes in clouds and radiation due to ice removal and aerosol number concentration increase, whereas by the last day the atmosphere has had time to adapt to the changes that were implemented at the start of the first day.

The near instantaneous changes as a consequence of removal of sea ice were negative changes in upward shortwave radiation (SW) at the top of the atmosphere (TOA) and downward SW at the surface. There were also signs of new clouds forming, indicated by a small increase in liquid water path (LWP) 0.23 g/m^2 . As the atmosphere has had time to adapt to the changed sea ice extent, new clouds have formed and precipitated, also causing other clouds to precipitate. Thus leading to an average decrease in LWP, -2.3 g/m^2 .

The near instantaneous changes following an increase in aerosol number concentration are increases in LWP and cloud droplet number concentration (CDNC), and a decrease in cloud droplet size. These more numerous and smaller droplets increase the albedo of the clouds, known as the first indirect effect. The increase in LWP indicates that the clouds are also denser and longer lived, which is known as the second indirect effect. Both these effects reduce the downward SW at the surface, giving a change of -9.2 W/m^2 . They also increase the SW up at TOA by 7.3 W/m^2 . As the atmosphere has had time to adapt, the cooling effect from reduced downward SW is evident in the surface temperature and heat fluxes, as they decrease.

In this study, initially high LWP ($40\text{-}300 \text{ g/m}^2$) weakens the enhancement of LW down at the surface, since the clouds sometimes are saturated with respect to LW. Thus a positive feedback between changes in Arctic stratus and changes in Arctic sea ice extent may not be confirmed.

Acknowledgements

First of all I want to thank my main supervisor Jón Egill Kristjánsson for an interesting project and for the opportunity to come and work at NCAR for a couple of weeks. Getting to both work with clouds, which I love, and go to the U.S.A. for the first time makes a happy student. I had a great time over there and am thankful that I could join him and his wife for both hikes and meals. I also want to thank my other supervisor Kari Alterskjær for her "poking" and setting deadlines and pushing me for the past few months – thank you for being a great motivator! I greatly appreciate the guidance and criticism that they have both given me throughout this project. I have learned a lot from both of them, and hope I get the opportunity to work with them again in the future.

Thank you so much to Anne Claire Fuillioux for helping me with setting up and getting started with WRF, and to both her and Kjell Andresen for help with technical problems during my work with this thesis. Thanks should also be given to Kjetil Schanke Aas for always taking time to answer any stupid WRF-related questions I might have had.

Thanks also to Gregory Thompson whom Jón Egill and I met with in Boulder, for meeting with us and for answering all my e-mails about running the new aerosol-aware microphysics scheme in WRF.

These past two years in the master program at MetOs have been very enjoyable, despite all the stress. Thanks to Marta and Helle especially, for all their positiveness.

I would also like to thank friends and family, for their encouragement, and for rooting for me during my work with this thesis.

Last, but not least, I would like to thank Henrik Andersen Sveinsson, my love and technical helper, for bearing with me through the last few weeks I worked on this thesis.

Oslo, 1st June 2015
Mari Fenn Kristiansen

Contents

1	Introduction	9
1.1	Main goal	10
1.2	Area description	10
1.3	Background	11
1.4	Structure of the thesis	12
2	Theory of clouds and radiation	13
2.1	Arctic stratus	13
2.2	Cloud effects on radiation	14
2.2.1	The Cloud – a gray body	14
2.2.2	Cloud emissivity	15
2.2.3	Cloud optical depth	15
2.2.4	Cloud albedo	16
2.2.5	Cloud droplet effective radius	16
2.2.6	Liquid water content and path	17
2.2.7	Ice water path	18
2.2.8	Dependence of cloud albedo and cloud emissivity on liquid water path and droplet size	19
2.3	Aerosols and clouds	20
2.3.1	The first indirect effect	21
2.3.2	The second indirect effect	22
3	Model and methods	25
3.1	Description of the WRF-ARW Modeling System	25
3.2	Model setup	29
3.2.1	Choices of physics in the model	30
3.3	Model runs	33
3.3.1	Input data	34
3.3.2	Manipulation of input files	34
3.4	Processing the model output	35

4 Results and discussion	37
4.1 The control run	37
4.2 Removed sea ice	48
4.2.1 Day 1	48
4.2.2 Day 5	55
4.3 Increased aerosol number concentration	63
4.3.1 Day 1	63
4.3.2 Day 5	70
4.4 Removed sea ice <u>and</u> increased aerosol	75
4.4.1 Day 1	75
4.4.2 Day 5	80
5 Summary and concluding remarks	87
Bibliography	91

Chapter 1

Introduction

Since 1979, the areal extent of Arctic sea ice in early autumn has shrunk by 80% according to satellite data [NSIDC, 2015]. According to new satellite data sets, the decline appears to be particularly rapid after 2000 [Wu & Lee, 2012]. The dramatic reduction in sea ice extent may have contributed strongly to the rapid warming of the Arctic, due to increases in latent and sensible heat fluxes from the ocean [Screen & Simmonds, 2010], and due to the sea ice–albedo feedback [Curry *et al.*, 1995]. The rapid warming of the Arctic compared to the global mean has become known as "Arctic amplification" [Graversen *et al.*, 2008], but the reasons for this amplification are not fully understood.

Globally, low clouds have a net cooling effect by reflecting solar radiation, due to their high albedo. Clouds also absorb and emit terrestrial longwave radiation, which has a warming effect at the surface. In the Arctic the intensity of incoming solar radiation is lower than at lower latitudes, and the warming effect of downwelling longwave radiation overpowers the cooling effect of reflecting shortwave radiation, since there is less to reflect. Thus low clouds have a net warming effect in the Arctic [Shupe & Intrieri, 2004]. The Arctic cloud cover is dominated by low layered clouds (stratus) [Curry *et al.*, 1996], therefore the climate effect of low clouds in the Arctic is important to study.

Decreasing sea ice extent could lead to an increase in the aerosol number concentrations in the area where ice has retreated. The open sea surface itself would lead to an increase in release of sea salt, primary organic matter and DMS (di-methyl-sulfide) to the lower atmosphere. The lack of sea ice would also increase the likelihood that the sea could be used for shipping, which would further increase the aerosol number concentration.

The enhancement of evaporation from the ocean with diminishing sea ice and the increase in aerosol number concentration from open water and shipping could lead to denser and longer-lived low clouds in the area of sea ice retreat. The hypothesis of this thesis is that these clouds would then

have a different radiative effect, and by that influence the further retreat of sea ice.

1.1 Main goal

Studies by Eastman & Warren [2010] using visual cloud reports from the Arctic together with surface and satellite observations, and by Kay & Gettelman [2009] and Palm *et al.* [2010] using lidar and radar observations have confirmed that the low-cloud amount over the Arctic oceans varies inversely with sea ice amount. This means that there is an increase in cloud amount when there is less sea ice. Therefore, one can envisage a positive feedback between shrinking sea ice (due to global warming), enhanced evaporation, increased effective cloud cover, enhanced downwelling longwave radiation and warming surface temperatures. In this thesis I will study if the aforementioned low-cloud amounts are also denser and more persistent, and could lead to an enhanced warming and reduced sea ice amount, also known as a positive feedback.

The effect of increase in aerosol concentrations from shipping and open water, and the effect of enhanced evaporation from open water are studied separately and combined. The main goal is to find whether more open ocean and/or larger aerosol loads will lead to changes in clouds that could enhance downwelling longwave radiation and decrease upwelling shortwave radiation, both of which have a warming effect at the surface, and therefore have a positive feedback enhancing warming of the Arctic.

The findings in my thesis have been achieved by use of a formulation of the Weather Research and Forecasting (WRF) model called the Advanced Research WRF (ARW). Used with a recently developed scheme (by Greg Thompson [Thompson & Eidhammer, 2014]) for cloud micro physics and aerosols and their effects on radiation.

1.2 Area description

The study area is in the Arctic and covers the Beaufort Sea and small parts of Alaska and Canada (figure 1.1).

There are a few reasons for choosing this as the study area. First it is in the Arctic, and sea ice is present there in autumn, even in 2012 when there was record low sea ice extent (eg. National Snow and Ice Data Center [NSIDC, 2015]). Also it has been subject to field campaigns: Surface Heat Budget of the Arctic Ocean (SHEBA) [Uttal *et al.*, 2002], First International Satellite Cloud Climatology Project Regional Experiment Arctic cloud Experiment (FIRE ACE) [Curry *et al.*, 2000], Mixed-Phase Arctic Cloud Experiment (M-PACE) [Verlinde *et al.*, 2007] and more. There are a few studies on Arctic clouds that include this area and data from some

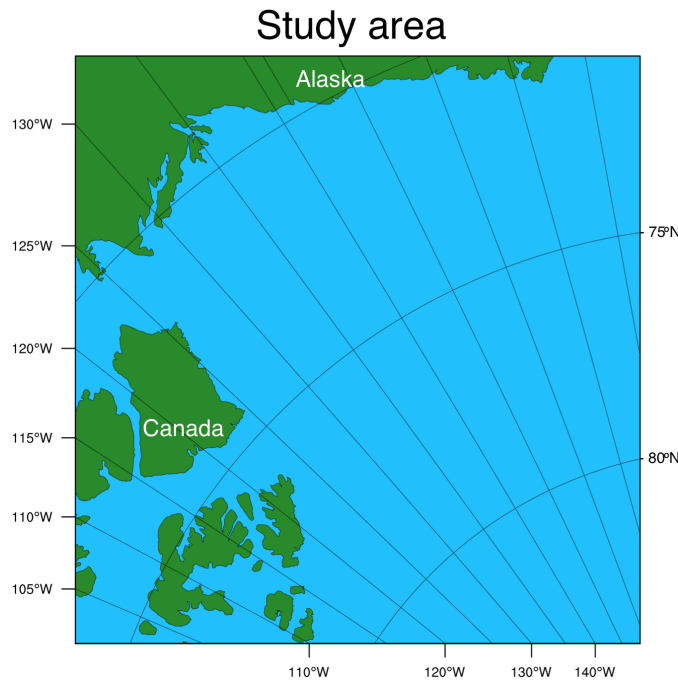


Figure 1.1: An overview of the study area. The bottom right corner is the northernmost point and the y-axes show longitude and latitude to the left and right, respectively.

of the aforementioned field campaigns. Some of these provide parts of the science basis for my study and selection of literature. Quite a few studies are based on satellite data analysis, and some of these are mentioned in the next section as background and motivation for my thesis.

1.3 Background

A study by Schweiger *et al.* [2008] investigated the connection between sea ice variability and cloud cover over the Arctic seas during autumn. They analyzed the ERA-40 re-analysis products and some satellite data sets. They found that that sea ice retreat was linked to a decrease in low-level (surface to ~ 1.9 km) cloud amount and an increase in mid-level (~ 1.9 to 6.1 km) clouds. They state that the decrease in static stability and deepening of the atmospheric boundary layer following ice retreat contribute to the rise in cloud level.

Vavrus *et al.* [2010] investigated the behaviour of clouds during intervals of rapid sea ice loss in the Arctic in the 21st century. The study was done by use of the Community Climate System Model (CCSM3). They conclude that cloud changes accelerate rapid loss of sea ice in autumn.

Kay & Gettelman [2009] combined satellite data sets and complementary atmosphere reanalysis data to study the Arctic cloud and atmospheric structure during summer and early Autumn over the years 2006-2008. This covers the (at the time) record low sea ice extent from 2007. In contrast to the study by Schweiger *et al.* [2008] they found more low-level clouds. The re-analysis used in Schweiger *et al.* [2008] was for the time period 1964-2001, which is not the same period as Kay & Gettelman [2009] studied.

Eastman & Warren [2010] analyzed visual cloud reports from the Arctic for year-to-year variations and found that following a low-ice September there would be enhanced low cloud cover in autumn.

A study by Palm *et al.* [2010] using satellite and lidar data found that areas of open water were associated with greater polar cloud fraction.

A common uncertainty and missing link in a few of these studies is that they did not look at liquid water content, effective radius and other parameters affecting the radiative properties of the clouds. In this study I want to look in to how these properties are influenced by the changing sea ice, and if changes in the clouds enhance sea ice melting.

1.4 Structure of the thesis

In the next chapter, Chapter 2, the theory of clouds and radiation is presented. This is followed by Chapter 3 where I explain which model and tools I have used and how I have worked with them to get the results presented in Chapter 4. A summary of the results and concluding remarks are included in the last chapter, Chapter 5.

Chapter 2

Theory of clouds and radiation

In this thesis the term shortwave (SW) refers to the wavelength band that carries the energy associated with solar radiation, including the visible spectrum and the shorter waves in the near infrared ($\lambda < 4\mu m$) [Wallace & Hobbs, 2006]. Longwave (LW) refers to wavelengths emitted by the Earth-atmosphere system (terrestrial radiation) including the longer waves in the near infrared and wavelengths in the infrared spectrum ($\lambda > 4\mu m$) [Wallace & Hobbs, 2006].

In this chapter a brief overview of clouds in the Arctic, with focus on stratus, is presented. This is followed by a description of how cloud properties can influence radiation and lastly a section on aerosol-cloud interactions.

2.1 Arctic stratus

The clouds studied in this thesis are low (up to about 1800 m) stratus clouds, in the Arctic. Stratus clouds are low layered clouds that form when extensive areas of stable air are lifted. They are normally between 0.5 and 1 km thick, and can be several km wide [Aguado & Burt, 2010]. The largest amounts of low stratus clouds in the Arctic are over the ocean [Klein & Hartmann, 1993].

According to Klein & Hartmann [1993], stratus in the Arctic basin peaks during summer at nearly 62%, while during the winter season the stratus only accounts for 18% of the cloud cover. This leads them to conclude that the seasonal cycle of stratus in the Arctic is driven by the temperature cycle and thereby moisture content in the atmosphere, rather than the static stability.

Winter in the Arctic (polar night) is completely dark and free of incoming SW radiation. The Arctic summer on the other hand has sunlight 24 hours a day. The amount of solar radiation reaching the surface is limited by the

optical depth of the atmosphere it passes through. Since the Arctic is far north, the incoming solar radiation is at a high zenith angle, and less SW reaches the surface than at lower latitudes.

Details on radiation follows below, but in short: Low clouds reflect SW radiation due to their high albedo. This has a cooling effect at the surface. These clouds also absorb and emit LW radiation, both up and down, and the downwelling LW radiation has a warming effect at the surface. Globally, low clouds have a net cooling effect at the surface, due to high amounts of incoming solar radiation and lower zenith angles. In the Arctic, the annual mean incoming solar radiation is low, the zenith angle is high and so is the surface albedo. It is only in the summer that reflection of solar radiation outweighs the downwelling LW emitted by the clouds [Curry *et al.*, 1996], therefore the warming effect of downwelling LW radiation dominates. Hence, as mentioned in Chapter 1, low clouds in the Arctic have a net warming effect at the surface [Shupe & Intrieri, 2004].

The air in the Arctic is very stable in winter (polar night), when the surface temperature is lower than that of the atmosphere above. The air is also clean since there are not many sources for pollution. In Autumn, the sea ice extent reaches a minimum after the summer melt and leaves open water to influence the properties of low clouds. According to Curry *et al.* [1996], clouds in the Arctic are mostly optically thin and low-lying. The maximum value of liquid water content measured in Arctic stratus over the Beaufort Sea during June 1980 was 0.5 g/m^3 , and the liquid water paths ranged from 11 to 117 g/m^2 for low clouds. Effective radii ranged from 3.6 to $11.4 \mu\text{m}$, with 7.5 being the average value for low clouds [Curry *et al.*, 1996]. These cloud properties in the clouds play a crucial role in influencing the radiation fluxes reaching the surface. Relevant cloud radiative properties are presented in the next section.

2.2 Cloud effects on radiation

The cloud microphysical properties that determine the cloud radiative properties include: the amount of condensed water, the size and shape of the cloud particles, and if the particles are liquid or ice [Curry *et al.*, 1996].

2.2.1 The Cloud – a gray body

Stefan–Boltzmanns law states that the flux density emitted by a blackbody is proportional to the fourth power of the absolute temperature (eg. [Liou, 2002]).

$$F = \epsilon_\lambda \sigma T^4 \quad (2.1)$$

where $\epsilon_\lambda = 1$ is the emissivity for a blackbody at wavelength λ . F (W/m^2) is the flux density emitted by the body, and $\sigma = 5.67 \cdot 10^{-8} \text{ J m}^{-2} \text{ sec}^{-1} \text{ K}^{-4}$

is the Stefan–Boltzmann constant. A blackbody both absorbs and emits at maximum, and the ratio of absorption and emission to the maximum is given by the absorptivity, α_λ , and the emissivity, ϵ_λ , for wavelength λ . Kirchoff's law states that the absorptivity and emissivity for a medium are equal for each wavelength in the longer wavelength spectra: $\alpha_\lambda = \epsilon_\lambda$ [Liou, 2002]. Kirchoff's law is only applicable for LW radiation at local thermodynamic equilibrium in the lower 60-70 km of the atmosphere. Since this study focuses on the lowest 2 km of the troposphere, the law is applicable.

A cloud can be defined as a gray body, which means that α_λ and ϵ_λ are not at their maximum, $\alpha_\lambda = \epsilon_\lambda < 1$ [Liou, 2002].

2.2.2 Cloud emissivity

The cloud LW emissivity, ϵ , is a measure of the emittance of LW radiation by the cloud. From Stefan-Boltzmann's law (equation 2.1) the flux density emitted by a body depends on the body's temperature and its emissivity. The cloud longwave emissivity is [Liou, 1992]

$$\epsilon = 1 - \exp(-k_v^c \text{LWP}) \quad (2.2)$$

where k_v^c is the mass absorption coefficient of cloud particles, which is inversely proportional to the droplet size [Alterskjaer *et al.*, 2010], meaning that a decrease in droplet size increases ϵ . LWP is the liquid water path, which is the vertically integrated amount of water. The LWP is further explained in section 2.2.6. Equation 2.1 shows that if one assumes constant cloud temperature, the flux density emitted by the cloud increases with increasing ϵ , which increases with increasing LWP. Arctic stratus are often sufficiently thin to not have an emissivity of unity (hence they are gray bodies). If they are thicker than 350 m, though, they do have emissivity close to unity [Herman, 1980]. Dependence of ϵ on LWP and droplet size will be further explained in section 2.2.8.

2.2.3 Cloud optical depth

Cloud optical depth (or cloud optical thickness), τ , is a measure of the cumulative depletion that a beam of radiation directed straight downward (zenith angle $\theta = 0$) would experience in passing through a defined cloud layer. Of the incident SW radiation on a cloud with optical depth τ , a fraction $e^{-\tau}$ is not scattered or absorbed and is defined as the transmissivity of the cloud [Wallace & Hobbs, 2006]. The remaining $1 - e^{-\tau}$ has been scattered one or more times, or absorbed, in passing through the cloud layer. The cloud optical depth is given by [Twomey, 1977]

$$\tau = \int_0^h k_E dz = \pi \int_0^h \int_0^\infty r^2 Q_E(r/\lambda) n(r, z) dr dz \quad (2.3)$$

at height z above cloud base for a cloud of depth h , containing $n(r)dr$ drops with radius in the interval $(r, r + dr)$ per cubic centimeter (cm^{-3}). $Q_E(r/\lambda)$ is the extinction efficiency and k_E is the extinction coefficient [Twomey, 1977]. The extinction efficiency is a measure of how well a particle removes the incident radiation, either by scattering or absorption. In the visible, for $\lambda \ll r$, $Q_E \approx 2$ is a good approximation [Hobbs, 1993], giving the simpler expression

$$\tau = 2\pi N r_e^2 h \quad (2.4)$$

where it is assumed that the cloud droplet radius can be approximated by the effective radius, r_e , defined in section 2.2.5.

2.2.4 Cloud albedo

In section 2.2.3 it was stated that the incident SW radiation on a cloud layer is either transmitted, scattered or absorbed. The scattered radiation is scattered by single droplets, and the single-scattering albedo, $\bar{\omega}$, is the fraction of energy that is not absorbed in a single-scattering event. $\bar{\omega}$ can to a good approximation be assumed equal to 1, which means that the absorption of SW is negligible for cloud water. When the single-scattering albedo is taken to unity, the albedo (or reflectance) of a cloud layer is given by [Hobbs, 1993]:

$$A = \frac{(1 - g)\tau}{1 + (1 - g)\tau} = \frac{1 - g}{\frac{1}{\tau} + (1 - g)} \quad (2.5)$$

The cloud albedo, A , is then a function of the SW optical depth of a cloud, τ , and the asymmetry factor, g . The asymmetry factor gives the direction of scattered radiation by the cloud, and is given by $g = \cos \theta$ where θ is the scattering angle. g is a power-averaged value of the cosine of the scattering angle [Twomey, 1974]. $g = 1$ indicates pure forward scattering and $g = -1$ indicates pure back-scattering. According to Twomey, $g = 0.8$ or 0.9 for warm clouds, which means that most of the scattered energy is scattered forward.

2.2.5 Cloud droplet effective radius

The cloud droplet effective radius determines important radiative properties of a cloud, cloud albedo (A) and cloud emissivity (ϵ) [Hansen & Travis, 1974], and is therefore of particular interest.

The cloud droplet effective radius is a mean of the size distribution of cloud droplets, weighted by the droplet cross section. The effective radius, r_e , may be written

$$r_e = \frac{\int r^3 n(r) dr}{\int r^2 n(r) dr} \quad (2.6)$$

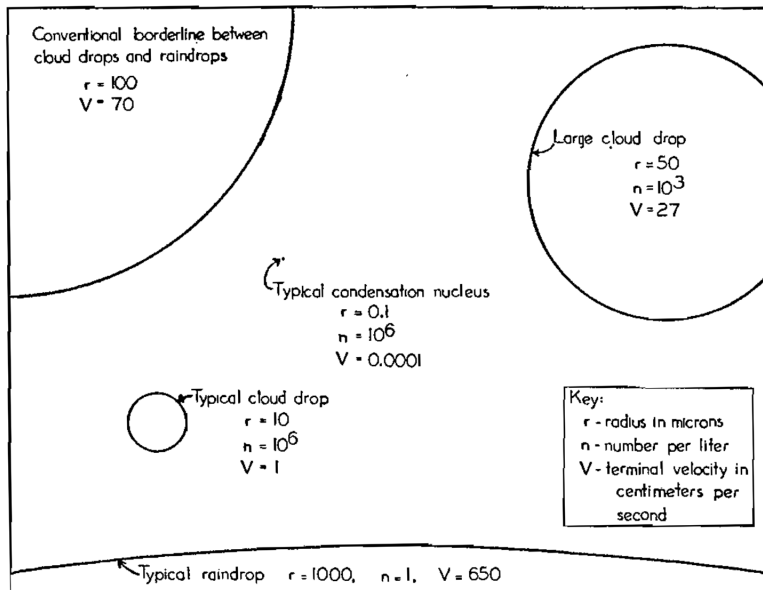


Figure 2.1: Typical sizes of cloud condensation nuclei (CCN), cloud droplet, large cloud droplet, borderline between cloud droplet and raindrop and typical size of raindrop. From [McDonald, 1958].

It can be seen from equation 2.4 that a decrease in r_e when N and h is kept constant decreases the optical depth of the cloud. Whereas an increase in r_e increases the cloud optical depth. It has already been established from equation 2.5 that a decrease (increase) in the cloud optical depth leads to a decrease (increase) in the cloud albedo A . The effect of r_e on ϵ is through k_v^c , where a decrease in r_e increases k_v^c and thereby increases ϵ (see equation 2.2).

The effective radius of a cloud droplet is typically on the order of a few micro meters μm . The typical size of a cloud droplet is depicted in figure 2.1. The figure also includes typical sizes of cloud condensation nuclei (CCN), large droplet, borderline between cloud droplet and raindrop and typical size of a raindrop.

2.2.6 Liquid water content and path

The amount of condensed water can be expressed by the liquid water content (LWC) in the cloud, often presented with units g m^{-3} , and is proportional to the cloud droplet number concentration (CDNC), and the cloud particle size. From Rogers & Yau [1989] the total number of droplets can be expressed by

$$N = \int n(r)dr \quad (2.7)$$

where N is the CDNC (cm^{-3}), and $n(r)$ is the number of droplets with radius in the interval $(r, r + dr)$. If the radius is approximated to be the mean volume radius, \bar{r} , the LWC for spherical droplets can be written

$$\text{LWC} = \int \rho_l \frac{4}{3} \pi r^3 n(r) dr \quad (2.8)$$

$$= \frac{4}{3} \pi \rho_l \int r^3 n(r) dr \quad (2.9)$$

$$= \frac{4}{3} \pi \rho_l \bar{r}^3 \int n(r) dr \quad (2.10)$$

$$= \frac{4}{3} \pi \rho_l \bar{r}^3 N \quad (2.11)$$

where the last equation shows the proportionality of LWC to the cloud droplet number concentration N , and to \bar{r} . ρ_l is the density of liquid water. Knowing the effective radius from equation 2.6, it is preferred to express the LWC as a function of that. The effective radius r_e and the mean volume radius \bar{r} are related by

$$r_e = \kappa \bar{r} \quad (2.12)$$

where $\kappa = 1.14$ for continental clouds and $\kappa = 1.08$ for maritime clouds [Martin *et al.*, 1994]. If one assumes a κ of unity the LWC may be written

$$\text{LWC} = \pi \rho_l r_e^3 N \quad (2.13)$$

Another common measure of condensed water is the liquid water path (LWP). If the LWC is integrated over a column, from the base to the top, it gives the LWP of that column.

$$\text{LWP} = \int_{base}^{top} \text{LWC} dz \quad (2.14)$$

The LWP is the column of liquid water in a cloud and is usually expressed in g m^{-2} .

2.2.7 Ice water path

Clouds do not always consist of just liquid water, they can also consist of ice. The amount of ice in a cloud for a given ice crystal size distribution is given by the ice water content (IWC) Liou [2002]

$$\text{IWC} = \int V \rho_i n(L) dL \quad (2.15)$$

where L is the maximum dimension of an ice crystal, V is the volume, ρ_i is the density of ice and $n(L)$ is the ice-crystal size distribution. As for the water droplets the cloud optical depth, τ , and mean effective crystal size,

D_e , are related through

$$\tau \approx \text{IWP}(c + b/D_e) \quad (2.16)$$

where IWP denotes the ice water path $\text{IWP} = \text{IWC} \cdot h$ for a layer of thickness h , and $c \approx -6.656 \times 10^{-3}$ and $b \approx 3.686$ for ice columns [Liou, 2002]. Equation 2.16 clearly shows that an increase in the IWP increases the cloud optical depth (when D_e is kept constant), which in turn, according to equation 2.5, increases the cloud albedo. The opposite is obvious for D_e ; when D_e increases, the optical depth decreases, provided the IWP is unchanged, which in turn decreases A .

2.2.8 Dependence of cloud albedo and cloud emissivity on liquid water path and droplet size

What effect a change in LWP has on incoming and outgoing radiation can be seen when the cloud optical depth is expressed as a function of LWP. Recall the cloud optical depth for SW radiation from equation 2.4 and rewrite it to get the CDNC (N) on the left side

$$N = \frac{\tau}{2\pi r_e^2 h} \quad (2.17)$$

If the equation for LWC, equation 2.13, is also rewritten to get N on the left side, like so

$$N = \frac{3\text{LWC}}{4\pi\rho_l r_e^3} \quad (2.18)$$

the cloud optical depth in the visible (τ) can be written as a function of LWP and r_e :

$$\frac{\tau}{2\pi r_e^2 h} = \frac{3\text{LWC}}{4\pi\rho_l r_e^3} \quad (2.19)$$

$$\tau = \frac{2\pi r_e^2 h 3\text{LWC}}{4\pi\rho_l r_e^3} \quad (2.20)$$

$$\tau = \frac{3\text{LWC} \cdot h}{2\rho_l r_e} \quad (2.21)$$

$$\tau = \frac{3\text{LWP}}{2\rho_l r_e} \quad (2.22)$$

Where $\text{LWC} \cdot h \approx \text{LWP}$. It is now clear that, if the droplet size is constant, an increase in the LWP increases the optical depth of a cloud, τ . An increase in τ would make the denominator in equation 2.5 for the cloud albedo, A , smaller and thereby increase the cloud albedo. An increase in A also means a reduction in SW radiation reaching the surface. In that way, an increase in LWP would have a cooling effect on the surface. But, the LW

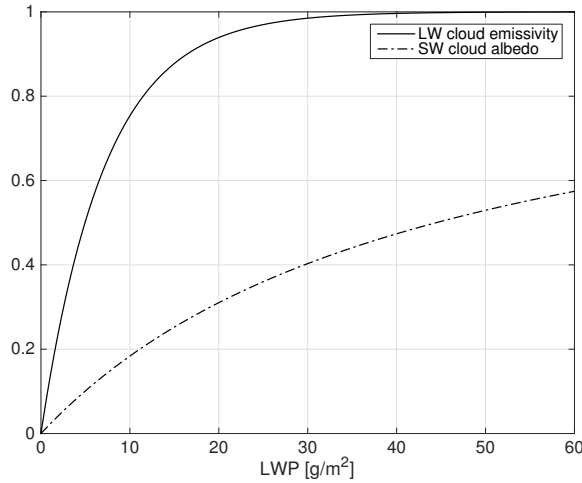


Figure 2.2: Cloud LW emissivity and SW albedo as a function of liquid water path (LWP), for clouds containing no ice.

radiation must also be considered. A change in LWP changes the cloud emissivity. Equation 2.2 shows that ϵ increases (decreases) with increasing (decreasing) LWP. This means that an increase in LWP would increase the flux density emitted by the cloud, following Stefan-Boltzmann's law from equation 2.1, and have a warming effect on the surface. Thus, a change in LWP gives opposite effects for short and long wavelengths. It is important to mention that the same effect is evident from keeping the LWP constant and decreasing r_e . This in turn increases τ , and thereby A – the cooling effect, but it also gives the warming effect through increasing ϵ , as described in section 2.2.5.

In figure 2.2 both SW cloud albedo, A , and the LW cloud emissivity, ϵ , are shown as functions of the LWP for ice-free clouds. It is based on equations 2.2, 2.5 and 2.22, where $k_v^c = 0.14$, $g = 0.85$, $\rho_l = 1000\text{kg/m}^3$ and $r_e = 10\mu\text{m}$ which is a typical cloud droplet radius according to figure 2.1. A cloud emissivity less than unity is mainly a consequence of low LWP, as it is saturated in the LW already at a LWP of 40 to 45 g/m^2 . A further increase in LWP does not increase the LW emission by the cloud and hence not the downward LW at the surface, but it does still increase the cloud albedo. Thus for clouds with LWP larger than 40 g/m^2 , an increase in cloud water amount would have a cooling effect at the surface.

2.3 Aerosols and clouds

Aerosols have a direct effect on the climate by scattering and absorbing SW radiation, and scattering, absorbing and emitting LW radiation. A subset of the atmospheric aerosols also serve as particles which water vapor

can condense on to form droplets [Wallace & Hobbs, 2006]. Aerosols upon which water vapor can condense are called cloud condensation nuclei (CCN). A typical size for CCN is shown in figure 2.1. For low temperatures (\sim -20 to -5°C) [Wallace & Hobbs, 2006], a few aerosols act as ice nuclei (IN) which if present allow for cloud ice to form. With IN cloud ice can form through heterogeneous freezing, contact nucleation and deposition [Wallace & Hobbs, 2006]. Heterogeneous condensation freezing is when a droplet already contains a freezing nucleus and is brought to lower temperatures so that the already condensed water on the particle freezes. Contact nucleation is when a supercooled droplet (droplet with temperature below 0°C) is hit by a suitable ice nucleus and freezes upon contact. Immersion freezing is when an ice nucleus penetrates into a droplet and makes it freeze. Deposition is when water vapor freezes directly on the ice nucleus.

Some typical CCN are sulfates, sea salt and organic carbon, whereas IN are typically mineral dust. All these types of nuclei are included in the model used in this study [Thompson & Eidhammer, 2014], which is described in the next chapter. Typical aerosol number concentrations are 10^3 to 10^5 cm^{-3} , the number of those that can act as CCN range from 10^{-2} to 10^3 cm^{-3} , and the number of available IN is about 10^{-3} cm^{-3} . The amount of aerosols that act as CCN or IN affect the radiative properties of the clouds. Such processes are known as indirect effects, two of which are described below.

2.3.1 The first indirect effect

The first indirect effect was proposed by Twomey [1974] and is often referred to as the Twomey effect. It describes the enhancement of cloud albedo as a consequence of an increase in aerosol content and a following decrease in cloud droplet size.

If there are few CCN in an area, a cloud formed there would be a clean cloud with few but large droplets. If the area had high aerosol concentration, the cloud would be polluted and have more numerous but smaller droplets. Provided the LWP is the same, the cloud would have a higher optical depth in the SW, with reduced r_e , according to equation 2.22, and a higher cloud albedo (equation 2.5).

The same is clear for ice, from equation 2.16, where it was shown that with IWP kept constant, a smaller ice crystal size yields a higher optical depth, and therefore an increased cloud albedo. Thus the first indirect effect also applies to ice, since a decrease in D_e while IWP is kept constant, means an increase in particle number, but a decrease in particle size and hence an increase in τ which in turn increases the cloud albedo.

Figure 2.3 shows that with more CCN and IN available, in a polluted environment, the cloud or cloud layer, appears brighter than when the air is clean. The increase in cloud albedo due to pollution is shown in the left-most 4 figures in the figure.

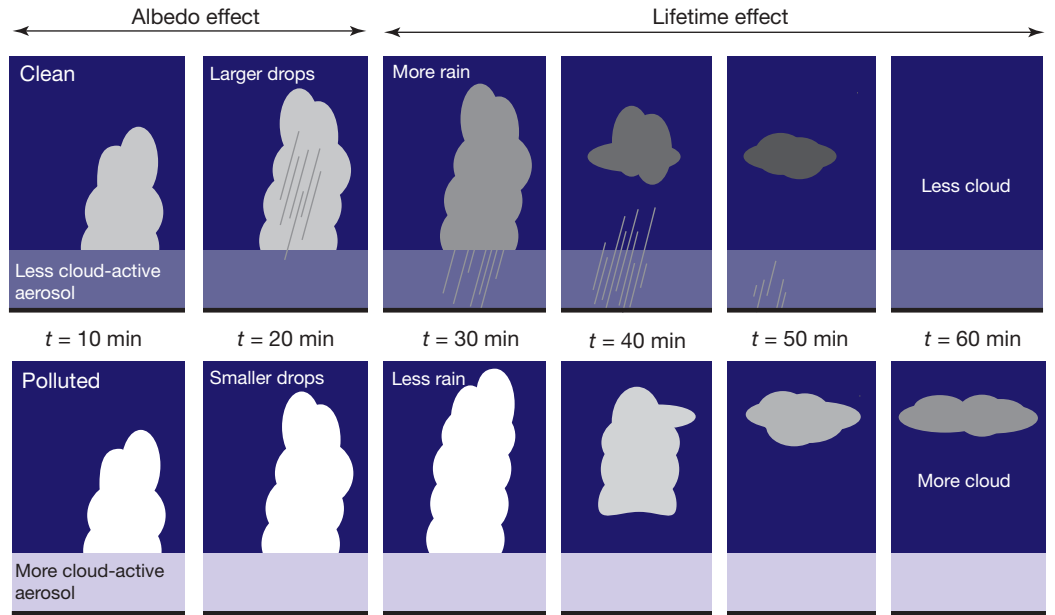


Figure 2.3: Figure showing the first indirect effect (albedo effect) to the left and the second indirect effect (lifetime effect) to the right. The figure includes a time axis to show the time scale of a precipitation process. The upper and lower panel show the clean and polluted case respectively. The figure is taken from Stevens & Feingold [2009].

2.3.2 The second indirect effect

The second indirect effect was proposed by Albrecht [1989], and is also known as the lifetime effect.

The second indirect effect suggests more numerous but smaller droplets reduce the precipitation efficiency and by that enhances the cloud lifetime and hence the cloud reflectivity [Albrecht, 1989]. The effect is depicted in figure 2.3 as the lifetime effect, where it is shown that in the lower panel, the polluted case, the cloud does not precipitate and is therefore still present after an hour, whereas the cloud in the upper panel, the clean case, is gone due to precipitation. If a cloud does not precipitate one could expect it to keep more of its liquid water for a longer time, by that increasing the lifetime of the cloud, and as shown by equation 2.22, a higher liquid water gives a higher optical depth and thereby also a higher albedo (equation 2.5).

A rain drop is formed when smaller droplets collide and coalesce into a larger droplet, which also falls to collect smaller droplets until it is large enough to fall out of a cloud as precipitation. Figure 2.1 shows raindrops typically have a radius of $1000\mu\text{m}$. The second indirect effect suggests that an increase in aerosol burden leads to the water vapor being spread over

a higher number of droplets, giving them a smaller effective radius which will prohibit them from growing to a raindrop, or delay such a growth. The hypothesis is that if the cloud does not precipitate, it will grow denser and live longer since the cloud water is not removed by precipitation. According to Lohmann & Feichter [2005] this effect was estimated to be of the same order as the first indirect effect. It has since been shown that the effect is in fact small globally averaged [Stevens & Feingold, 2009]. Stevens & Feingold [2009] state that in the cases where an increased aerosol burden prohibits precipitation, the small size of the cloud droplets make them evaporate easily. Depending on the cloud type, this enhanced evaporation can cancel the effect of reduced precipitation and the cloud ceases to exist. Also, an increase in aerosol burden in deep precipitating clouds may lead to more, not less, precipitation [Stevens & Seifert, 2008].

Chapter 3

Model and methods

To test the thesis hypothesis, a formulation of the Weather Research and Forecasting (WRF) model called the Advanced Research WRF (ARW) has been used. The model is described in the first part of this chapter. Then follows a description of the model setup and the different physics schemes that were chosen for this study, before a summary of the different runs that were performed. Ending the chapter are two short sections on the input data and processing of the model output.

3.1 Description of the WRF-ARW Modeling System

The version of the WRF-ARW modeling system used is 3.6.1, which was released in April 2014. The model is primarily developed at the National Centre for Atmospheric Research (NCAR) in Boulder, Colorado. The ARW model is the first fully compressible conservative form nonhydrostatic model designed for both research and operational numerical weather prediction (NWP) applications [Skamarock & Klemp, 2008].

As can be seen from figure 3.1 the WRF-ARW Modeling System consists of four major programs [Wang *et al.*, 2015]:

- The WRF Preprocessing System (WPS)
- WRF-Data Assimilation (WRF-DA)
- ARW solver
- Post-processing & Visualization tools

WPS is used primarily for real data simulations [Wang *et al.*, 2015], like the study presented in this thesis. A real-data simulation means that it has been initialized by observations and reanalysis, not artificial data. WPS' functions include defining simulation domains, interpolating terrestrial data

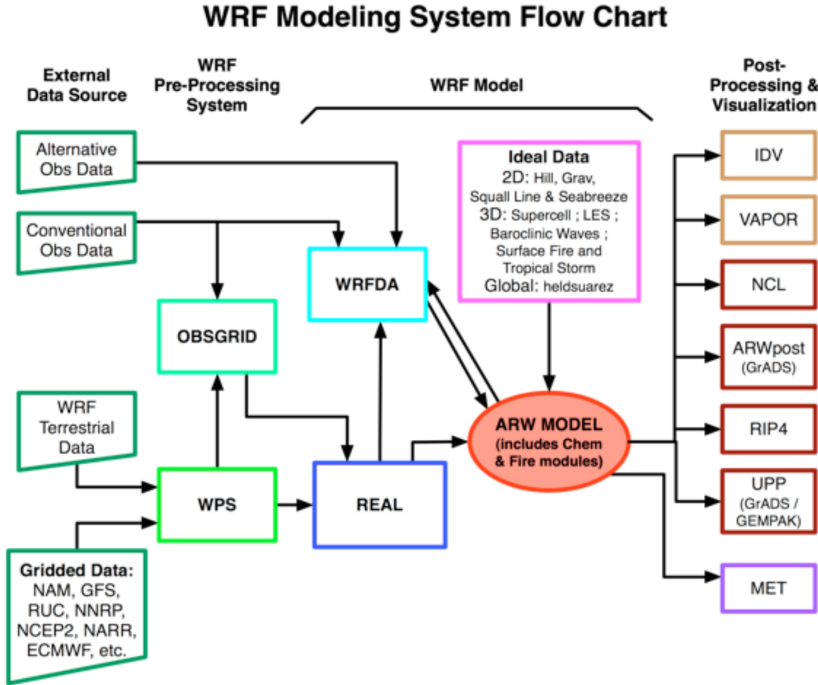


Figure 3.1: Flowchart for the WRF ARW Modeling System Version 3. From Wang *et al.* [2015].

and degridding and interpolating meteorological data from another model to this simulation domain [Wang *et al.*, 2015]. WRF-DA is optional and can be used to ingest observations into the interpolated analyses created by WPS [Wang *et al.*, 2015], but was not used in this study. The ARW solver is the key component of the modeling system, which is composed of several initialization programs for idealized, and real-data simulations, and the numerical integration program [Wang *et al.*, 2015].

The continuous equations solved in the ARW model are the Euler equations cast in a flux form where the vertical coordinate, η , is defined by a normalized hydrostatic pressure,

$$\eta = (p_h - p_{ht})/\mu \quad (3.1)$$

where $\mu = (p_{hs} - p_{ht})$ [Skamarock & Klemp, 2008]. p_h is the hydrostatic component of the pressure and p_{hs} and p_{ht} are the values of the hydrostatic pressure in a dry atmosphere at the surface and top boundaries respectively [Skamarock & Klemp, 2008].

The vertical coordinate is the traditional σ coordinate used in many hydrostatic atmospheric models, but is denoted by η in ARW, and is shown in figure 3.2.

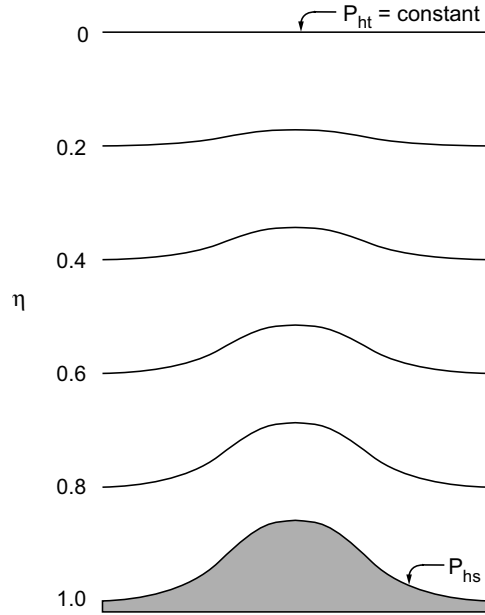


Figure 3.2: This figure is shown as presented in Skamarock & Klemp [2008], and is a schematic of the η coordinate. P_{hs} and P_{ht} represent the hydrostatic pressure at the surface and top respectively.

η decreases monotonically from a value of 1 at the surface, where the coordinate follows the terrain and $P_h = P_{hs}$, to a value of 0 at the top level, which is then a pressure surface, where $P_h = P_{ht}$. Levels with constant η are commonly referred to as η -levels (or Eta-levels). $\mu(x, y)$ is the mass of dry air per unit area within the column in the model domain at (x, y) . The η -levels are where the vertical wind speeds are calculated, whereas the thermodynamic variables (θ) are calculated between the η -levels, on so-called mass levels.

With the vertical coordinate η , and the mass of an air column, $\mu(x, y)$, in the model grid the Euler equations can be written with variables on flux form:

$$\mathbf{V} = \mu \mathbf{v} = (U, V, W), \quad \Omega = \mu \dot{\eta}, \quad \Theta = \mu \theta$$

Now \mathbf{v} is the velocity vector in three dimensions, $\omega = \dot{\eta}$ denotes the vertical velocity and ϕ is the geopotential, and the set of prognostic equations that

needs to be solved numerically is this:

$$\partial_t U + (\nabla \cdot \mathbf{V}_u) - \partial_x(p\phi_\eta) + \partial_\eta(p\phi_x) = F_U \quad (3.2)$$

$$\partial_t V + (\nabla \cdot \mathbf{V}_v) - \partial_y(p\phi_\eta) + \partial_\eta(p\phi_y) = F_V \quad (3.3)$$

$$\partial_t W + (\nabla \cdot \mathbf{V}_w) + g(\partial_\eta p - \mu) = F_W \quad (3.4)$$

$$\partial_t \Theta + (\nabla \cdot \mathbf{V}\theta) = F_\Theta \quad (3.5)$$

$$\partial_t \mu + (\nabla \cdot \mathbf{V}) = 0 \quad (3.6)$$

$$\partial_t \phi + \mu^{-1}[(\mathbf{V} \cdot \nabla \phi - gW) = 0 \quad (3.7)$$

$$\partial_t Q_m + (\nabla \cdot \mathbf{V}Q_m) = F_{Q_m} \quad (3.8)$$

To close the system they use the diagnostic equation for inverse density, α_d ,

$$\partial_\eta \phi = -\alpha_d \mu \quad (3.9)$$

and the moist equation of state

$$p = p_0 \left(R_d \theta \frac{1 + R_d/R_v)q_v}{p_0 \alpha_d} \right)^\gamma \quad (3.10)$$

where $\gamma = c_v/c_p = 1.4$ is the ratio of the heat capacity for dry air at constant volume, to that of constant pressure, R_d and R_v are the gas constants for dry and moist air respectively, q_v is the mixing ratio of water vapor and p_0 is the reference pressure (10^3 hPa). The right-hand-side terms in equations 3.3-3.6 and 3.8 represent forcing terms which arise from model physics, turbulent mixing, spherical projections, the earth's rotation, and moist physics [Skamarock *et al.*, 2008].

To solve these equations the WRF-ARW modeling system uses the spatial discretization known as a staggered C grid [Skamarock *et al.*, 2008]. Figure 3.3 shows the schematic of the grid and how the velocities, u and v , are calculated at the edges of each grid box both in the horizontal and in the vertical, half a grid box length away from the thermodynamic variable, which is calculated in the middle of each grid box, at the mass point. The advection in and out of the grid box is calculated from u and v . This staggering allows for discretization of the pressure gradient and divergence terms across a single grid interval, without any averaging, which gives a highly accurate second order difference.

The time integration in ARW is performed by a "time split integration scheme", which means that the low frequency, meteorologically significant modes are integrated by a third order Runge-Kutta (RK3) integration scheme, while the higher frequency acoustic modes are integrated with a shorter time step, to conserve the numerical stability. In general, it is preferred to use as large a time step as possible while keeping the numerical stability. For integration by the RK3 scheme the maximum time step Δt_{max}

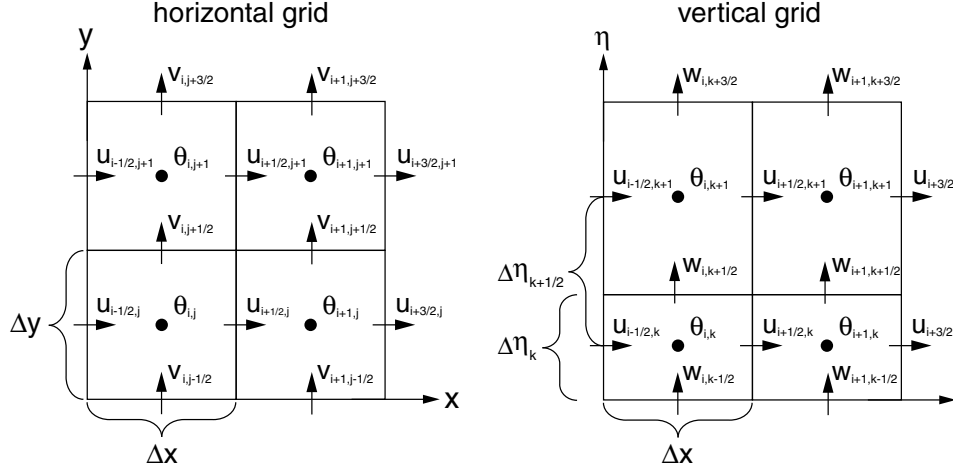


Figure 3.3: This figure is shown as presented in Skamarock & Klemp [2008], and shows the staggering of the C-grid. The horizontal staggering to the left, and the vertical staggering to the right.

is found through equation 3.11

$$\Delta t_{max} < \frac{C \cdot \Delta x}{\sqrt{3} \cdot u_{max}} \quad (3.11)$$

where C is the maximum Courant number, which depends on the order of the discretization of the advection terms. Typically in WRF, it is recommended that Δt (in seconds) does not exceed 6 times Δx (in km). When running the modeling system with a horizontal resolution of 4 km grid point spacing I therefore chose $\Delta t = 24$. Details about the model runs and choices of physics in the model is presented in the next section.

3.2 Model setup

The model was run with a $4 \text{ km} \times 4 \text{ km}$ horizontal grid point spacing, with 300×300 grid points, and 72 vertical layers, with the model top at 10 hPa. The area covers parts of the Beaufort Sea, north of Canada and Alaska. This area was chosen because data from the area has been used for related studies [Eastman & Warren, 2010, Kay & Gettelman, 2009, Palm *et al.*, 2010, Schweiger *et al.*, 2008, Shupe & Intrieri, 2004, Wu & Lee, 2012] as mentioned in Chapter 1. The area is not completely ice free any part of the year [NSIDC, 2015], and provides a good place to simulate cloud-sea ice interaction. The area spans several time zones, and is approximately 7 hours behind UTC time. The times given in the WRF-ARW modeling system are UTC. The model was run for a period of 5 days, 1st to 6th of September 2012. This is approximately when the record low ice extent in the Arctic

was set (eg. National Snow and Ice Data Centre, U.S.A., [NSIDC, 2015]).

The vertical layers in the ARW model are often referred to as eta levels, because of the choice of η as the vertical coordinate. These levels have uneven vertical spacing and the altitude of each level is dependent on pressure. Therefore, the level height varies in both time and space. As a consequence of pressure dependence, the levels in the lower troposphere are closer to each other than the levels higher up in the troposphere. Thus the low clouds in the area can be resolved. In this study, only the lowest 11 eta levels have been used to study the low clouds. Approximate heights for the lowest 11 eta levels are shown in Table 3.1.

Table 3.1: Approximate height for each of the lowermost 11 eta levels, in meters above the surface.

Eta level	Approximate height
1	10 m
2	60 m
3	140 m
4	220 m
5	380 m
6	540 m
7	800 m
8	1000 m
9	1350 m
10	1500 m
11	1800 m

3.2.1 Choices of physics in the model

The selection of physics schemes in WRF-ARW are numerous and fall into several categories, each containing several choices. Table 3.2 shows some of the different categories and the choice of scheme, for this study, within each of those categories.

Table 3.2: Table of physics categories and choice of scheme for this thesis

Physics categories	Scheme selected within category
(1) microphysics	aerorol-aware [Reisner <i>et al.</i> , 1998, Thompson & Eidhamer, 2014, Thompson <i>et al.</i> , 2004, 2008]. Option 28.
(2) cumulus parameterization	Grell 3D [Grell, 2002]. Option 5.
(3) planetary boundary layer (PBL)	Yonsei University scheme [Hong & Dudhia, 2004]. Option 1.
(4) land-surface model	Noah Land Surface Model [Tewari <i>et al.</i> , 2004]. Option 2.
(5) radiation	RRTMG LW & SW [Iacono, 2003, Iacono <i>et al.</i> , 2000, 2008, Mlawer <i>et al.</i> , 1997]. Option 4 in both LW and SW.

The ARW model offers a wide selection of schemes to treat different physics that one wants represented in the model. The schemes treat the physics slightly differently. Some schemes are better for certain horizontal and vertical resolutions than others, so one needs to be careful when choosing how the model is to treat the physics. For my thesis, the especially relevant scheme to mention is the cloud microphysics scheme that I chose, which is the aerosol-aware scheme described in Thompson & Eidhamer [2014]. When studying cloud and radiation response to removal of sea ice, one might expect an increase in aerosols from the open ocean and increased sea traffic. The aerosols are therefore also relevant for the choice of schemes, and the aerosol-aware scheme, described further below, includes the necessary processes for this study.

The choice of cumulus parameterization was based on the grid resolution, and the best fit for it. A horizontal grid point spacing of 4 km can be fine enough to not use cumulus parameterization [Thompson & Eidhamer, 2014], but in this thesis a parameterization that was more suitable for grid point spacings less than 10 km was chosen; the Grell 3D parameterization. According to Wang *et al.* [2015] Grell 3D may be used on high resolution, like my 4 km grid point spacing.

The aerosol-aware scheme

The microphysics includes explicitly resolved water vapor, cloud, and precipitation processes. The aerosol-aware scheme was chosen so that the study would have scavenging of aerosols included and have proper enough representation of aerosols to study aerosol–cloud interactions, without using the WRF model coupled with chemistry (WRF-Chem). According to the ARW User’s Guide by Wang *et al.* [2015], the aerosol-aware scheme con-

siders water- and ice-friendly aerosols, and a climatological data set may be used to specify initial and boundary conditions for the aerosol variables. I have used this climatological data set, which will be explained in Subsection 3.3.1 Input data. The scheme uses a monthly mean for aerosol number concentrations derived from multi-year (2001-2007) global model simulations in which particles and their precursors are emitted by natural and anthropogenic sources and are explicitly modeled with multiple size bins for multiple species of aerosols by the Goddard Chemistry Aerosol Radiation and Transport (GOCART) model [Thompson & Eidhammer, 2014]. The aerosol-aware scheme [Thompson & Eidhammer, 2014] is built on the schematic shown in figure 3.4, from Reisner *et al.* [1998]. It is a double moment scheme, which means it computes both mass mixing ratios, Q , and number concentrations, N , for the same water species (hydrometeors).

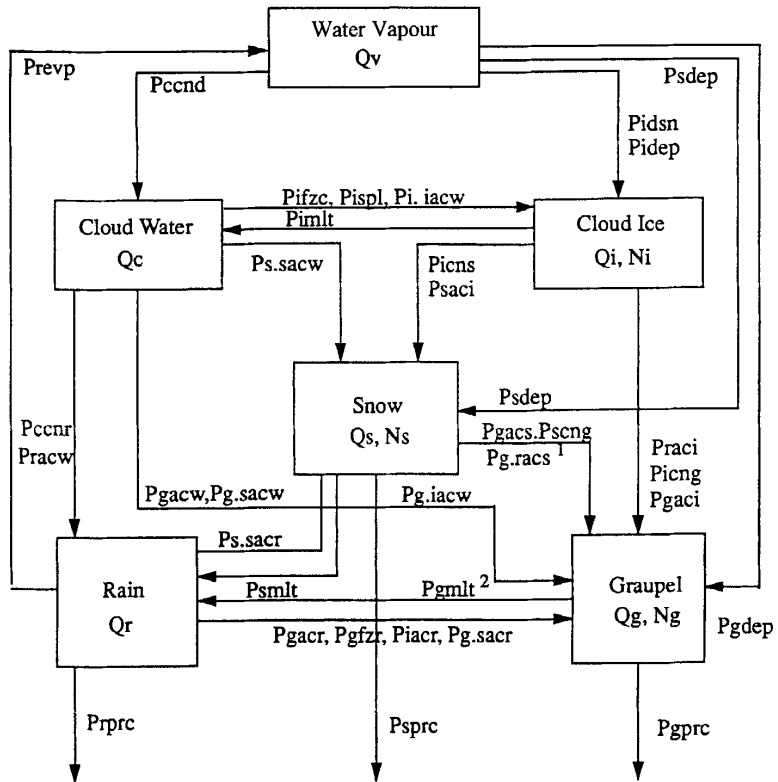


Figure 3.4: Cloud microphysical parameterization scheme used in some NWP models as shown in Reisner *et al.* [1998]. A full list of the acronyms used in the schematic can be found in Reisner *et al.* [1998].

Figure 3.4 show the processes in the microphysics scheme developed by Reisner *et al.* [1998], which the first bulk microphysics scheme by Thompson [Thompson *et al.*, 2004] was based on. The aerosol-aware scheme [Thompson *et al.*, 2004] was developed to include the processes shown in Figure 3.4.

son & Eidhammer, 2014] is an extension of the updated Thompson bulk microphysics scheme described in Thompson *et al.* [2008]. The figure shows a schematic of five hydrometeors, cloud water (c), rain (r), ice (i), snow (s) and graupel (g), and if just the mass mixing ratio is calculated or if both the mass mixing ratio and the number concentration is calculated. For each of the hydrometeors, prognostic equations are used with all the sources and sink terms included.

The RRTMG radiation schemes

According to Thompson & Eidhammer [2014] the Rapid Radiative Transfer Model (RRTM) for General Circulation Models (GCMs) (RRTMG) schemes for SW and LW [Iacono, 2003, Iacono *et al.*, 2000, 2008, Mlawer *et al.*, 1997] are the only radiation schemes which include the effects of the effective radii calculated in the aerosol-aware scheme. These were therefore used in combination with the aerosol-aware cloud microphysics scheme. The RRTMG schemes are accurate schemes using look-up tables for efficiency, and accounts for multiple bands and microphysics species, and includes the Monte Carlo Independent Column Approximation (MCICA) method of random cloud overlap [Wang *et al.*, 2015].

3.3 Model runs

The results presented in the next chapter are based on four different runs. The control run is the run where the aerosol climatological data set has been used unchanged, and where the sea ice is kept as it was in the downloaded input data, see Subsection 3.3.1. The control run is used as a base to compare the other runs to, those with no ice and/or increased aerosol number concentrations.

There are two runs where the sea ice was removed, NoIce and Aero10NoIce. The point of this is to compare the run with no ice to the control run, and see if there are any changes in the cloud properties, and SW and LW fluxes. For one of those runs the aerosol number concentration was also increased. Results from this run can be compared with the control run.

The number of water- and ice-friendly aerosols were multiplied by 10 both with and without sea ice for two runs: Aero10 with ice, and as mentioned above, Aero10NoIce without ice. The goal is to find changes in cloud properties and radiation fluxes compared to those in the control run.

Table 3.3 shows an overview of the different runs that have been performed, whose output have been used for production of figures presented in the next chapter.

Table 3.3: Table showing the names of the runs and if they have sea ice or not, and if the aerosol concentration has been increased by a factor of 10 through input files. All the runs have the same horizontal resolution of 4 km×4 km, dimensions 300×300, 72 vertical layers and $\Delta t=24$ s.

Name	Sea ice	Aerosol concentration
Control	initial	climatology
NoIce	removed	climatology
Aero10	initial	climatology×10
Aero10NoIce	removed	climatology×10

3.3.1 Input data

The model runs were initialized with data downloaded from the European Centre for Medium-Range Weather Forecasts (ECMWF) [ECMWF, 2015]. The downloaded data is from the ERA-Interim data set, which is a global atmospheric reanalysis from 1979 to present and continues to be updated in real time [ECMWF, 2015]. Through WPS the data from ERA-Interim was interpolated over the area, with a 2 degree minute spacing between the points, to be used to initialize the model. The data used is in 6-hourly atmospheric fields on pressure levels, for the first five days of September 2012, which was the period the model was run for. This is done to make sure the initial meteorological conditions are the same in every run, so that the effects of changing a variable in the input files for the modeling system are only due to that change.

To use the climatological aerosol data set, the file containing monthly means had to be called through WPS. The aerosol input data includes mass mixing ratios of sulfates, sea salts, organic carbon, dust, and black carbon from a 7-yr simulation with 0.5° longitude by 1.25° latitude spacing [Thompson & Eidhammer, 2014].

3.3.2 Manipulation of input files

The input files for the ARW solver, created by WPS and REAL (see figure 3.1) were manipulated by use of the NetCDF Operator (NCO) tool ncap2. In these files the sea ice was removed for the runs without sea ice (NoIce and Aero10NoIce) and the aerosol number concentration from the climatological data set was multiplied by 10 for the runs with increased aerosol number concentration (Aero10 and Aero10NoIce).

3.4 Processing the model output

Figures presented in my thesis were made by me (unless stated otherwise) by use of NCL (National Center for Atmospheric Research (NCAR) Command Language) citepNCL. For the NCL scripts I found a lot of help and inspiration from the example scripts for WRF-users, found on the NCL web page [UCAR, 2015].

The model output was stored as instantaneous values for every hour for each of the five days, from each of the four runs.

To study the response in cloud radiative properties, fields of interest were made into daily time averages, by use of NCL, in each run. Some fields vary only in horizontal space and in time (2-dimensional in space), and were simply added together and divided by the number of hours in a day. These fields are: SW and LW radiation down at the surface and up at the top of the atmosphere (TOA), latent heat (LH) and sensible heat (SH), temperature at the surface and at 2 m height and winds at 10 m height.

The cloud parameters, such as r_e and CDNC, vary also in the vertical (3-dimensional in space) and have been averaged over the 11 lowermost layers (the lower ~ 1800 m above the surface) and all hours of the day. Hence, the figures showing r_e and CDNC over maps do not account for variations in the vertical.

The LWC on the other hand has not been averaged over the layers, but summarized into LWP. In each of the lowermost 11 layers the LWC has been multiplied with the thickness of the respective layer and then added in height to make the LWP.

The differences between two runs, presented in the next chapter, are daily time averaged differences. Where the difference has been calculated for every hour of the day, and then averaged in time.

Chapter 4

Results and discussion

In this chapter, the results of the simulations outlined in Chapter 3 are presented. First, the model output from the control run (Control) is described. The control run is also used for comparison and reference in the following sections. The chapter mostly consists of a discussion of why there is a difference in certain cloud and radiation variables between NoIce and Control, and between Aero10 and Control. At the end, there is also a section on the difference in the fields between Aero10NoIce and Control.

The discussion is based on daily time averaged differences between Control and the other runs. The results are discussed separately for NoIce, Aero10 and Aero10NoIce for days 1 and 5 (1st and 5th of September 2012). Here day 1 represents the closest to an "off line" run, with near instantaneous changes in clouds due to ice removal or aerosol increase, whereas by day 5 the atmosphere has had some time to adjust to the changes that were imposed at the beginning of the first day of the run.

In a few of the plotted differences, the most extreme differences (both positive and negative) have been left outside the range of the color bar, because they overshadowed the smaller differences. This is done to more clearly see the differences, but without changing the overall picture. The most extreme values are still included in the field averaged value showed in each figure.

I also try to answer if these results show a warming or cooling effect.

4.1 The control run

Figure 4.1 shows the weather situation in the control run for days 1 and 5. The temperature at 2 m height is represented by red contour lines, and the wind direction and speed at 10 m height is shown by the wind barbs and their color. Recall from figure 1.1 that the northernmost latitude line (bottom right corner) in the figure represents 80°N, followed by 75°N, and then 70°N latitude line (top left corner). Day 1, figure 4.1a shows weak

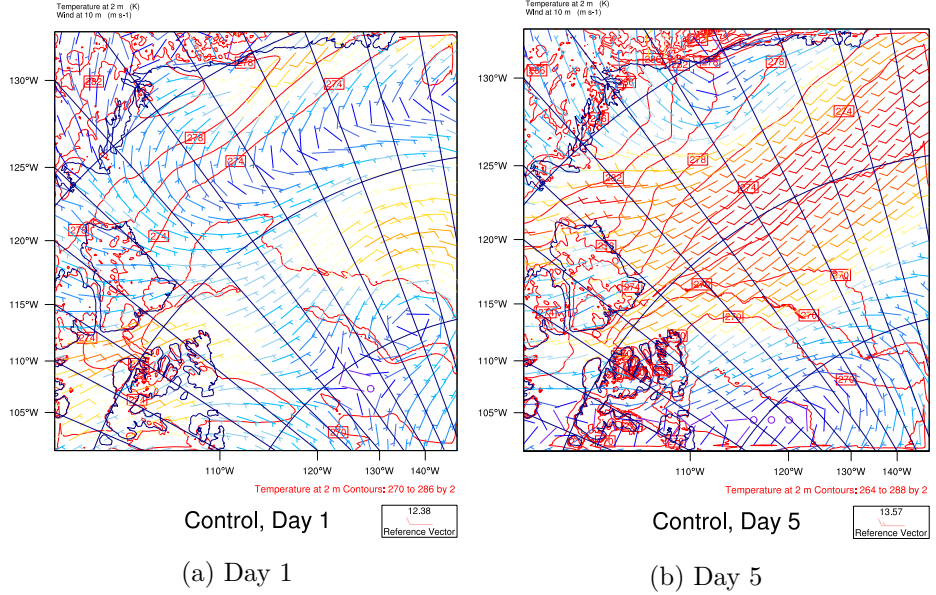


Figure 4.1: The temperature and wind pattern for days 1 and 5, from the control run. The temperature at 2 m height is represented by red contour lines and the wind speed and direction at 10 m height is shown by wind barbs and their color, where red indicates higher wind speed and blue indicates lower. The shortest tails on the wind barbs indicate a wind speed of 5 m/s and the longest indicate 10 m/s.

northery winds (~ 5 m/s) bringing cold air, -3°C (270 K), from the north over the sea ice, and the westerly winds over the ocean south of the sea ice bring moisture to the air over the sea ice, which contributes to the low stratus in figure 4.2a. Figure 4.2 contains the vertical cross sections of LWC and IWC (and temperature) over the line shown in figure 4.2d. The deeper clouds over the island in figure 4.2a have been formed due to orographic lifting. The height of the "mountain" is ~ 400 m according to the y-axis in the cross section, and the filled contours of terrain height in figure 4.2d. The westerly winds over the sea ice, towards the mountain at $\sim 76^{\circ}\text{N}$ and 112°W , increase in strength over the mountain. The air is brought to saturation as it is lifted over the mountain by the winds, and forms deeper clouds over the mountain with LWC of $\sim 0.1 \text{ g/m}^3$. From figure 4.2b, showing the ice water content (IWC) in the section, one can see that the thicker clouds over the mountain also contain ice in the upper part of the clouds, with about $5 \cdot 10^{-3} \text{ mg/m}^3$.

By day 5 the wind direction has changed to south-easterly, see figure 4.1b, and the clouds in the cross section, figure 4.2c are low stratus over the sea ice, and there is also some thin cloud formation at the mountain, probably formed by weaker orographic lifting. There is no IWC in the section for day

5 (not shown). The stratus clouds in day 5 (figure 4.2c) have highest LWC in the core of the clouds, where the temperature is lowest, there the temperature inversion stops the air from rising further. Following theory [Rogers & Yau, 1989], LWC increases with height above cloud base and reaches its maximum at the cloud top. The LWC does rise with height above cloud base as expected, except for at the cloud top. Entrainment of dryer air at the top of clouds causes cloud droplets to evaporate and thereby thins the clouds [Wallace & Hobbs, 2006].

The LWP, CDNC and r_e for days 1 and 5 are shown in figure 4.3. One can see that the LWP and the CDNC have a similar pattern, which is as expected based on equation 2.13. The pattern in r_e also fits quite well with that of LWP, where the effective droplet radius is higher so is LWP, which can be interpreted as that larger droplets contain more water. These similarities in patterns are true for both days 1 and 5. In the daily averaged LWP for day 1, figure 4.3a, there are some areas with LWP of 0-20 g/m², for instance 78-81°N 135-145°W. Here there are no low clouds, which is also evident from the lack of number of droplets per cubic centimeter in figure 4.3c. This figure shows the numbers with units 10⁶ kg⁻¹, which can be approximated to the more common units for CDNC, per cubic centimeter (cm⁻³). Assuming that the clouds are close enough to the surface to assume an air density $\rho_a = 1 \text{ kg/m}^3 = 1 \text{ kg}/10^6\text{cm}^3$, then for CDNC 10⁶/kg = cm⁻³ is a good approximation. Based on the LWP from day 5 (figure 4.3b), most of the low clouds were only in the western part of the domain on that day. Particularly thick low clouds are seen just south of 75°N and west of 130°W. Where the LWP ranges from 100 to almost 300 g/m², and the CDNC ranges from 15 to 60 cm⁻³ (figure 4.3d). These clouds contain many droplets with averaged effective radius as large as 8 μm (figure 4.3f).

Figure 4.4a shows the time averaged downwelling SW radiation at the surface. There the dark blue colors, indicating less downwelling shortwave radiation, fit well with the pattern for LWP in figure 4.3a. Meaning that there are low clouds in the study area that don't let much SW through, in fact most of it is reflected. The SW up at the top of the atmosphere (TOA) (figure 4.4b) has the inverse pattern of SW down at the surface (figure 4.4a), which both fit well with the pattern in LWP for the low clouds, thus indicating that the low clouds have reflected much of the SW up at TOA. The effect of the low clouds can also be seen in the figures for LW radiation, where all the green in figure 4.4c indicates a LW radiation flux downward at the surface of 270-200 W/m². This pattern of green is also recognized as a good fit with the LWP of the lower 1800 m of the atmosphere on day 1 (figure 4.3a). The LW up at TOA (figure 4.4d on the other hand does not show the same values as for the downward LW. The LW up at TOA lies mostly in the range 195-225 W/m². The average value for the field is 215.5 W/m², which is almost 60 W/m² less than the average 272.6 W/m² downward at the surface. Therefore there must be clouds higher up absorb-

ing and re-emitting the LW radiation at lower temperatures, which according to Stefan-Boltzmann's law (equation 2.1) yields a smaller flux.

It is interesting to notice from figure 4.4 that the downwelling LW at the surface, on average 272.6 W/m^2 (figure 4.4c), is about three and a half times the average upwelling SW at TOA, of 76.9 W/m^2 (figure 4.4b). Hence, in this case the low clouds had a warming effect at the surface 1st of September 2012.

On day 5, similarly to day 1, the low cloud pattern, illustrated by LWP (figure 4.3b) is evident in the lack of downward SW at the surface (figure 4.5a). The same goes for SW up at TOA (figure 4.5b), also here the low cloud pattern is recognized. Especially in the area with high LWP (figure 4.3b) and higher CDNC (figure 4.3d), $75\text{-}72^\circ\text{N}$ $130\text{-}160^\circ\text{W}$, the SW flux up at TOA is particularly high. Assuming that this is reflected by the low clouds in that area fits with equation 2.22 where the high liquid water path gives a higher cloud optical depth, which in turn gives a high cloud albedo (equation 2.5). Notice also that both the SW down at the surface (figure 4.5a) and up at TOA (figure 4.5b) is about 110 W/m^2 (notice the different scales) around $75\text{-}77^\circ\text{N}$ and $110\text{-}125^\circ\text{W}$, and can be seen as small yellow dots in figure 4.5b. That the flux is almost the same both down at the surface and up at TOA indicates that there are glaciers and/or snow in those spots, with particularly high albedo (0.9-1) [NSIDC, 2015].

The downward LW at the surface on day 5 (figure 4.5c) is obviously mostly from the low cloud amounts in the area of $75\text{-}72^\circ\text{N}$ $130\text{-}160^\circ\text{W}$, which is where most of the high flux of LW is located. There is also a significant LW signal from the clouds located at 78°N $120\text{-}125^\circ\text{W}$. Again confirming the cloud emissivity dependence on LWP (equation 2.2). The upward LW at TOA (figure 4.5d) on the other hand is not highest over the area of highest LWP in the lower layers. The highest flux of LW up at TOA is over Canada in the southernmost part of the study area (south of 70°N between 130 and 140°W). This area was free of low clouds (see figure 4.3b) and is clearly quite free of high clouds too with these high values of LW flux upward at TOA ($\sim 250 \text{ W/m}^2$). The lower values over the area with significantly higher LWP ($75\text{-}72^\circ\text{N}$ $130\text{-}160^\circ\text{W}$) is either because the clouds in that area stretch higher up into the atmosphere, thus emitting at lower temperatures than the low clouds, or there are simply other clouds higher up in the same area that also would emit less as a consequence of lower temperatures.

The heat fluxes upward at the surface, latent heat (LH) and sensible heat (SH), are also of interest when studying clouds in the Arctic. The fluxes are shown in figure 4.6 for days 1 and 5. Notice that the LH is lower over the sea ice for both days 1 and 5. This is because the sea ice is colder than the ocean, and works as a lid over that part of the ocean, not letting all the heat and water vapor out. Another thing to notice is the marked increase in SH just off the sea ice edge, 77°N , 135°W , day 5. This is due to the strong winds in that area (figure 4.1b), which brings cold air from over

the ice out over the warmer open ocean. Thus the temperature gradient is stronger just off the sea ice edge, increasing the heat given from the surface to the overlying air. The effect is strongest at the sea ice edge, but is also evident further away over the ocean, to about 160°W. The reason the signal is so clear at the ice edge and stretches far is the wind speed, which is just above 10 m/s (see figure 4.1b). In figure 4.6d is also a white "blob" south of the sea ice (70-75°N and 125-140°W), which indicates a negative heat flux of about 20 W/m². There the surface draws heat from the overlying air, since the temperature at 2 m height (figure 4.1b) is higher than the skin temperature (figure 4.7b) in that area. This warmer air is brought over the ocean by winds coming from land southeast of that area, see figure 4.1b. The figure also shows the strength of the wind field, which was mentioned as a reason for the high SH off the ice edge and is also the reason for the strong negative heat flux.

The daily time averaged skin temperature of the study area is shown in figure 4.7, for both days. It shows that the skin temperature is generally lower at the sea ice surface than the ocean surface and land surfaces. Also, the skin temperature increases further south, and is highest over land, which is furthest south. The skin temperature is lowest in day 5, in the same spots that were claimed to be glacier and/or snow when discussing the figures showing SW down at the surface and up at TOA on day 5 (figures 4.5a and 4.5b). The temperature there is ~-13°C (260 K).

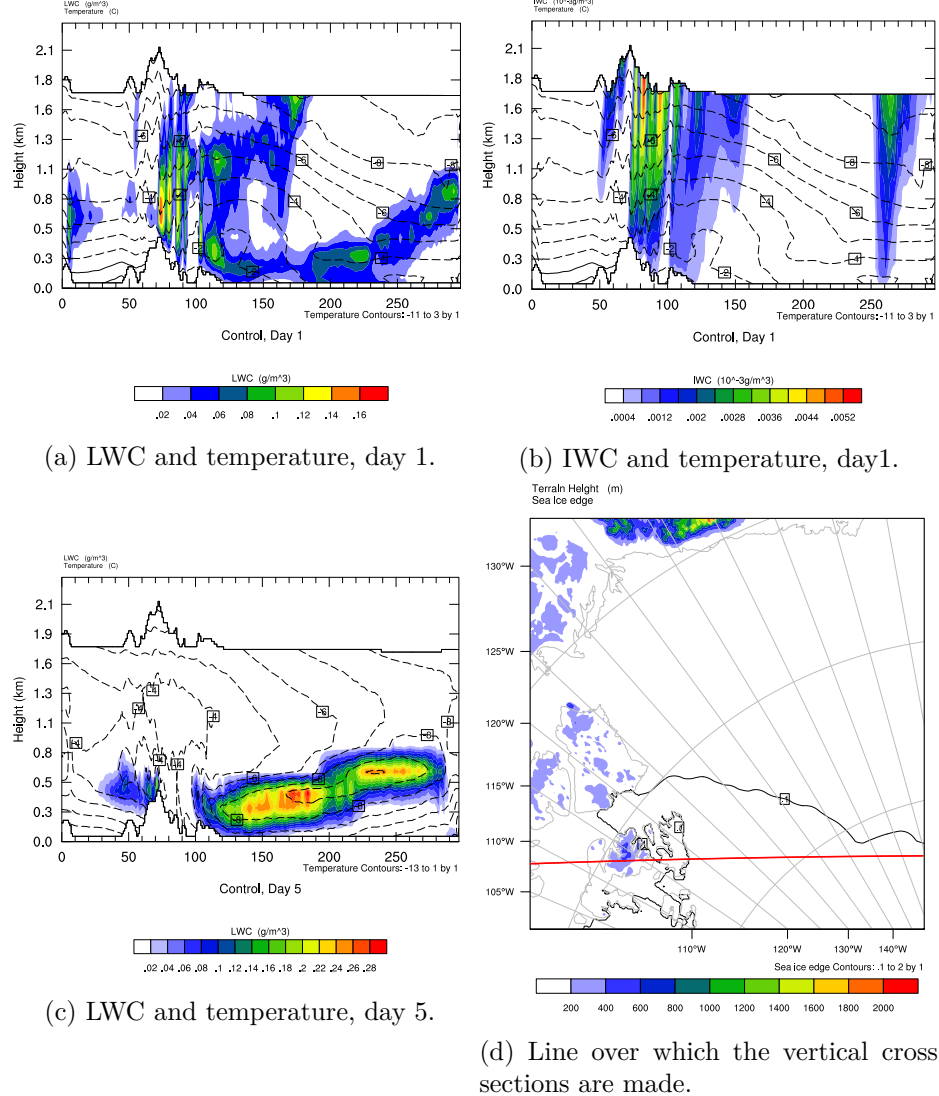


Figure 4.2: Vertical cross sections of averaged liquid (g/m^3) and ice (mg/m^3) water content, as filled contours, with temperature ($^\circ\text{C}$) as dashed contours, from the control run, for days 1 and 5. LWC and IWC for day 1 are shown in figures 4.2a and 4.2b respectively. Figure 4.2c shows the LWC for day 5. (Notice the different scales.) The IWC on day 5 was 0 in the section and is not shown. Figure 4.2d shows a map of the area with the ice edge as a black contour line. Terrain height is represented by filled contours and the red line over the sea ice is the line over which the cross sections are made.

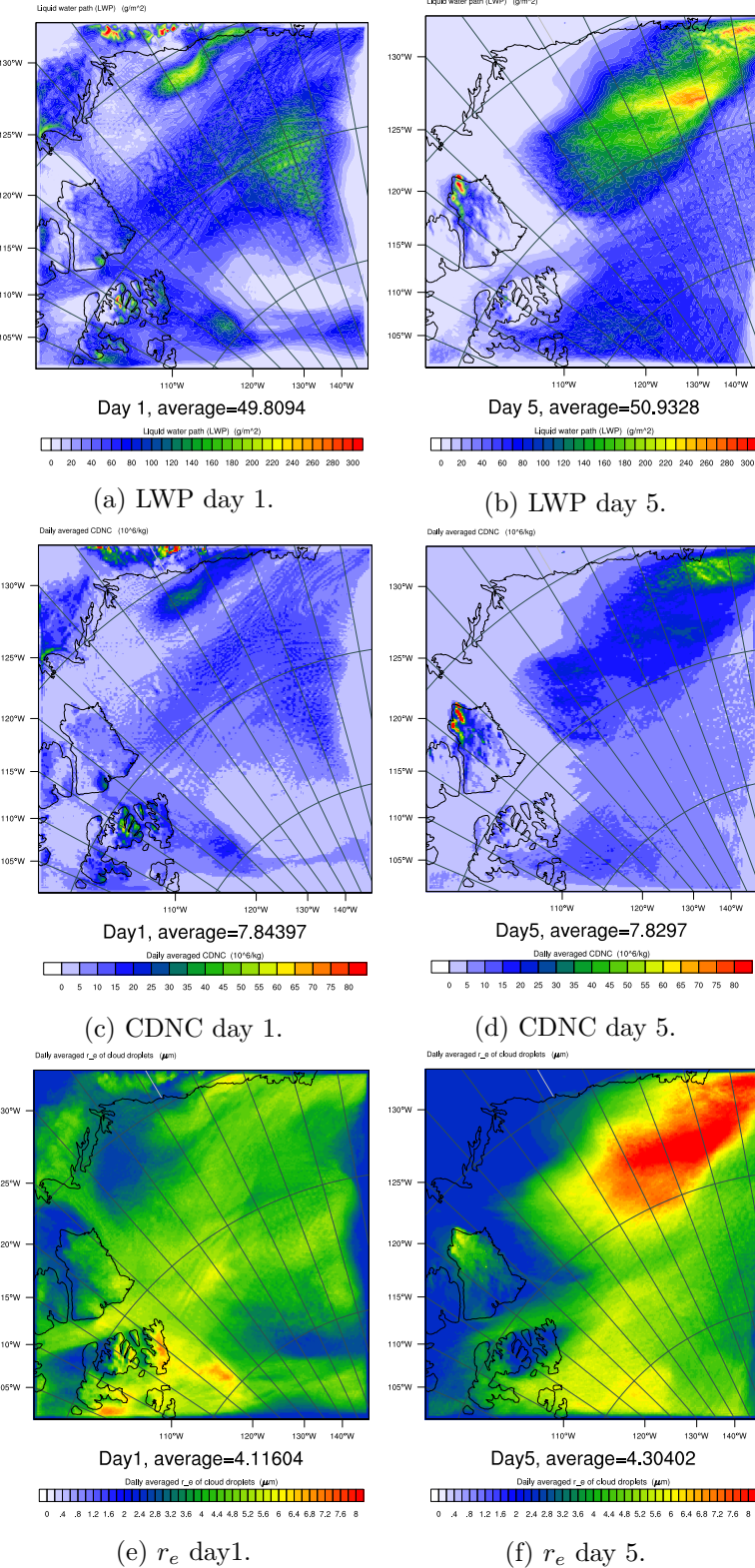


Figure 4.3: LWP averaged in time, and CDNC and r_e averaged over the lowermost 11 layers and time, for days 1 and 5. Control.

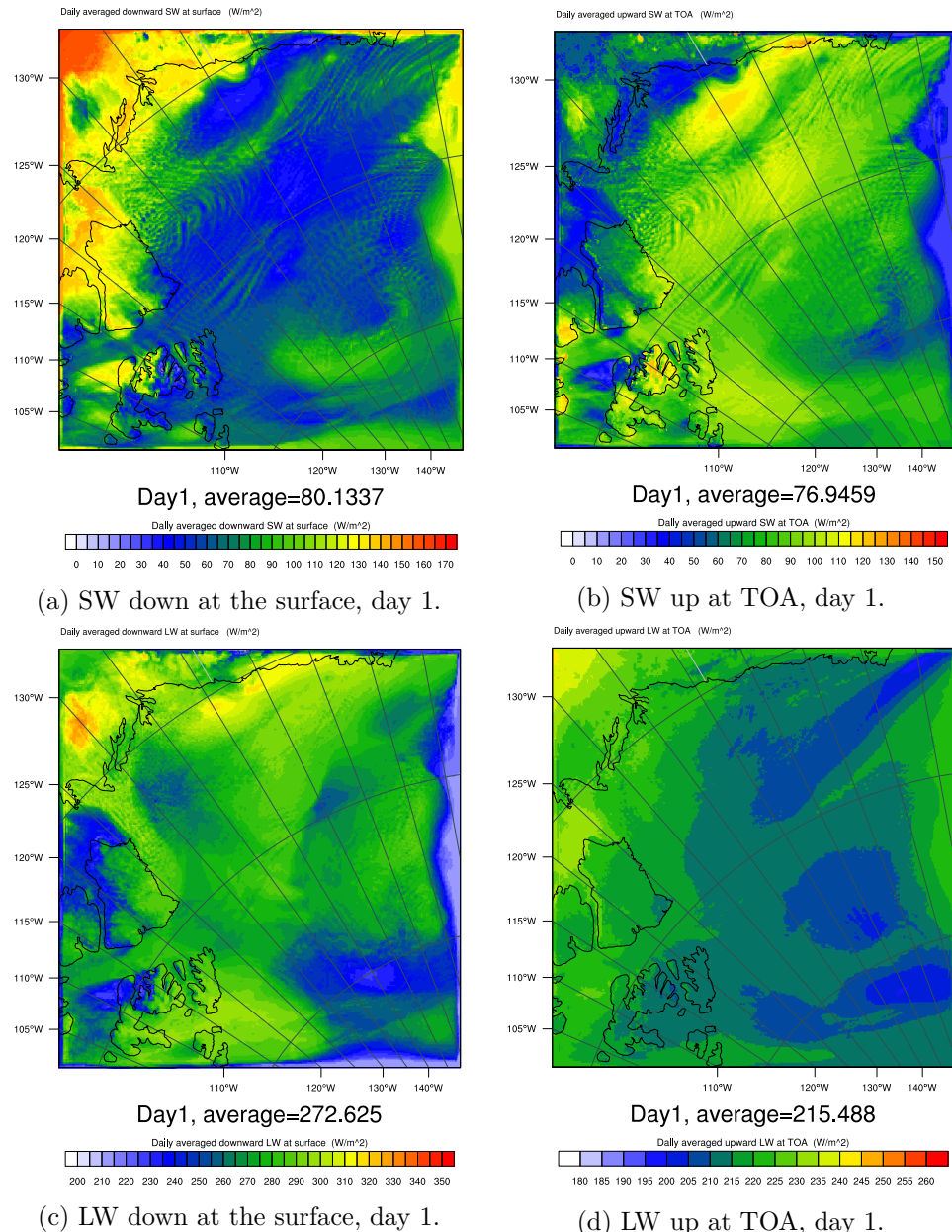


Figure 4.4: The average SW and LW flux down at the surface and up at TOA, for day 1. Control.
Notice the different scales.

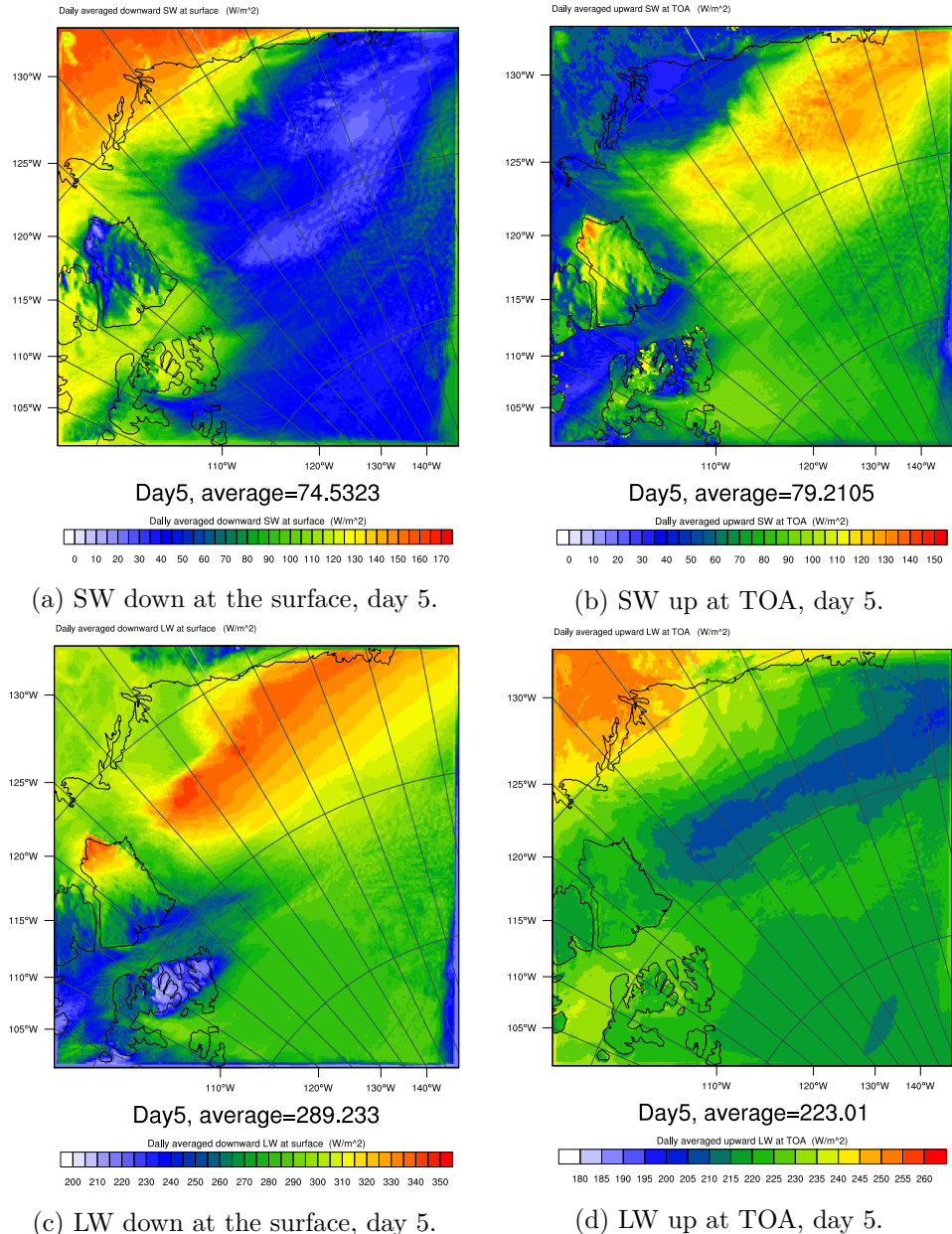


Figure 4.5: The average SW and LW flux down at the surface and up at TOA, for day 5. Control.
Notice the different scales.

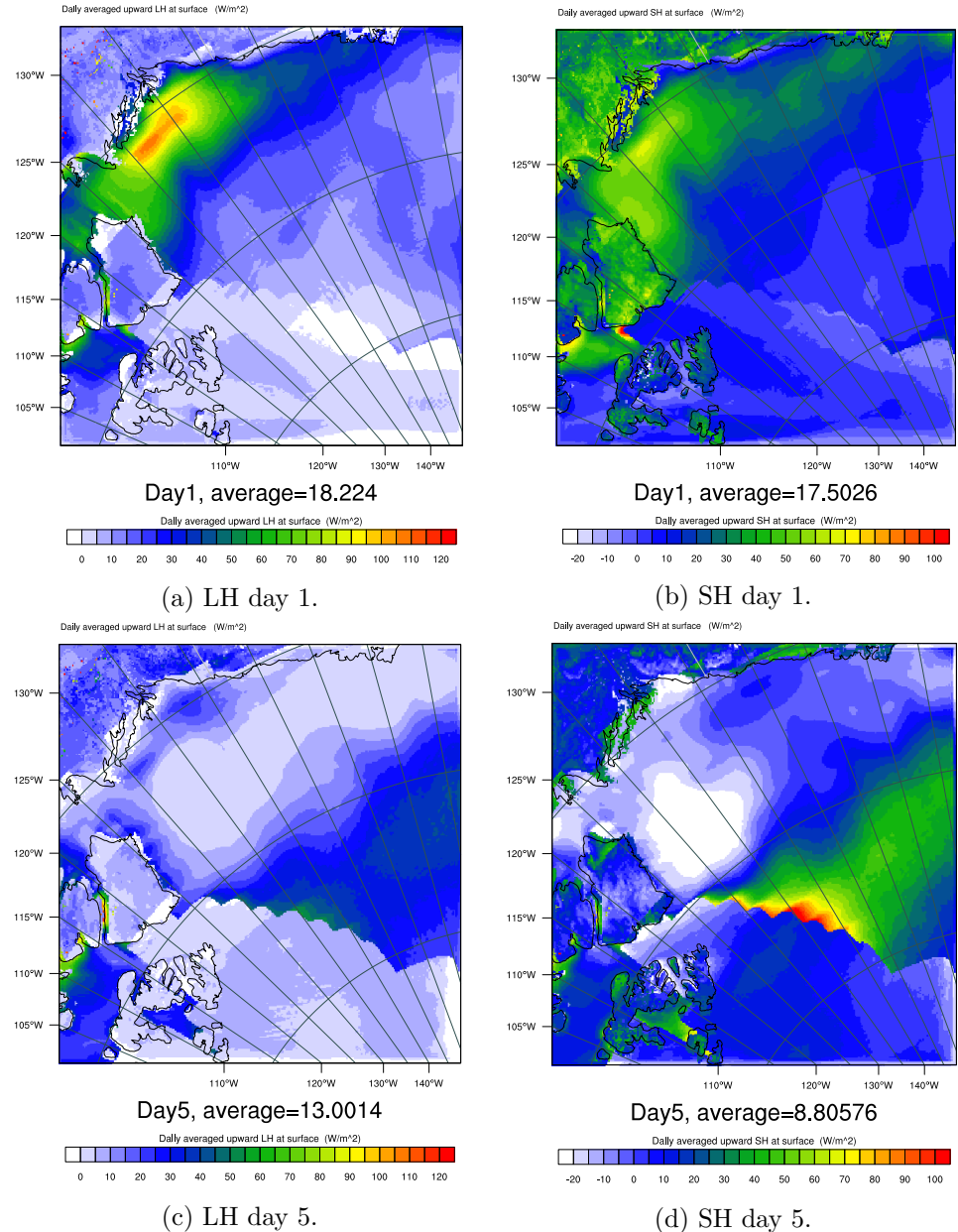


Figure 4.6: The average surface heat fluxes (SH and LH) up at the surface, for days 1 and 5. Control.

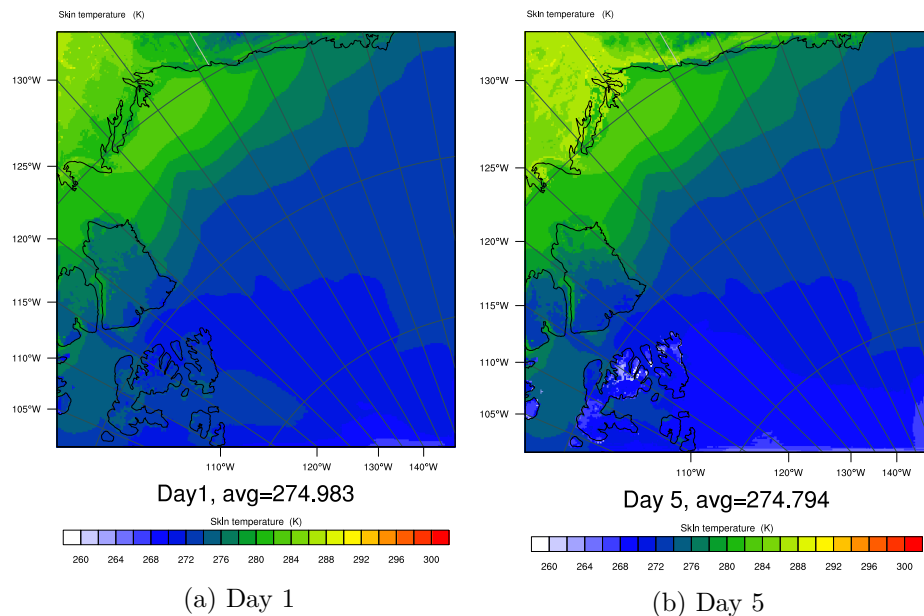


Figure 4.7: Daily averaged skin temperature (K) of the study area, for both days 1 and 5. Control.

Notice the different scales.

4.2 Removed sea ice

The sea ice was removed to study the effect this had on the cloud radiative properties, and through that if it had heating or cooling effects at the surface. The sea ice that was present in the control run, but has been removed for NoIce, is shown in figure 4.8.

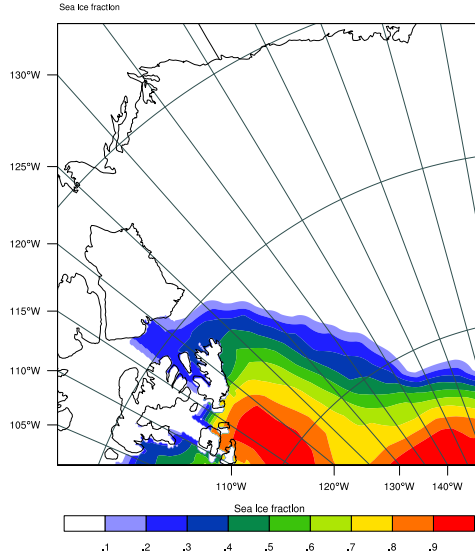


Figure 4.8: Sea ice fraction in Control (and Aero10).

4.2.1 Day 1

Removal of sea ice should lead to an increase in aerosol number concentration. As mentioned in Chapter 1, the open sea surface will release sea salt, primary organic matter and DMS. The increase in water-friendly aerosols is seen just over the newly open sea surface in figure 4.9a. Recall that the section is over the red line shown in figure 4.2d, over the sea ice. Making the same approximation here as for CDNC, $10^6 \text{ kg}^{-1} = 1 \text{ cm}^{-3}$, there is an increase of water-friendly aerosols of up to 25 cm^{-3} . And above there is approximately an equal decrease. Although the numbers in figure 4.9b, showing difference in CDNC between NoIce and Control, are not the same, there is an increase in number of droplets in the same area as there is a decrease in water-friendly aerosols. This indicates that water-friendly aerosols that were not activated in Control could be activated and grow into cloud droplets in NoIce, due to enhanced evaporation from the open ocean. This meaning that the clouds in the control run (figure 4.2a) are there in NoIce too (similar pattern), but get denser where the water-friendly aerosols are now activated. This means that there are more available aerosols close to

the newly opened sea surface, and that aerosols in that area are more likely to be activated due to enhanced evaporation.

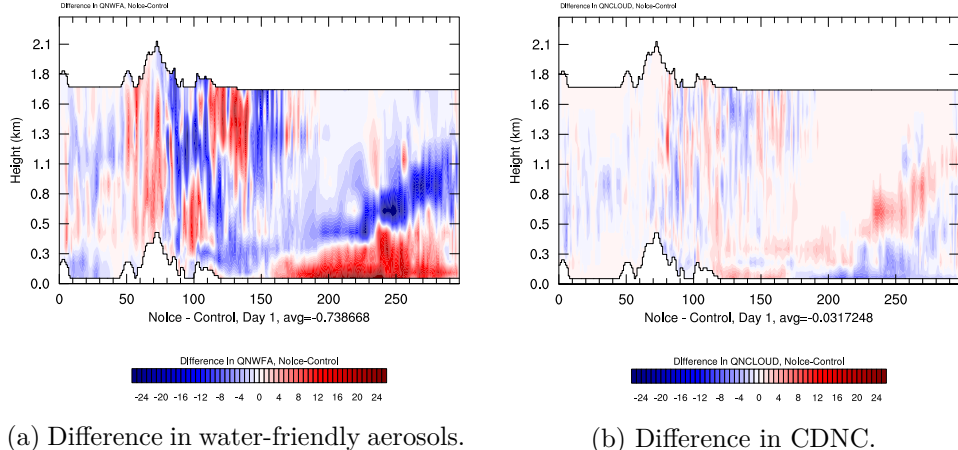


Figure 4.9: Difference in time averaged CDNC and number concentration of water-friendly aerosols for day 1. Units: kg^{-1} . NoIce-Control.

The average difference in LWP, NoIce-Control, for day 1, shown in figure 4.10a is small for the whole field ($\sim 0.23 \text{ g/m}^2$ increase). But the area of interest in this case is where the sea ice is no longer present (recall figure 4.8). The area where there was sea ice in the control run shows a positive difference in LWP. Especially furthest north (bottom right corner of the map) the LWP is significantly higher, $> 15 \text{ g/m}^2$.

Looking back to figure 4.3a, there were no low in that area. This implies that there could be new clouds forming there, that could not form when there was sea ice. The removal of the sea ice has allowed for release of more aerosols (figure 4.9a), increased evaporation and an increase in latent heat (LH) flux which can be seen from figure 4.11a, where the shape of the area that sea ice was removed from is recognized.

The northernmost part of the study area also has an increase in the cloud droplet number concentration (CDNC), figure 4.10b, in the same area as is covered by the red patch indicating an increase in the LWP, which fits well with equation 2.13. There the amount of liquid water is proportional to the droplet number concentration, denoted by N in the equation, and the LWP is the vertically integrated LWC. The average increase in the CDNC would be approximately 1 or 2 droplets cm^{-3} in the northernmost area. Since CDNC is averaged over 24 hours and 11 layers (to a height of about 1800 m) the CDNC could be higher at certain times, and in certain layers.

The increase in effective radius in the same area as the LWP is increased also indicates the formation of new clouds, figure 4.10c, that could not form in the control run (see figure 4.3e).

In figure 4.10c, showing the difference in r_e , there are two red patches

between 140 and 155°W at 80 and 83°N, indicating an increase in droplet effective radius. Looking back to figures 4.3a and 4.3e of the LWP and r_e from day 1 in the control run, there were no low clouds at those locations. The increase in LWP at 83°N has already been mentioned, but there is also a slight increase in LWP at 80°N where the other pronounced difference in r_e is seen. These red patches of increased r_e are also clear in the difference in LW downward radiation at the ground surface, figure 4.12c. They can also be slightly recognized as a decrease in SW downward radiation in figure 4.12a. The SW radiation flux at ground surface has been reduced due to the increase in LWP, and the more pronounced decrease in downward SW is clearly recognized with the same shape and size as the northern patch of increase in LWP. This can be explained by equations 2.5 and 2.22, where it is clear from equation 2.22 that the cloud optical depth, τ , increases with LWP, and following equation 2.5 an increase in τ would also increase the cloud albedo.

The downward LW radiation flux at the surface (figure 4.12c) has been increased due to the increase in LWP and droplet size, which means that there is more water in the clouds and they emit more LW to the ground. It was shown in Chapter 2 that an increase in LWP increases the emissivity of the cloud, shown in equation 2.2, until the cloud is saturated with respect to LW radiation at about 40-45 g/m², following figure 2.2. Similarly, but opposite sign, the decrease in LW down at the surface, at 81°N 125-140°W, is recognized as a decrease also in LWP, CDNC and r_e (figures 4.10a, 4.10b and 4.10c). Thus there are less, or at least thinner, clouds in that area to emit LW. The decrease in LWP by ~9 g/m² (figure 4.10a) from ~40 g/m² in the control run (figure 4.3a) significantly decreases the cloud emissivity since it does not vary linearly and is below 40 g/m² (recall figure 2.2). The increase in the LW at TOA (figure 4.12d) is because of increased temperature at the surface when the sea ice is removed (figure 4.11c).

Of course, the removal of sea ice would reduce the SW at TOA, see figure 4.12b. The albedo of sea ice varies between 0.5 and 0.9 depending on snow cover and the age of the ice and is typically 0.5-0.7 for bare ice, whereas a typical ocean albedo is 0.06 [NSIDC, 2015]. Thus the change in SW at TOA is negative over the area of ocean where there was sea ice in the control run. The increased SW at TOA at 80°N and 155°W is because of the cloud forming in that area, see figure 4.12b, and can be recognized in the increase in r_e in the same place (figure 4.10c). This also gives an increase in LWP (figure 4.10a) and reduction in SW at surface (figure 4.12a) and increase of LW at surface (figure 4.12c). The signal in upward SW at TOA is due to the enhanced albedo caused by new clouds at that location, since these figures don't show in-cloud changes, simply the difference between the fields from the run without ice (NoIce) and the control run (Control).

A part of the decrease in SW down at the surface (figure 4.12a) has the same shape as that of decreased SW up at TOA (figure 4.12b), especially

around 75-80°N 110-135°W. The removal of sea ice has not just decreased the SW up at TOA by decreasing the albedo, but also the downward SW at the surface is decreased. Of the SW reflected by the sea ice, a fraction (depending on the clouds albedo) would be reflected back to the sea ice by the overlying lower clouds. This effect is lost when the sea ice is removed. Even though there is $\sim 2.4 \text{ W/m}^2$ less SW down at the surface, the SW that does reach the surface will have a warming effect compared to the control run, since the ocean has such a low albedo (0.06).

The heat fluxes and surface temperature are almost unchanged for most of the study area by the removal of sea ice, except for the area where the sea ice has been removed (see figures 4.11a, 4.11b and 4.11c). For much of the "sea ice removed area" the fluxes are higher than in the control run. This is not surprising, since one would expect the ocean surface to hold a higher temperature than the sea ice, therefore more heat is released than in the case when sea ice is present. This is true except for the blue area at 77-79°N and 115-125°W, also from which sea ice has been removed. This indicates a decrease in surface heat fluxes and surface temperature compared with the control run. This area of decrease in each of the figures, coincides with where the heat fluxes were higher than over the rest of the sea ice by ~ 5 to 10 W/m^2 in the control run, see figures 4.6a and 4.6b, and where the skin temperature was higher, see figure 4.7a. Thus the surface heat fluxes are approximately the same for the whole area which is now sea ice free, but had to increase and decrease in different areas. The same goes for the temperature, which was $\sim 2^\circ\text{C}$ higher in that area than the rest of the sea ice, in the control run. Now the surface is colder in there, about 0.9 to 1.5°C colder. The open ocean around has a temperature which is $\sim 1^\circ\text{C}$ warmer, thus evening out the difference in temperature between that and the area of decrease, leaving the whole "sea ice removed area" with approximately the same temperature. The average increase in skin temperature for the whole area is 0.1°C .

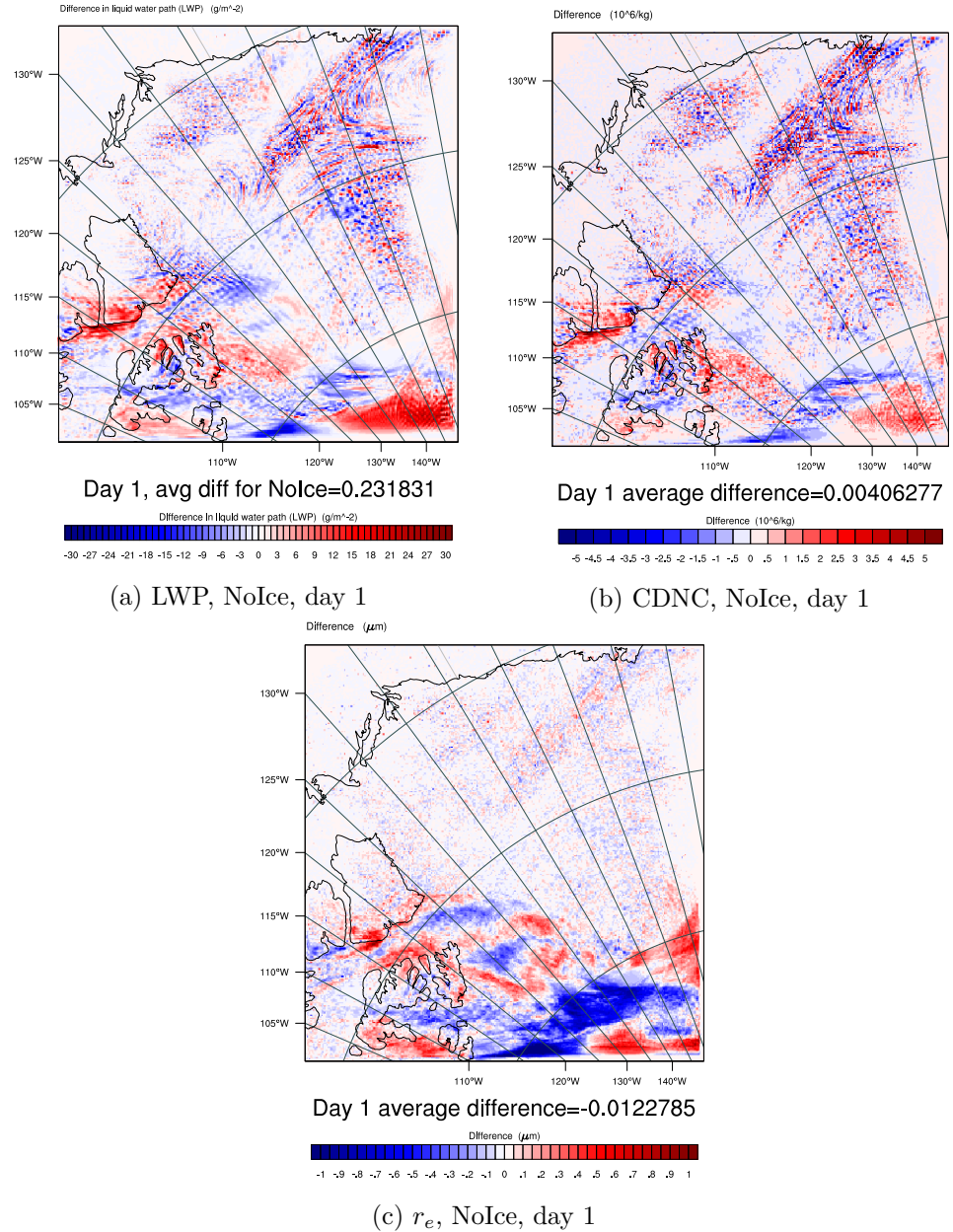


Figure 4.10: Difference in time averaged LWP, and in height and time averaged CDNC and r_e , for day 1. NoIce-Control.

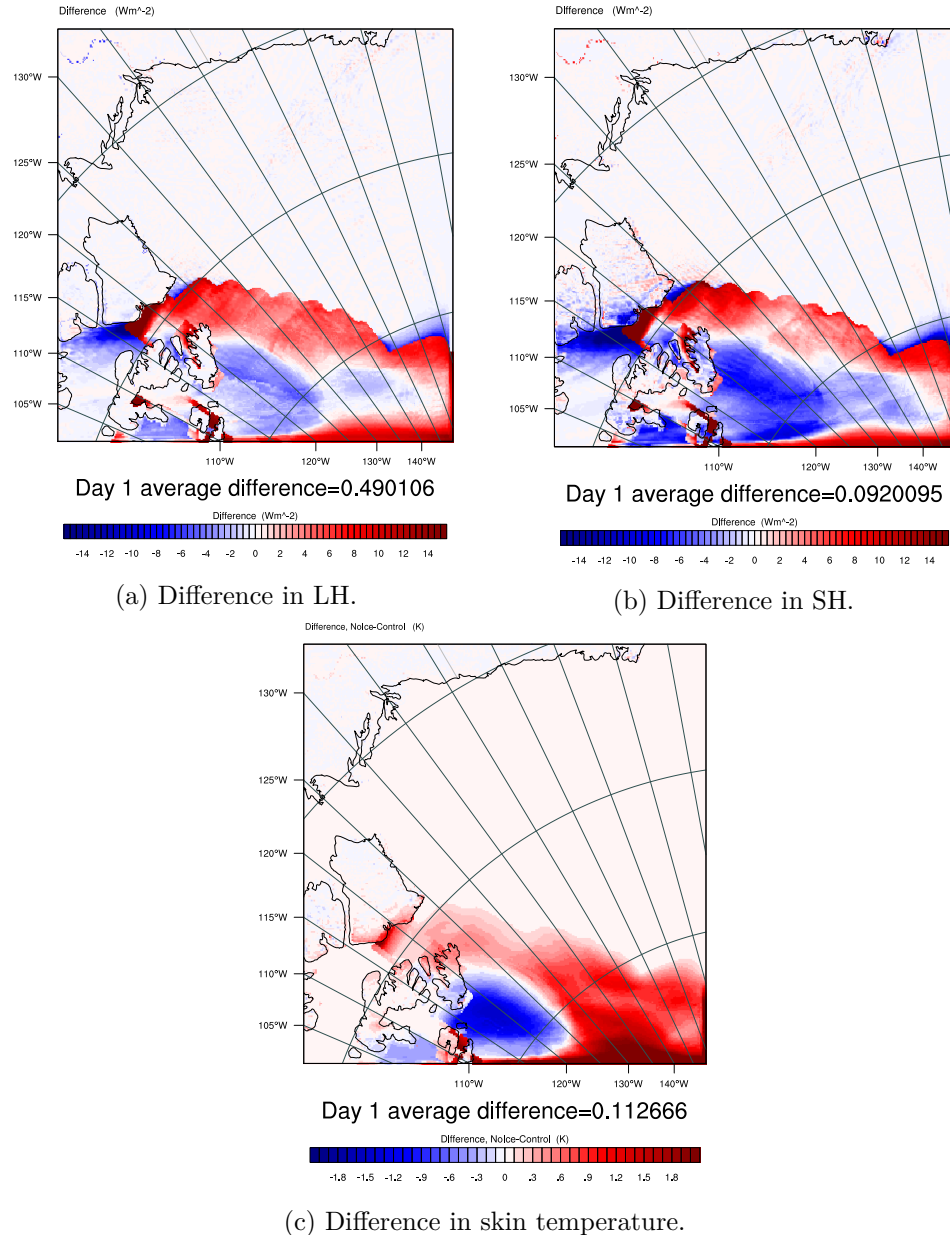


Figure 4.11: Difference in time averaged LH, SH and skin temperature for day1. NoIce-Control.

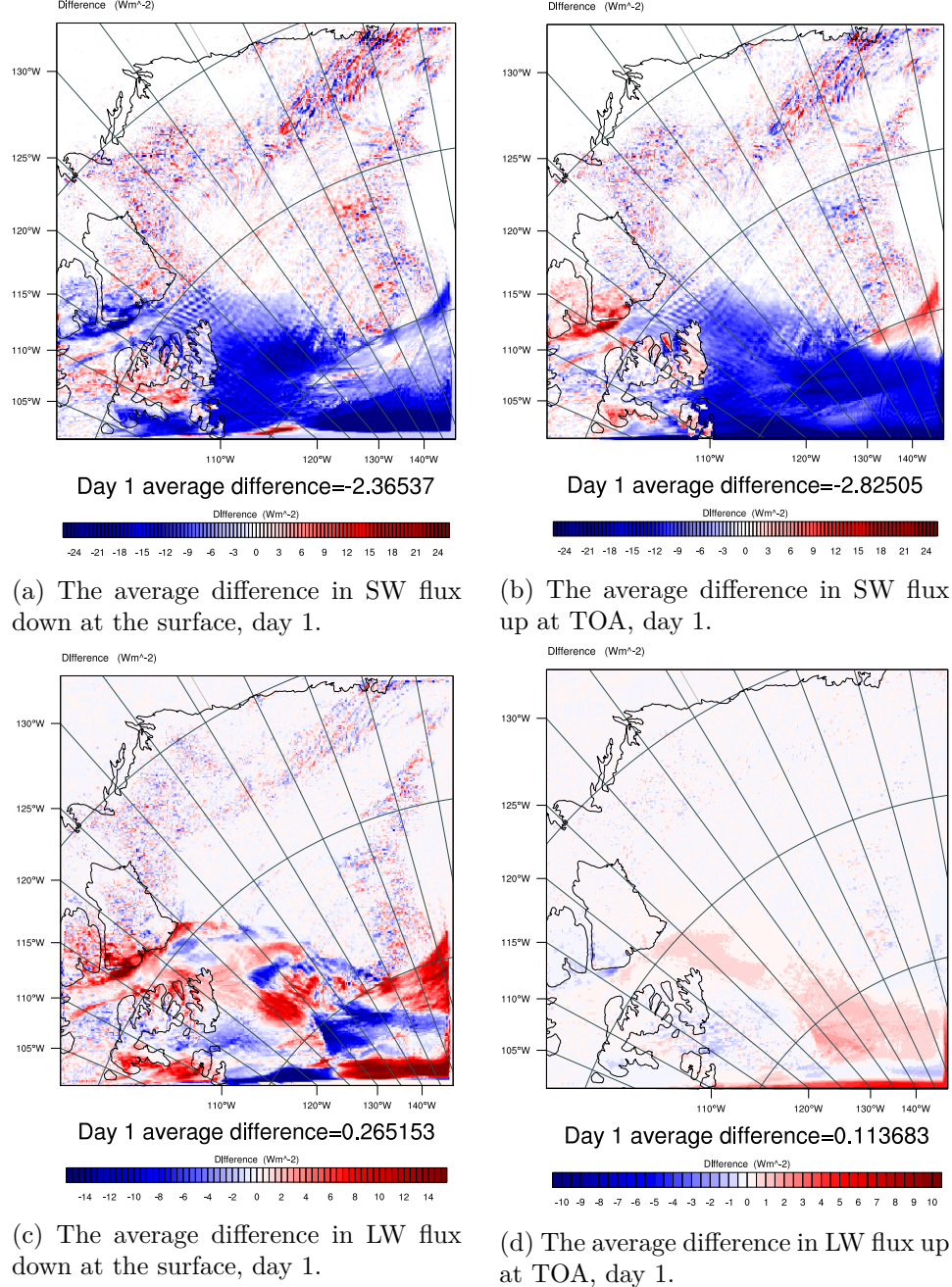


Figure 4.12: Difference in time averaged SW and LW flux down at the surface and up at TOA, for day 1. NoIce-Control.
Notice the different scales.

4.2.2 Day 5

The average differences for LWP, CDNC and r_e at day 5 are all negative, see figure 4.13, over the area that had ice in the control run. Thus the clouds making up the LWP in the control run, see figure 4.3b, have either ceased to exist, been significantly thinned, moved away or turned into ice. The LWP has a negative difference of $>15 \text{ g/m}^2$ for most of the "sea ice removed area", which means that the LWP, when comparing with the values for that area in the control run (figure 4.3b) which were around $40\text{-}100 \text{ g/m}^2$, there is still around $20\text{-}70 \text{ g/m}^2$ left. So the clouds have not all ceased to exist. This is supported by the fact that the CDNC in the control run was ~ 10 to 25 cm^{-3} and has according to figure 4.13b got 3 to >5 droplets cm^{-3} less in the run with no ice. Then the clouds in the run with no ice are left with <5 to around 20 droplets cm^{-3} which is definitely enough to assume that there are still clouds in the area.

There is hardly any ice at all in the study area in the lowermost 1800 m (not shown), and the IWP is zero (not shown) over the area where there was sea ice, and the area around. The wind pattern (not shown) is the same as in the control run (figure 4.1b), and the chance that the clouds have been moved to a different area is ruled out. Therefore precipitation must have depleted the clouds of some of the droplets. The difference in rain (not shown) for the run with no ice compared to the control run is negligible and so snow was found guilty of depleting the clouds. Figure 4.14 shows how the clouds that were claimed started to form in day 1 of the run with no ice, in section 4.2.1, did form and as more water vapor and aerosols were made available, more clouds developed and produced snow that performed natural cloud seeding, by making other clouds snow too.

Figure 4.14a shows the difference in mixing ratio of snow to air averaged for day 1 over the 11 lowermost layers. The slight increase in mixing ratio of snow is in the same area as the red patch in figure 4.13b that was claimed to be forming clouds. Figure 4.14b shows that in day 2 the clouds have indeed formed and as time passes more clouds form and produce snow through to day 5, see figure 4.14e where the positive difference in snow is less pronounced, but still present.

The clouds on the 5th day of the run with no ice are now significantly thinner than the clouds in the 5th day of the control run, due to the aforementioned reduction in CDNC. This allows for more of the upwelling LW at TOA to come directly from the surface (figure 4.15d), which holds a higher temperature than the atmosphere above (see cross section in figure 4.2c) and the newly ice free area also has a higher skin temperature, an increase of $\sim 1^\circ\text{C}$ compared to the control run, when there was sea ice there (see figure 4.16c). Following Stefan-Boltzmann's law (equation 2.1) the surface should then emit more LW than the clouds and sea ice with lower temperatures in the control run did. Figure 4.15d shows that the upwelling LW at

TOA has indeed increased by ~ 0.5 to 5 W/m^2 over the area where sea ice has been removed. Overall the average increase in upwelling LW at TOA for the whole area is just shy of 0.5, but the area of particular interest is where the sea ice has been removed, and that shows a more pronounced difference than the rest of the field.

In figure 4.15 the difference, for NoIce-Control, in SW down at the surface and up at TOA is illustrated by figures 4.15a and 4.15b. The upwelling SW at TOA (figure 4.15b) has an average difference of $\sim -3.3 \text{ W/m}^2$ for the whole field, and from <-25 to around -10 W/m^2 over the now ice free area. Such a decrease in upwelling SW radiation over the whole area that was covered by sea ice in the control run is because of the significant decrease in albedo of the area (not shown), which was discussed under day 1. The most pronounced decrease in upwelling SW at TOA at 77°N $120\text{-}140^\circ\text{W}$ is of same size and shape as the equally pronounced increase in downwelling SW at the surface of $>25 \text{ W/m}^2$ (figure 4.15a), in the same place. This can also be recognized as the most significant decrease in CDNC which has lost more than $5 \text{ droplets cm}^{-3}$ (figure 4.13b) compared to the control run. Thus, a cloud that was there in the control run has been significantly thinned or ceased to exist completely, such a decrease in CDNC (N in equation 2.4) decreases the cloud optical depth, τ , and albedo, A (equation 2.5), and does therefore not protect the surface from downwelling SW by reflecting it back to TOA.

The red patch at 77°N stretching from 120 to 140°W , in figure 4.15a, indicating the increase in downwelling SW is recognized as a decrease in downwelling LW in the same area in figure 4.15c. This can also be explained by the decrease in CDNC and the LWP. Looking at the difference in LWP in figure 4.13a, which shows LWP for NoIce-Control, one sees that the LWP in NoIce is $>30 \text{ g/m}^2$ less than in the control run for that exact area. The LW emissivity of the clouds decrease with the LWP (equation 2.2), provided the LWP is below the limit for saturation in the LW, which is $40\text{-}45 \text{ g/m}^2$ according to figure 2.2. The LWP in the control run (figure 4.3b) for that area was 30 to 60 g/m^2 . Thus the LWP in NoIce is below the limit for saturation in LW and the LW emissivity is decreased, explaining the decrease in LW reaching the surface in that particular area.

For quite a large part of the area which is now sea ice free the downwelling LW experiences an increase compared to the control run, see figure 4.15c. The depletion of clouds by snow, decreasing the LWP, would intuitively also decrease the downwelling LW at the surface if one considers the decrease in emissivity it would lead to, based on equation 2.2. On the other hand, knowing Stefan-Boltzmann's law (equation 2.1) the temperature of the emitting body is of crucial importance. The removal of sea ice has led to an increase in surface heat fluxes and skin temperature, as mentioned in day 1, and shows the same for day 5 in figure 4.16.

A higher skin temperature and increased surface heat fluxes causes warmer

air to rise, and convection rises the lower cloud base higher up into the atmosphere. The cloud height for a section of the area can be seen in the vertical cross section for LWC on day 5 4.17 for the run with no ice. Comparing this with the vertical cross section from the control run, figure 4.2c, it is clear that the stratus clouds lie approximately 500 m higher, closer to the mountain in the run without sea ice than they did in the control run.

Looking closely at vertical cross sections from NoIce (figure 4.17) and Control (figure 4.2c) the clouds in NoIce have a higher temperature at the core (-9°C), where there is most liquid water, than in Control (-9 to -10°C). This increase in temperature allow the clouds to emit more LW to the ground surface, following Stefan-Boltzmanns law (equation 2.1) than in Control, despite the decrease in LWP that lowers the cloud emissivity (equation 2.2). On the other hand, in NoIce the clouds do not stretch as close to the mountain as in Control, and at 77°N and 117°W (between 100 and 120 on the x-axis) NoIce has no cloud, which fits with the decrease in downwelling LW in that area.

The increase in surface fluxes from the area where sea ice was removed, shown in figure 4.16, is accompanied by a significant decrease over the ocean outside where the sea ice used to be. Recall that the strong winds in that area made the surface heat fluxes significantly higher over the ocean than over the ice, compared to day 1 (figure 4.6). The wind pattern in NoIce (not shown) is the same as in Control, but since the sea ice is not there, the air being brought over that area is no colder than further out over the ocean and does therefore not experience the same difference in temperature gradient as when the sea ice was there. Thus, removal of sea ice releases more latent and sensible heat, and gives a higher skin temperature (~0.6 to 2 °C increase) in that area. With an increase of ~2 °C the skin temperature (where there used to be sea ice) reaches almost the same skin temperature as the open ocean (figure 4.7b), thus reducing the temperature gradient between the skin temperature and the overlying air. Therefore there is no marked increase in the surface fluxes off the sea ice edge, and it is shown as a decrease compared to Control, for both LH and SH (figures 4.16a and 4.16b).

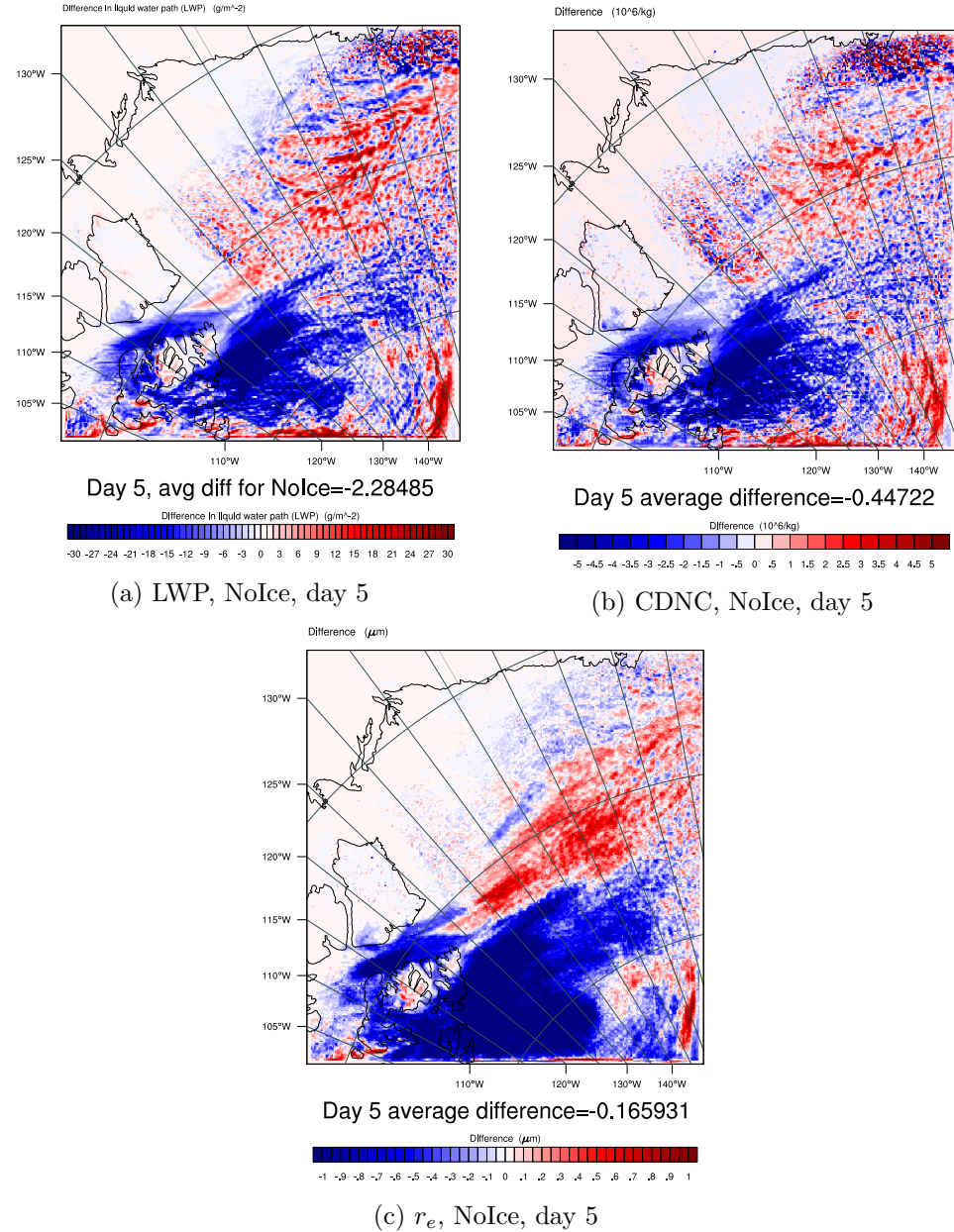


Figure 4.13: Difference in time averaged LWP, and in height and time averaged CDNC and r_e , for day 5. NoIce-Control.

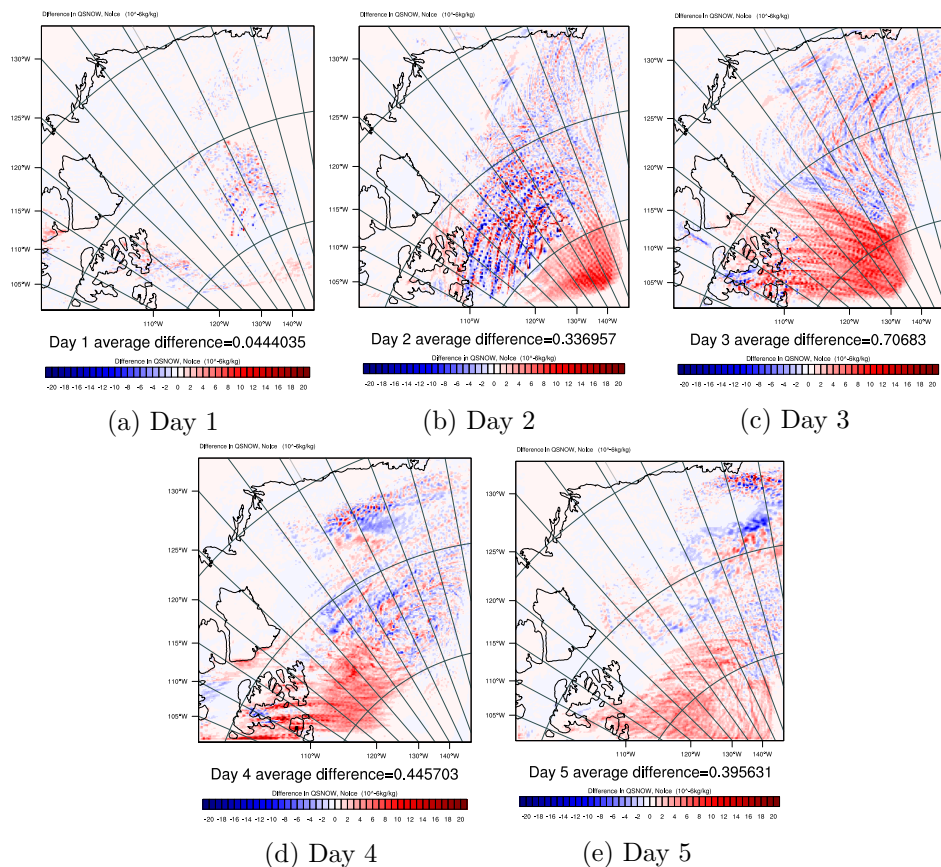


Figure 4.14: Difference in time and height averaged mixing ratio of snow to air, for days 1 to 5. NoIce-Control.

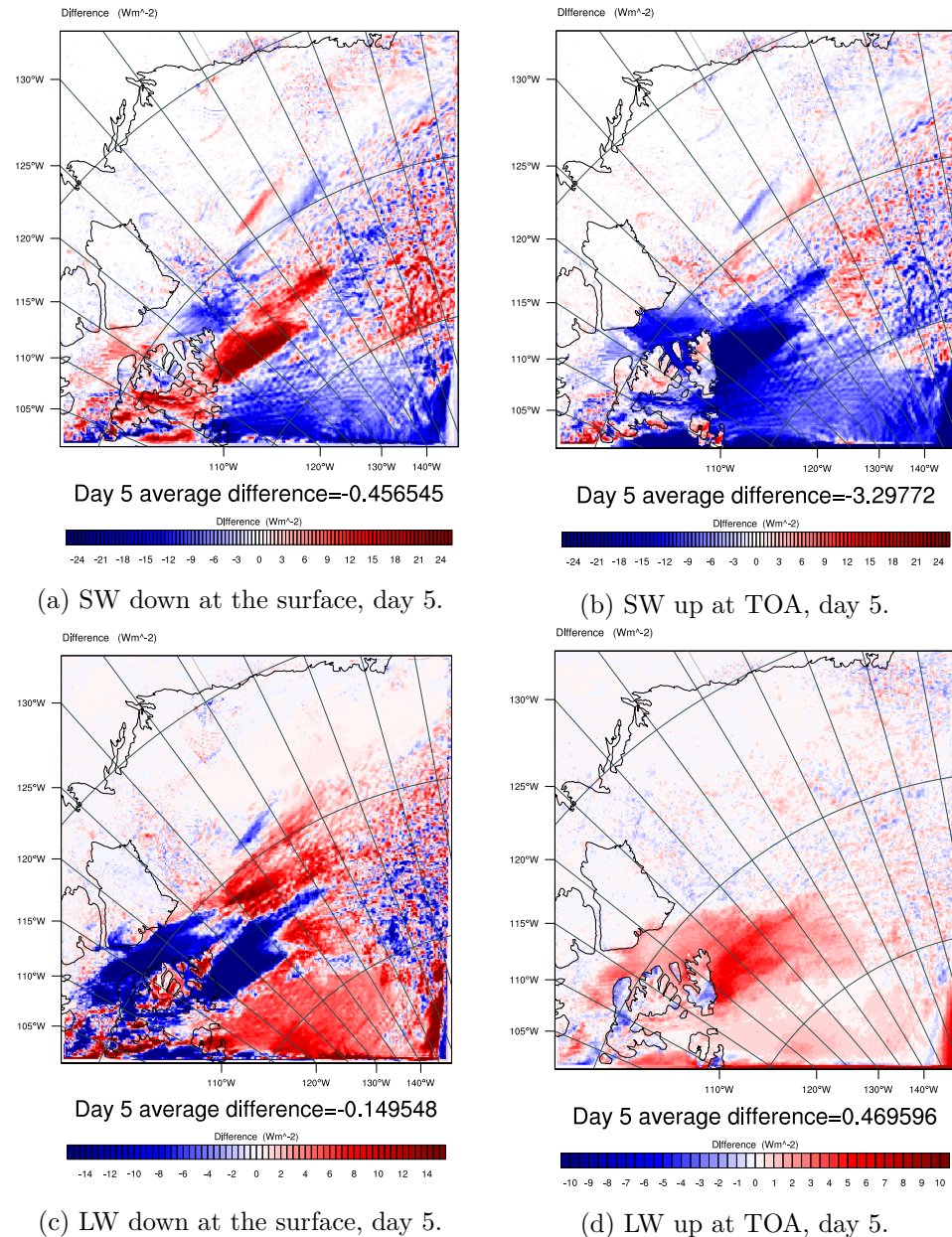


Figure 4.15: Difference in time averaged SW and LW flux down at the surface and up at TOA, for day 5. NoIce-Control. Notice the different scales.

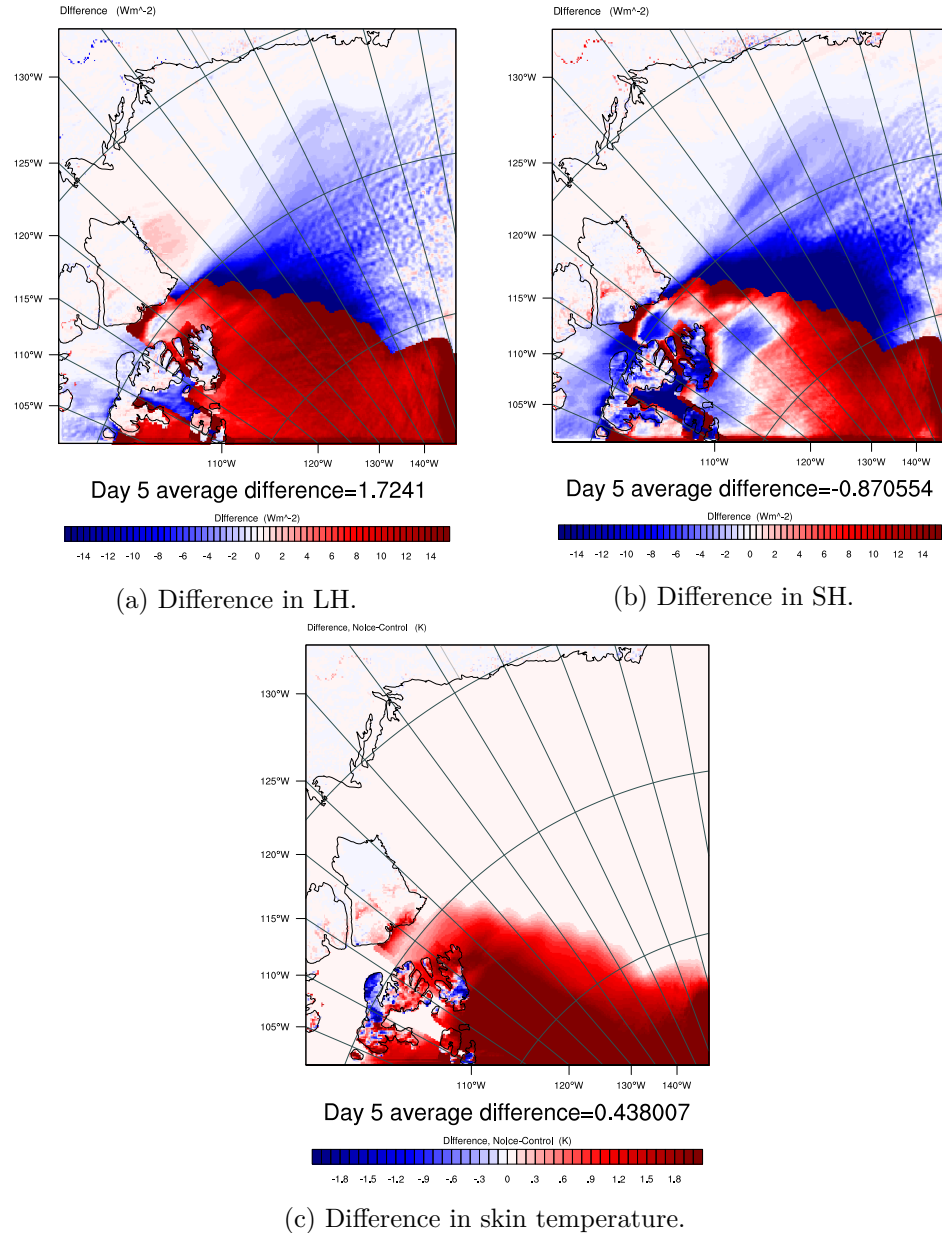
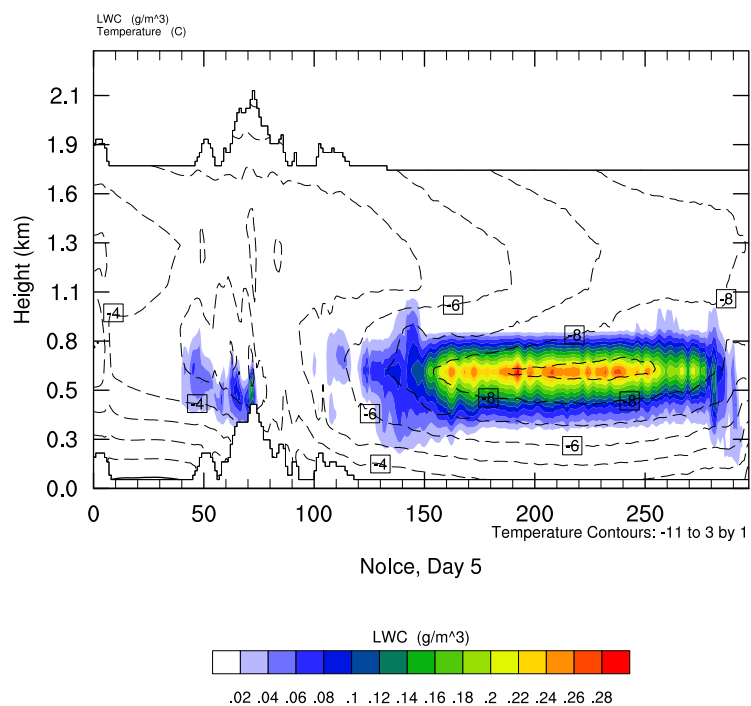


Figure 4.16: Difference in time averaged LH, SH and skin temperature for day 5. NoIce-Control.



4.3 Increased aerosol number concentration

The aerosol number concentration was multiplied by 10 to study the effects of pollution in the area. The increased ship traffic in the Arctic leads to higher aerosol loads [Eckhardt *et al.*, 2013], which could affect the cloud radiative properties and thereby have a warming or cooling effect at the surface. Figure 4.18 shows the number concentration for water-friendly aerosols in day 1 of Control and Aero10, where the pattern obviously is almost identical, and overall increased by a factor of 10 (notice the different scales).

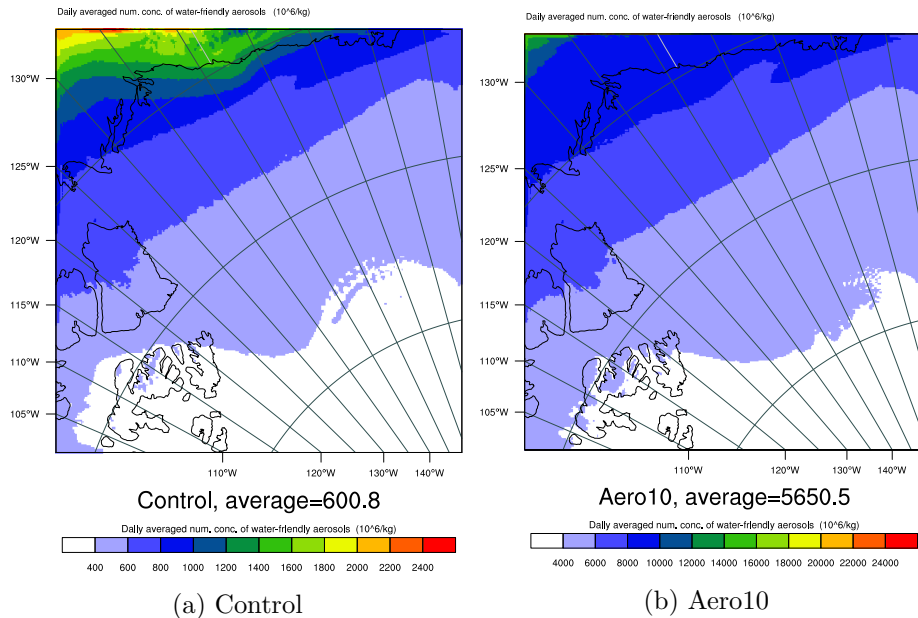


Figure 4.18: Number concentration of water-friendly aerosols in day 1. In Control and Aero10. Notice the different scales.

4.3.1 Day 1

With an aerosol number concentration 10 times higher than that in the control run, the average LWP and CDNC for day 1 increase by about 11 g/m^2 and 16 cm^{-3} respectively, see figure 4.19. The increases in CDNC and LWP are expected with such a high increase in available CCN. The highest increases in LWP and CDNC is where the LWP and CDNC was highest in the control run (figures 4.3a and 4.3c respectively), $74\text{-}78^\circ\text{N } 145\text{-}155^\circ\text{W}$ and $71^\circ\text{N } 140\text{-}150^\circ\text{W}$. This increase in time averaged LWP and CDNC indicates that the clouds are denser and longer lived, thereby increasing there reflectance of SW (figure 4.20a). This is known as the second indirect effect (recall from Chapter 2).

Remembering the first indirect effect (also described in Chapter 2), one would expect a decrease in droplet size with the increase in numbers. r_e has in fact decreased for the whole field in this run, with an average decrease of $0.5 \mu\text{m}$, and is shown in figure 4.19c

The first indirect effect describes an increase in the cloud albedo as a consequence of more numerous and smaller droplets, and the upwelling SW at TOA is increased by as much as 7.3 W/m^2 on average for the whole field on day 1 (see figure 4.20b). As opposed to the run with no ice, the sea ice is unchanged in the run with increased aerosol number concentration (Aero10), so the signal here is clearly an increase in reflected SW. Over the sea ice however, the increase in reflected SW is not as large as in the rest of the field, since the sea ice already has a relatively high albedo itself (around 0.6). The increase in the albedo of the clouds has significantly reduced the downwelling SW at the surface (figure 4.20a) compared to the control run. The change is $\sim 9.3 \text{ W/m}^2$ decrease on average for the study area, which represents a cooling. On the other hand the average LW radiation at the surface is higher (figure 4.20c) due to the aforementioned increase in LWP and thereby increased emittance by the clouds, as follows from equation 2.2. The increase in LW reaching the surface is $\sim 2.3 \text{ W/m}^2$. The most pronounced increase in LW down at the surface is in areas where the LWP in the control run (figure 4.3a) was lower and therefore not as close to saturation with respect to cloud LW emissivity. Two of these areas are $79^\circ\text{N}, 130\text{-}140^\circ\text{W}$ and $82^\circ\text{N}, 125\text{-}145^\circ\text{W}$. The decrease in upward LW at TOA (figure 4.20d) is due to lower emittance of LW from the clouds than from the surface, since they have lower temperatures than the surface. The vertical temperature distribution over the red line in figure 4.2d can be seen as dashed contours in figure 4.21, which also shows the LWC as filled contours. The scales are different, but comparing with figure 4.2a, showing LWC in the same section from Control, one can see that the LWC has increased in the clouds seen in the section. The vertical distribution of the clouds is the same for both runs, and the clouds formed by orographic lifting over the mountain have higher LWC than in the control run, since more CCN are activated and allowed to grow into cloud droplets. Thus, the clouds are responsible for more of the LW reaching TOA than in the control run.

The LW cloud emissivity is sensitive to an increase in water amount for LWP less than $\sim 40\text{-}45 \text{ g/m}^2$. Day 1 in the control run had LWP around $50\text{-}150 \text{ g/m}^2$ at $72\text{-}79^\circ\text{N} 115\text{-}125^\circ\text{W}$. This is also seen in that there is no significant change in LW downward at the surface in that area, see figure 4.20c. This area with lack of change in LW down is approximately the same area as where there is a negative change in LH and SH upward from the surface over the sea ice, and where the skin temperature has decreased ($\sim -0.2^\circ$), see figure 4.22. Since there has been no change in LW at that location there is no warming or cooling effects from the LW, but the change can be explained

by the changes in SW radiation. The downward SW at the surface has been significantly decreased (-9.2 W/m^2) as a consequence of the increase in aerosol number concentration, see figure 4.20a.

The albedo of the sea ice in Aero10 is around 0.6 (not shown) which means that a fraction of the incident SW radiation is absorbed. Since the amount of incident SW radiation at the surface has been reduced by the cloud cover, the absorbed radiation is less than for a higher incident amount. The ice therefore has a lower temperature (figure 4.22c) decreasing the temperature gradient between the surface and the overlying air, thus decreasing the upward surface heat fluxes.

The skin temperature, figure 4.22c, shows that there is an increase over the sea ice, where the surface heat fluxes increase ($79^\circ\text{N } 130\text{-}140^\circ\text{W}$ and $82^\circ\text{N } 115\text{-}145^\circ\text{W}$). These areas coincide with the previously mentioned increase in LW down at the surface (figure 4.20c), where the clouds in the control run were not saturated with respect to LW (figure 4.3a). An increase in LW down at the surface has a warming effect.

Parts of Canada, islands at $73^\circ\text{N } 115\text{-}125^\circ\text{W}$ and $75\text{-}77^\circ\text{N } 105\text{-}120^\circ\text{W}$, and $68^\circ\text{N } 128\text{-}133^\circ\text{W}$, and the part of the domain that is in Alaska ($70^\circ\text{N } 140\text{-}158^\circ\text{W}$) experience a decrease in skin temperature, $>0.5^\circ\text{C}$, compared to the control run (figure 4.22c), but the ocean does not. These areas are also where the reduction in downward SW at the surface is most significant (figure 4.20a), and overpower the the increase in LW down at the surface (figure 4.20c). It was shown in Chapter 2, that when a cloud is saturated with respect to LW (as a function of LWP) the albedo of the clouds become increasingly important, figure 2.2. Since land has lower heat capacity than the ocean, it responds faster to changes in the downward radiation at the surface. In this study there would be no effect on the sea surface temperatures (SSTs) anyway, because they are constant and the same for all the four runs (Control, NoIce, Aero10, Aero10NoIce). The increase in temperature seen from the removal of sea ice earlier in the chapter (figures 4.11c and 4.16c) were simply an adjustment to the SSTs downloaded from ECMWF.

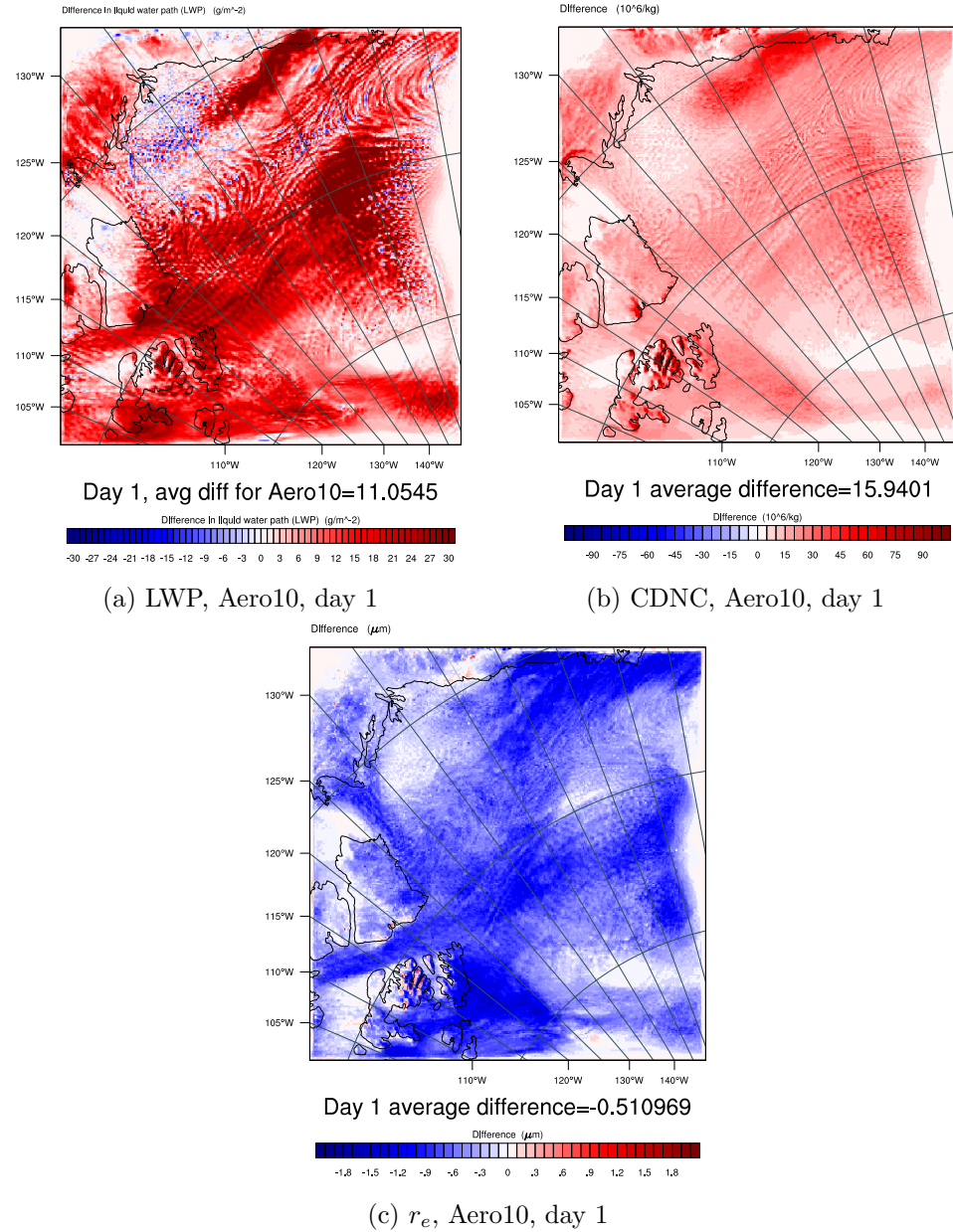


Figure 4.19: Difference in time averaged LWP, and in height and time averaged CDNC and r_e , for day 1. Aero10-Control.

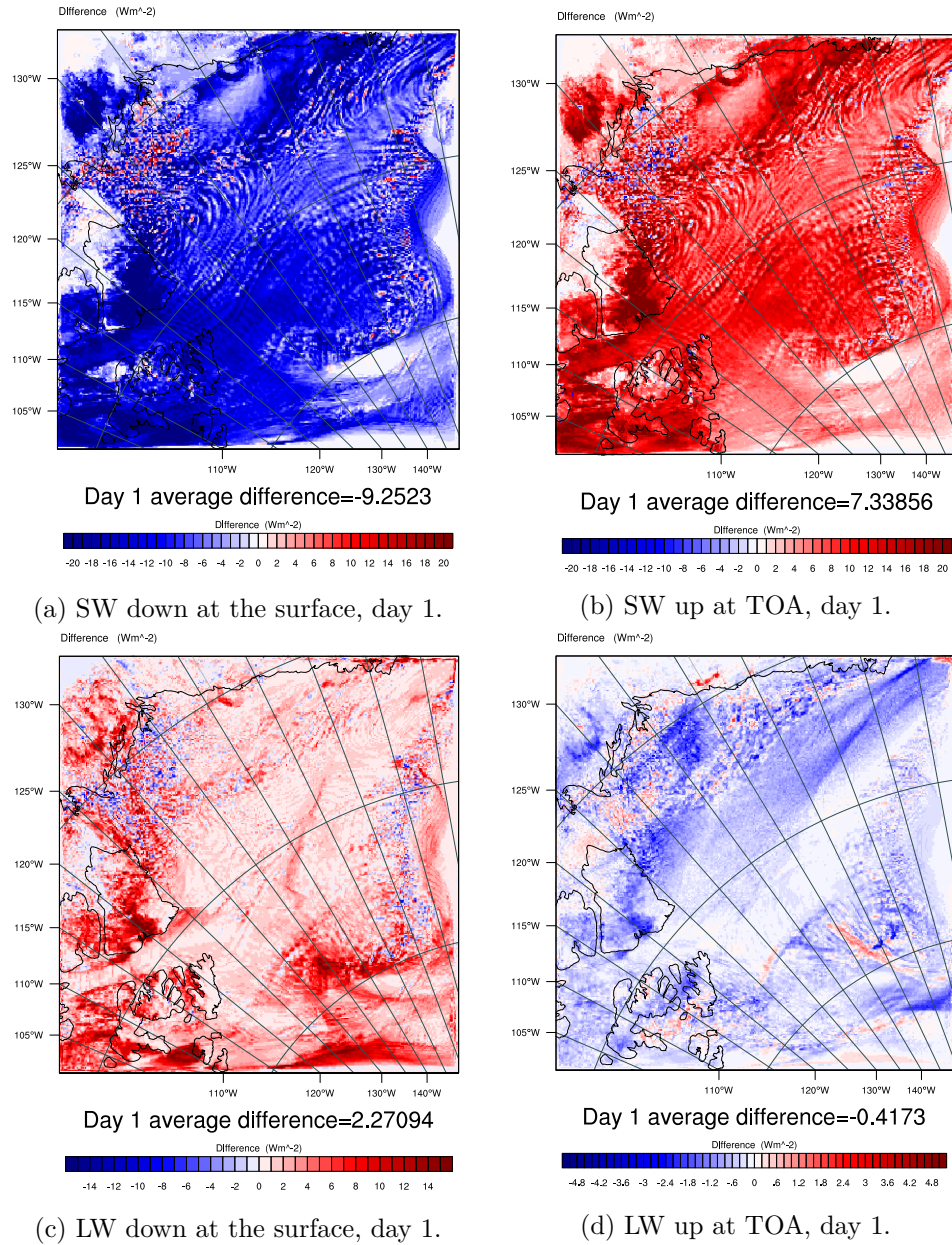


Figure 4.20: Difference in time averaged SW and LW flux down at the surface and up at TOA, for day 1. Aero10-Control.
Notice the different scales.

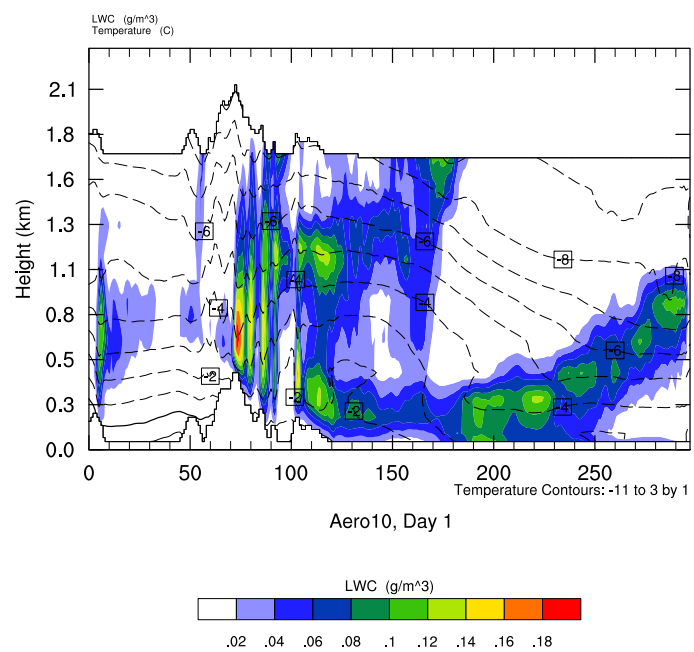


Figure 4.21: Time averaged LWC as filled contours, and temperature as dashed contours, in the vertical cross section over the red line in figure 4.2d. Day 1 of Aero10.

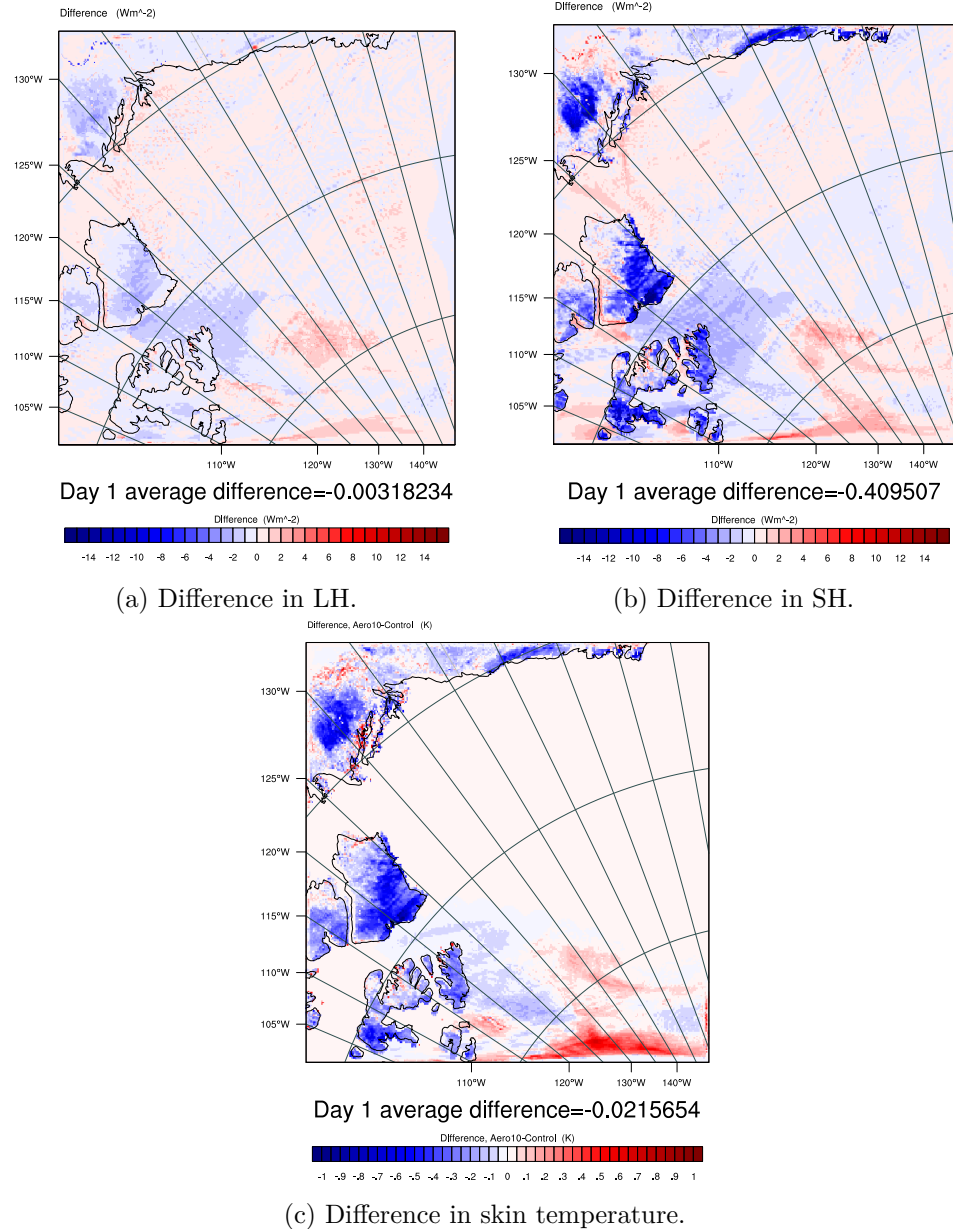


Figure 4.22: Difference in time averaged LH, SH and skin temperature for day 1. Aero10-Control.

4.3.2 Day 5

The differences in LWP and CDNC and r_e for day 5 (Aero10-Control) are shown in figure 4.23. As for day 1, the LWP shows an average increase for the whole study area. The increase in LWP on day 5 in Aero10 compared to Control is $\sim 20 \text{ g/m}^2$ and is especially high where the LWP was also high in the control run (see figure 4.3b). The increase in CDNC has the same pattern as the increase in LWP, which is expected based on equation 2.13. The average increase in CDNC for the study area is $\sim 22 \text{ cm}^{-3}$. Similarly to day 1, evidence of the first indirect effect is suspected since r_e has an average decrease of $\sim 0.6 \mu\text{m}$, which means that still for day 5 there are more numerous and smaller droplets. Also for r_e the pattern is the same as for LWP, but with opposite sign.

Which means that for day 5 the first indirect effect is expected – a higher cloud albedo as a consequence of more numerous and smaller droplets, and according to figure 4.24a the cloud albedo has indeed increased. On average for the whole study area the upward SW at TOA has increased by $\sim 7 \text{ W/m}^2$. Also here the increase in reflected SW is less over the sea ice. As expected, the SW down at the surface is then decreased for the whole field, with an average decrease of 8.6 W/m^2 .

Day 5 in the control run had LWP around $60\text{-}100 \text{ g/m}^2$ in the middle lower area of figure 4.3b ($72\text{-}85^\circ\text{N } 110\text{-}140^\circ\text{W}$) and up to almost 300 g/m^2 at $75\text{-}72^\circ\text{N } 130\text{-}160^\circ\text{W}$. Recall that this indicated saturation with respect to LW, which is also seen in that there is no significant change in LW downward at the surface in those areas, see figures 4.24c.

The area with lack of change in LW down ($72\text{-}85^\circ\text{N } 110\text{-}140^\circ\text{W}$) is approximately the same area as where there is a negative change in LH and SH upward from the surface over the sea ice, and where the skin temperature has decreased, see figure 4.25. Also for day 5 this change can be explained by the changes in SW radiation. The downward SW at the surface has been significantly decreased (-8.6 W/m^2) as a consequence of the increase in aerosol number concentration, see figure 4.24a.

Following the same reasoning as for day 1: Because of the first indirect effect, the cloud albedo has increased, and there is less SW down at the surface for the sea ice to absorb. The ice therefore has a lower temperature (figure 4.25c) decreasing the temperature gradient between the surface and the overlying air, thus decreasing the upward surface heat fluxes.

The skin temperature, figure 4.25c, for the domain shows a decrease ($\sim 0.5^\circ\text{C}$) in the same area as where there is less sensible and latent heat release over the sea ice, but it also shows a decrease over land. The Canadian islands at $73^\circ\text{N } 115\text{-}125^\circ\text{W}$ and $75\text{-}77^\circ\text{N } 105\text{-}120^\circ\text{W}$, and Alaska at $70^\circ\text{N } 140\text{-}158^\circ\text{W}$, experience a decrease in skin temperature compared to the control run, but the ocean does not. Again this is because the land has lower heat capacity than the ocean (and that the SSTs are constant).

For the area north of 75°N where the clouds were not saturated with respect to LW, the pattern of increase in latent and sensible heat (figures 4.25a and 4.25b) can be recognized as the areas of increase in LW down at the surface (figure 4.24c).

In this case, with reduced SW down at the surface and lower skin temperatures, the increase in aerosol number concentration has a cooling effect at the surface.

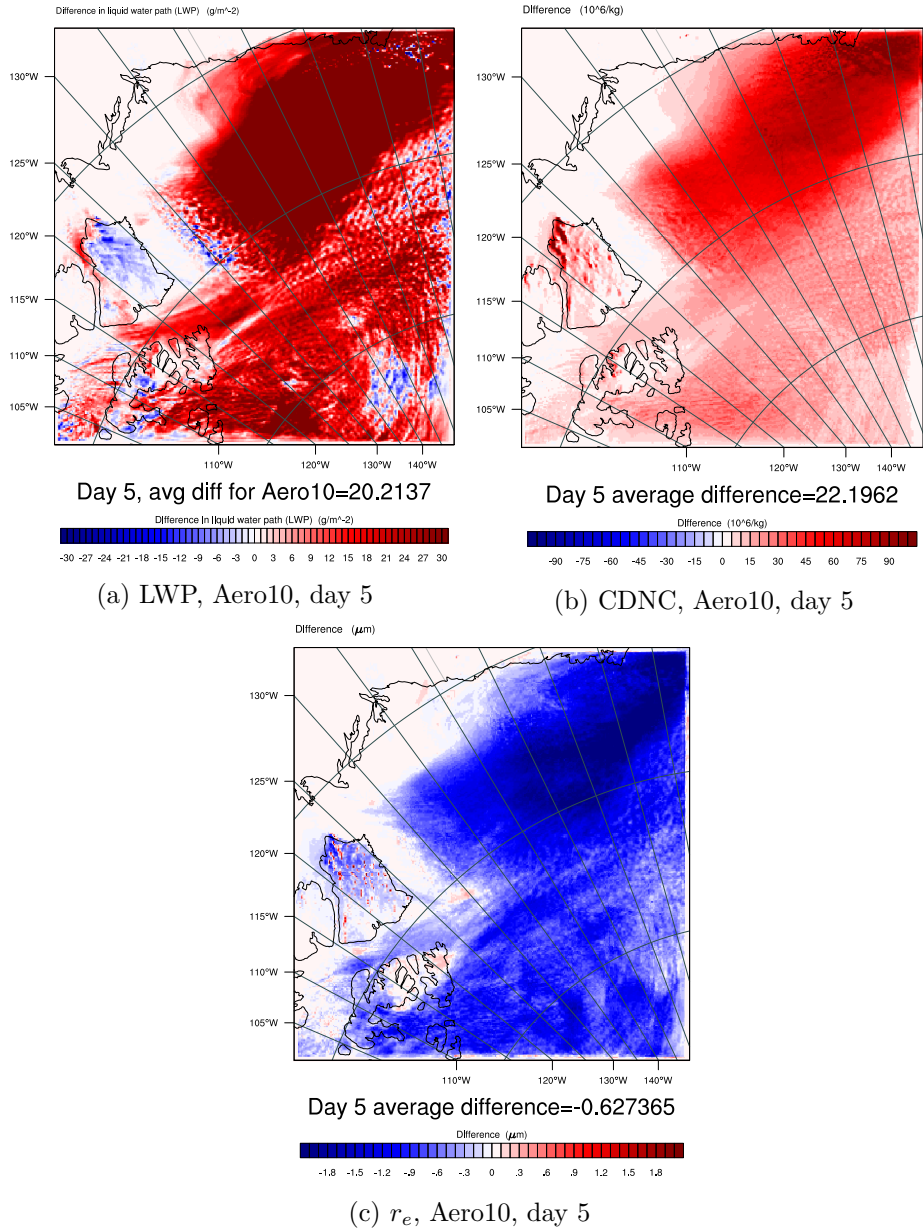


Figure 4.23: Difference in time averaged LWP, and in height and time averaged CDNC and r_e , for day 5. Aero10-Control.

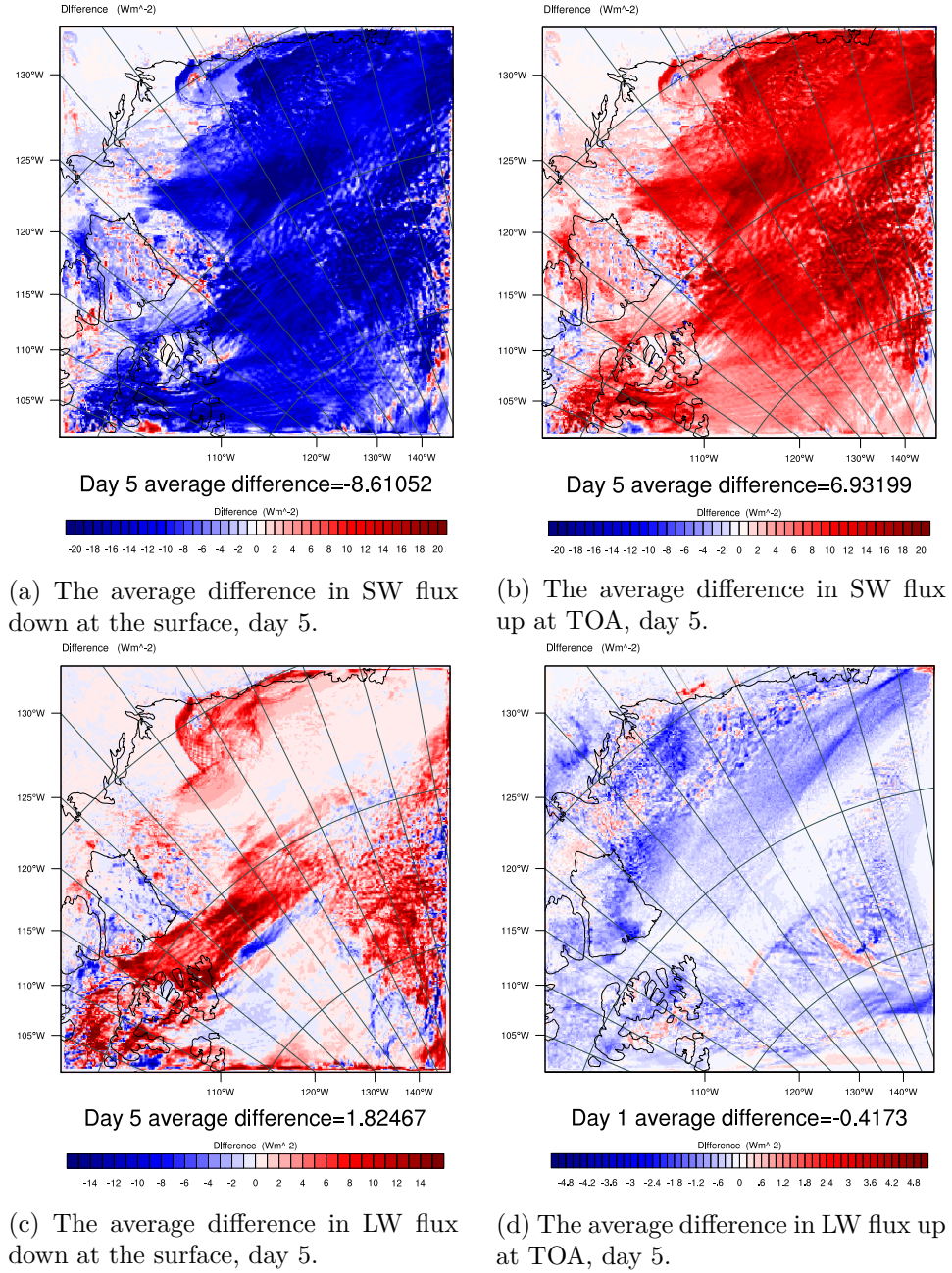


Figure 4.24: Difference in time averaged SW and LW flux down at the surface and up at TOA, for day 5. Aero10-Control. Notice the different scales.

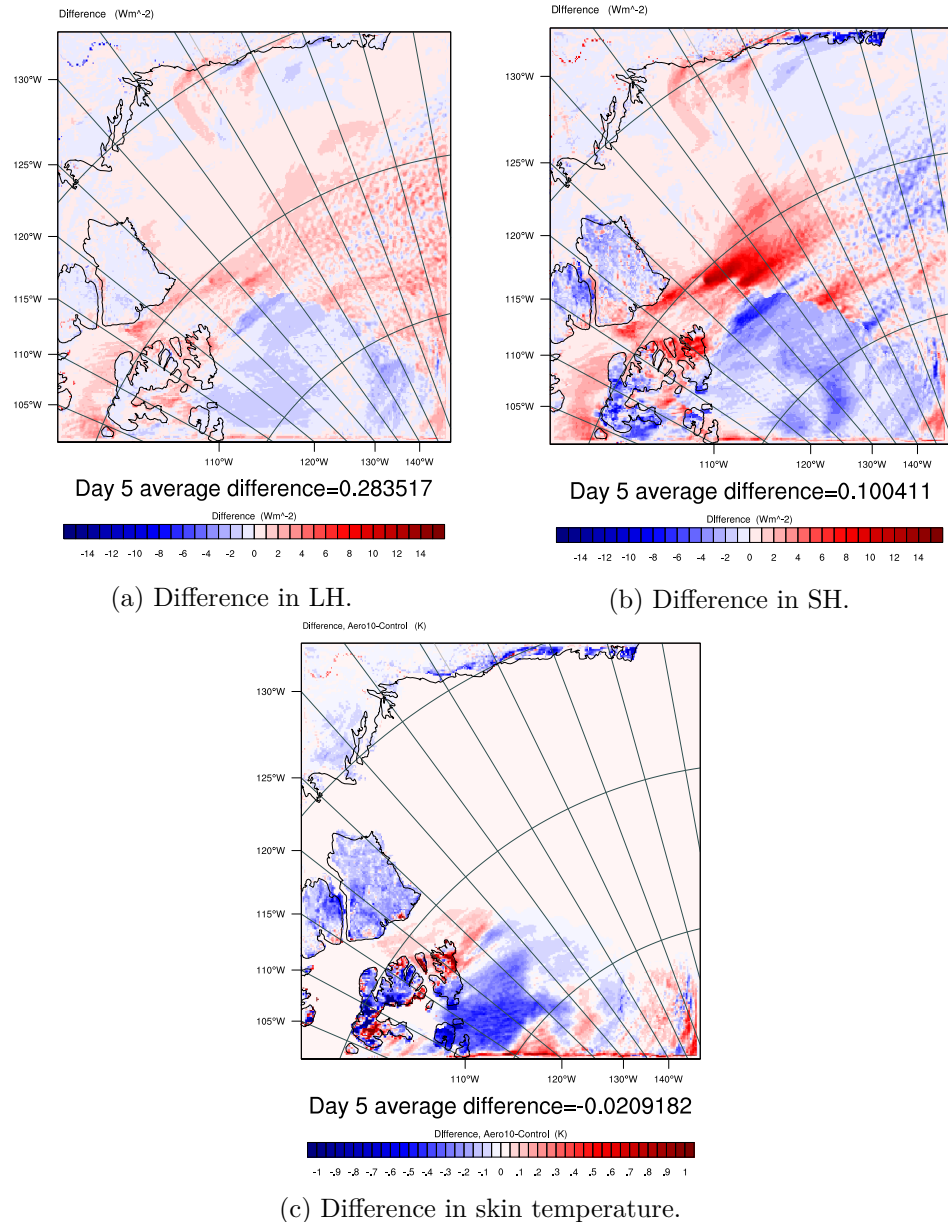


Figure 4.25: Difference in time averaged LH, SH and skin temperature for day 5. Aero10-Control.

4.4 Removed sea ice and increased aerosol

The effects on radiative cloud properties and the surface by removal of sea ice and increased aerosol number concentration is studied combined. This is to get an idea of the effects of increased pollution from sea traffic as a consequence of more ice free ocean, in combination with more available heat and moisture from the ocean. The results in this section are not discussed as detailed as the results presented in the two previous sections for NoIce and Aero10 separately. This is to avoid too much repetition of the mechanisms behind the differences.

4.4.1 Day 1

The difference in LWP between the run with both removed sea ice and increased aerosol number concentration (Aero10NoIce) and Control for day 1 (figure 4.26a) is clearly due to the increase in number of aerosols. The increase in LWP for day 1 in NoIce (figure 4.10a) was on average $\sim 0.2 \text{ g/m}^2$ for the whole field, whereas for Aero10 it was 11 g/m^2 , which is also the average increase for Aero10NoIce. The average increase in CDNC (figure 4.26b) for Aero10NoIce is also similar to Aero10 (figure 4.19b) where both those runs had an average increase of $\sim 15.9 \text{ cm}^{-3}$. The difference in effective radius is also the same with an average decrease in droplet size of about $0.5 \mu\text{m}$ (see figure 4.26c for Aero10NoIce and 4.19c for Aero10). For these specific parameters it is clear that the effect of increasing the aerosol number concentration outweighs that of removing the sea ice.

When looking at the difference in radiation fluxes down at the surface and up at TOA (figure 4.27) one can see that both the removal of sea ice and the increase in aerosol number concentration make a difference. For downward SW at the surface (figure 4.27a) the average difference can be interpreted as a sum of the difference in NoIce and Aero10. NoIce and Aero10 had average decreases in SW down of $\sim 2.36 \text{ W/m}^2$ (figure 4.12a) and $\sim 9.25 \text{ W/m}^2$ (figure 4.20a) respectively. When added together they are almost equal to the average difference in Aero10NoIce, which is a decrease of 11.6 W/m^2 . Such a decrease in downwelling SW radiation should have a cooling effect at the surface.

It can be seen from figures 4.28a, 4.28b and 4.28c showing LH, SH and skin temperature respectively, that there is a decrease in upward surface fluxes and temperature of the surface at $77\text{-}79^\circ\text{N}$ and $115\text{-}125^\circ\text{W}$, which was explained by the adjustment to SSTs in the area that had sea ice. As the sea ice is removed the temperatures in that area are set to the SSTs and for the higher temperature over the sea ice, that meant a reduction in temperature, but for most of the area that had sea ice the skin temperature is increased. This is expected since the sea surface normally has a higher temperature than ice. Where the temperature is higher, so is the release of

sensible and latent heat, and it is lower where the temperature is lower (see figures 4.28a and 4.28b). The decrease in temperature over land has been explained (in the previous section about Aero10) by the increase in aerosol number concentration leading to a significant reduction in downward SW at the surface (figure 4.27a). Due to the low heat capacity of land compared to water, the land experiences a cooling and the sea surface does not. (Also the SSTs are constant, and would not be affected by any changes in any of the runs in this thesis.)

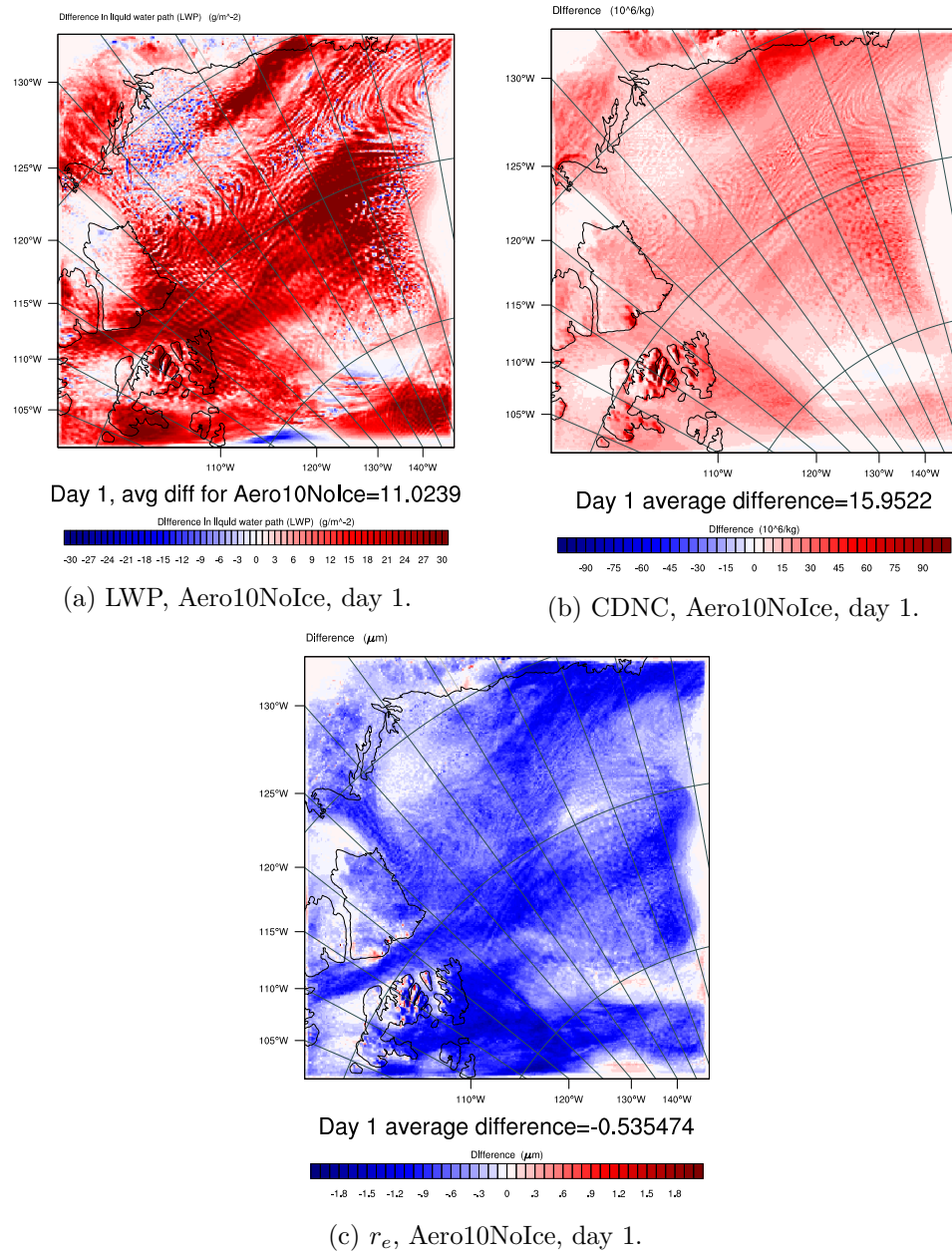


Figure 4.26: Difference in time averaged LWP, and in height and time averaged CDNC and r_e , for day 1. Aero10NoIce-Control.

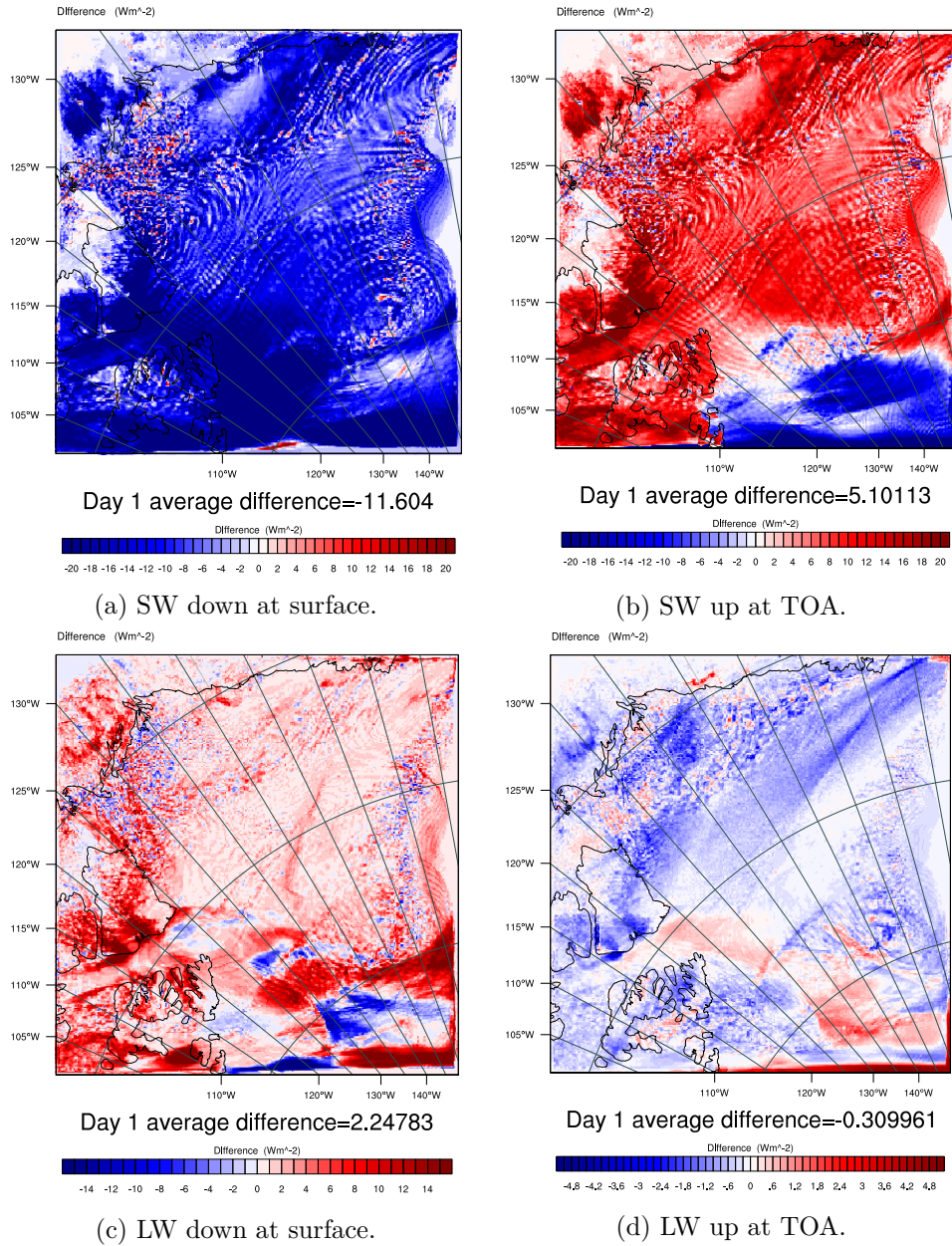


Figure 4.27: Difference in time averaged SW and LW flux down at the surface and up at TOA, for day 1. Aero10NoIce-Control. Notice the different scales.

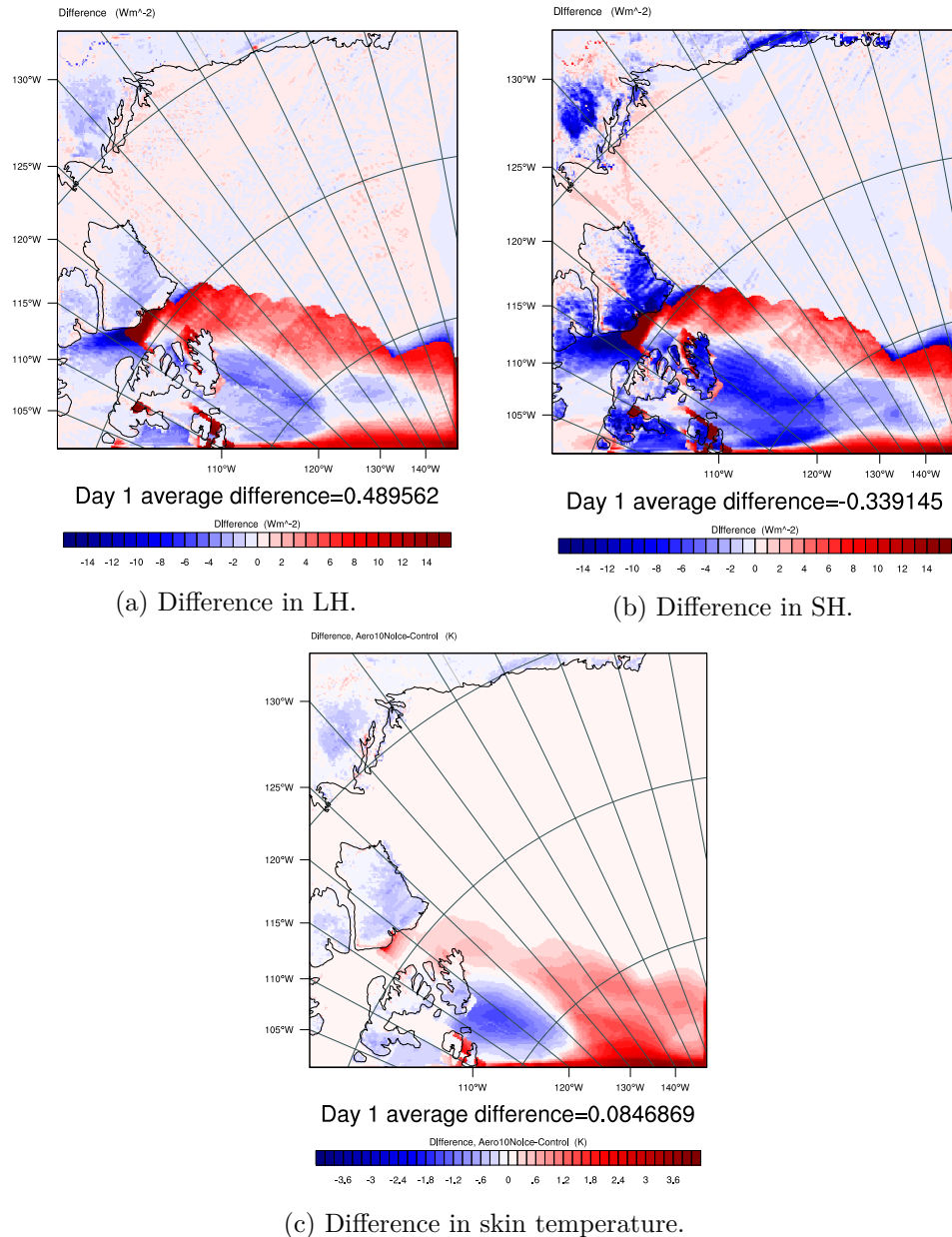


Figure 4.28: Difference in time averaged LH and SH up at the surface, and skin temperature, for day 1. Aero10NoIce-Control.

4.4.2 Day 5

On the last day of the run, day 5, the atmosphere has had time to adapt to both the sea ice changes and the changes in aerosol number concentration. The increase in LWP of $>25 \text{ g/m}^2$ (south of 75°N and west of 130°W in figure 4.29a) is recognized as the area that had highest LWP in the control run (figure 4.3b) and experienced an increase in NoIce (figure 4.13a), but a more significant increase as a consequence of more available CCN in Aero10 (figure 4.23a). Due to snow, the LWP in NoIce was negative on average (figure 4.13a), and also here it can be seen that precipitation has significantly reduced the LWP over a part of where there was sea ice (77°N $115\text{--}130^\circ\text{W}$). The increase in available moisture and surface temperatures, see figures 4.31a and 4.31c, from the removal of sea ice gives increased convection, and production of more precipitating clouds. Thus the average increase in LWP of 16.7 g/m^2 is a combined effect of the increase in CCN increasing the LWP, which is known to be proportional to the CDNC (recall equation 2.13), and the decrease in LWP, that more convection and precipitation has led to through removal of sea ice.

The most pronounced decrease in LWP (77°N $115\text{--}130^\circ\text{W}$), has here as in NoIce, opened up for a significant increase of $\sim 20 \text{ W/m}^2$ in SW down at the surface at that location, seen as the only red patch in figure 4.30a. Since the ocean albedo is 0.06, and not 0.6 as it was for the sea ice, the SW up at TOA has also changed by $\sim 20 \text{ W/m}^2$, but with opposite sign (figure 4.30b). This thinning of the clouds has led to changes in LW too, where the LW down at the surface is decreased by $\sim 15 \text{ W/m}^2$ (figure 4.30c), and the LW up at TOA has increased by up to 5 W/m^2 (figure 4.30d). The increase in LW up at TOA is because of the increased surface temperature seen in figure 4.31c (recall Stefan-Boltzmann's law, equation 2.1).

The difference in surface heat fluxes is dominated by the removal of sea ice, see figures 4.31a and 4.31b. The reason for the patterns seen in those figures is that the removal of sea ice increases the surface temperature (figure 4.31c), which strengthens the temperature gradient between the surface and the overlying air. Thus the surface fluxes are increased where the sea ice has been removed. Just off the sea ice edge on the other hand there is a strong decrease in surface heat fluxes. This decrease is simply showing (compared to Control in figure 4.6) that there is not a pronounced increase in surface heat fluxes off the sea ice edge, now that the surface temperature is almost the same where there used to be sea ice, and just outside that area, giving a much smaller temperature gradient than in the control run, despite the strong winds. One may also recall the decrease in SH and skin temperature over the Canadian islands and Alaska, from increase in aerosol number concentration (figure 4.25) which is also noticeable in figures 4.31b and 4.31c.

The increase in surface heat fluxes and skin temperature (figure 4.31)

where the sea ice has been removed causes increased convection. Figure 4.32 shows LWC and temperature in the vertical cross section over the red line in figure 4.2d. There it is clear that the cloud base has been elevated due to the increased convection, compared to the control run (see figure 4.2c). The loss of liquid water near the mountain, is covered by the area of most pronounced decrease in LWP, indicated by the dark blue patch at 77°N 115-130°W.

Looking at the cross sections of LWC and temperature from Aero10NoIce and Control (figures 4.32 and 4.2c) one can also see that the temperature is higher in Aero10NoIce. Where there is most liquid water in Aero10NoIce the temperature is ~-8 to -9°C, whereas in Control it is ~-9 to -10°C. This contributes to an increase in downwelling LW at the surface (figure 4.30c).

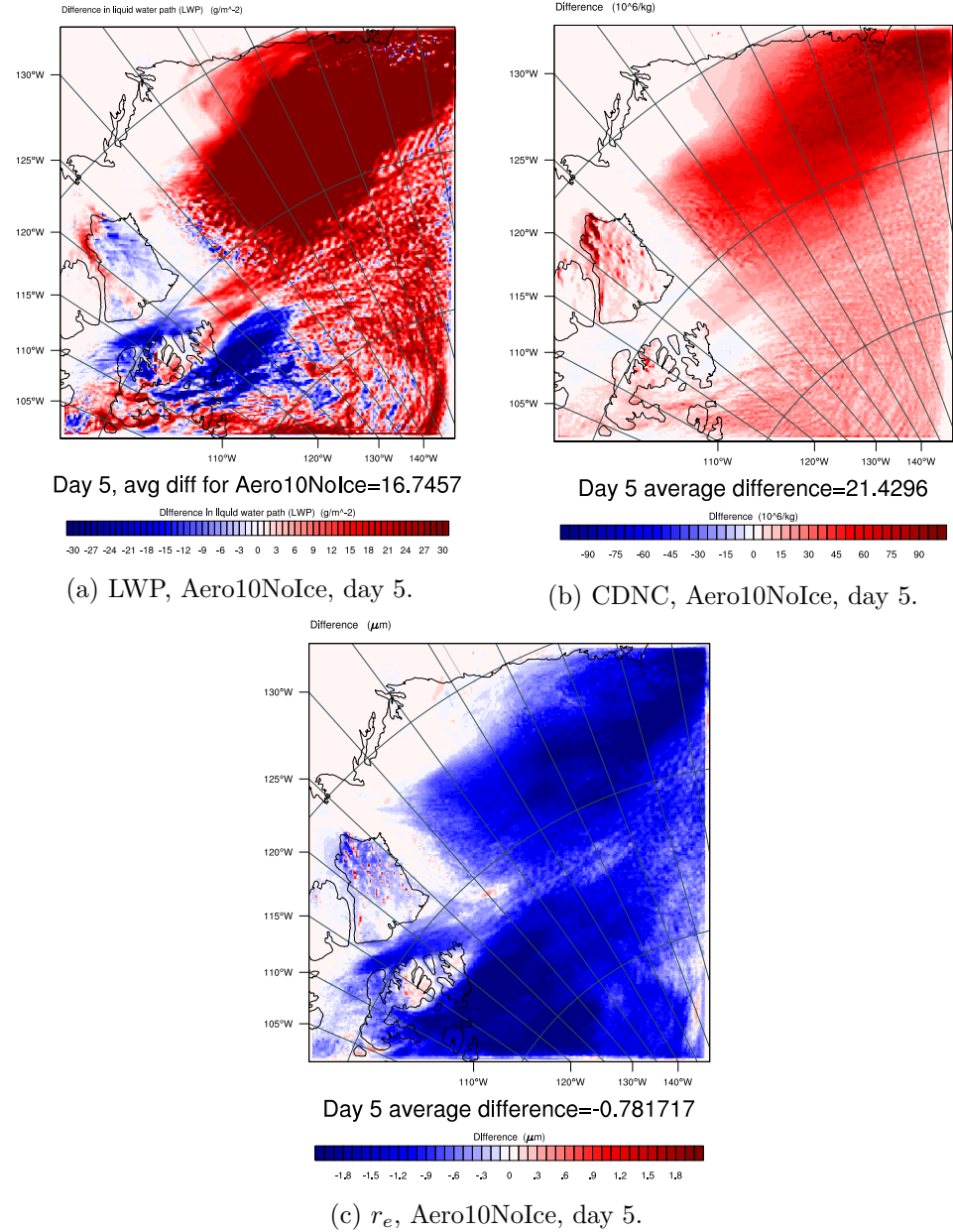


Figure 4.29: Difference in time averaged LWP, and in height and time averaged CDNC and r_e , for day 5. Aero10NoIce-Control.

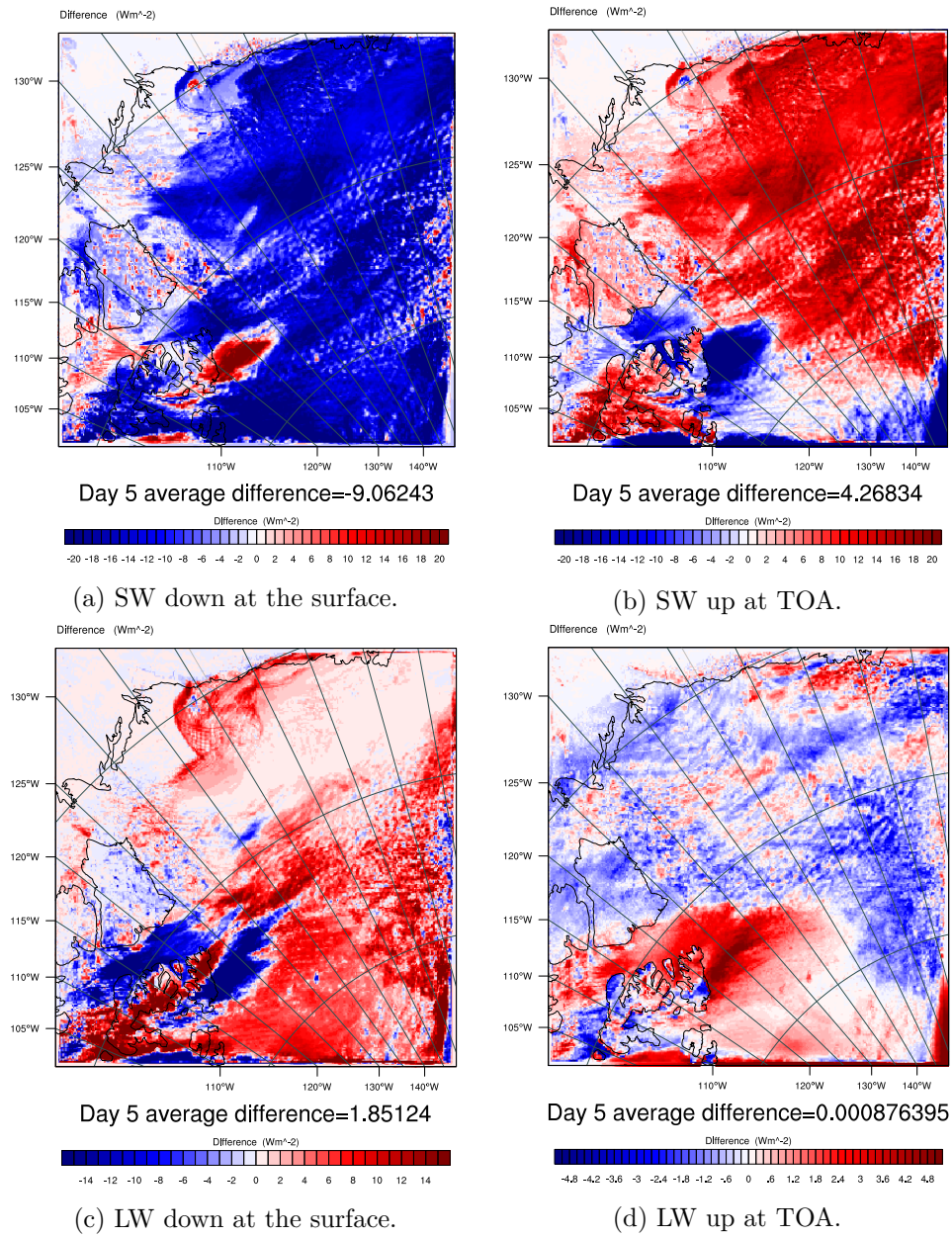


Figure 4.30: The average difference in SW and LW flux down at the surface and up at TOA, for day 5. Aero10NoIce-Control.
Notice the different scales.

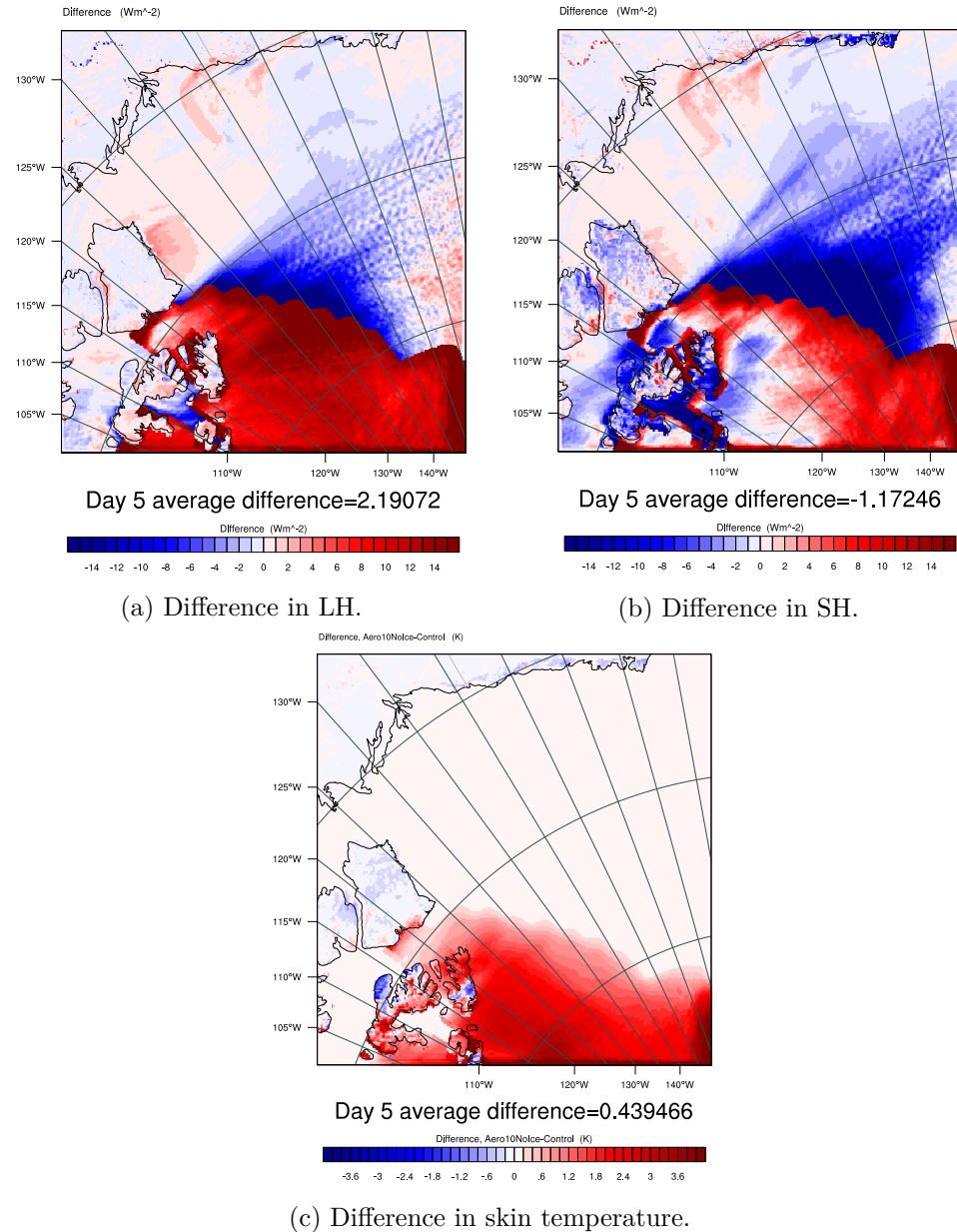


Figure 4.31: Average difference in LH and SH up at the surface, and difference in skin temperature, for day 5. Aero10NoIce-Control.

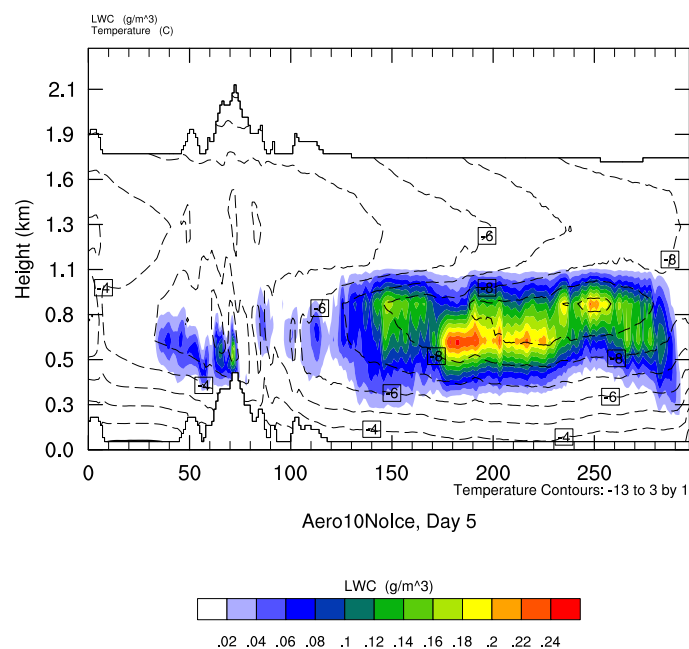


Figure 4.32: Time averaged LWC as filled contours, and temperature as dashed contours, in the vertical cross section over the red line in figure 4.2d. Day 5 of Aero10NoIce.

Chapter 5

Summary and concluding remarks

In this thesis the cloud radiative response to removal of sea ice and increased aerosol number concentration was studied by use of a formulation of the Weather Research and Forecasting (WRF) model called the Advanced Research WRF (ARW). The model was run for the first 5 days of September 2012, which is the most recent year of record low sea ice extent [NSIDC, 2015]. The model was run with and without sea ice, and with and without increased aerosol number concentration. The study area covers the Beaufort Sea, north of Canada and Alaska. The hypothesis was that there could be a positive feedback between the declining areal Arctic sea ice extent (eg. National Snow and Ice Data Center [NSIDC, 2015]) and radiative response of low Arctic stratus in autumn. Studies by Eastman & Warren [2010], Kay & Gettelman [2009], Palm *et al.* [2010] have found that the lack of sea ice in early autumn has led to an increase in low cloud amount. The question is then if these clouds have a warming effect at the surface. This could enhance sea ice melt and/or delay freezing, both of which would further decrease the sea ice extent.

The aforementioned studies did not look at the microphysical changes in the clouds, which has been the focus of this study. The response, and radiative effects of clouds to removal of sea ice and increased aerosol number concentration has been studied both separately and combined, for both the the first day of the run, which acts almost as an off-line run showing near instantaneous changes, and the last day of the run, when the atmosphere has had time to adapt to the changes implemented on the start of the first day.

Summary of results:

- Near instantaneous changes as a consequence of removed sea ice are increased surface heat fluxes, increased surface temperature and emission of water-friendly aerosols from the newly opened ocean. The

enhanced evaporation from the ocean together with convection leads to formation of new clouds, with small increases in liquid water path (LWP) (0.2 g/m^2) and cloud droplet number concentration (CDNC) (0.004 cm^{-3}). New clouds give increased downwelling LW radiation at the surface $\sim 0.27 \text{ W/m}^2$. The higher temperature of the surface increases the daily time averaged upwelling LW radiation at the top of the atmosphere (TOA) by 0.1 W/m^2 . Removing the sea ice significantly reduces the albedo, thus decreasing both upwelling SW at TOA, and downwelling SW at the surface, which is no longer reflected between sea ice at the surface and the clouds above.

- Near instantaneous changes as a consequence of increased aerosol number concentration are increased LWP (11 g/m^2) and CDNC (16 cm^{-3}) and decreased effective radius, r_e ($-0.5 \mu\text{m}$). The combination of increased CDNC and decreased r_e increases the cloud albedo, and is known as the first indirect effect. The increase in daily time averaged LWP indicates that the clouds are denser and longer lived, enhancing the reflectance of SW, which is known as the second indirect effect. The SW up at TOA is increased by 7.3 W/m^2 , and down at the surface it is reduced by 9.5 W/m^2 . The increase in LW down at the surface is 2.3 W/m^2 . Thus, the cooling effect by reduced downward SW wins over the warming effect from enhanced LW down at the surface. This is also seen in the decrease in temperature of the surface (skin temperature), -0.02°C , and reduction in sensible heat flux, -0.4 W/m^2 .
- When increase in aerosol number concentration and removal of sea ice is combined, the near instantaneous changes in LWP, CDNC and r_e are the same as when the sea ice is unchanged. The SW down at the surface is reduced by 11.6 W/m^2 , and up at TOA it is increased by 5.1 W/m^2 . Thus the combined removal of sea ice and increase in aerosols have a greater cooling effect at the surface through reduction in SW. On the other hand, the albedo of the ocean is significantly lower, meaning that more of the downward SW at the surface is absorbed, which has a warming effect.
- A few days after removal of the sea ice, the atmosphere has had time to adapt and in this study the increased surface temperatures and surface heat fluxes have made new clouds form. These clouds precipitate and also cause other clouds to precipitate leading to a reduction in LWP (-2.3 g/m^2), CDNC (-0.45 cm^{-3}) and r_e ($-0.16 \mu\text{m}$).
- The effect of increased aerosol number concentration after a few days is similar to the first day. The clouds are denser and longer lived, but the warming effect in LW (1.8 W/m^2) down at the surface is overpowered by the cooling effect in SW (-8.6 W/m^2) at the surface.

- When increase in aerosol number concentration and removal of sea ice is combined, the increase in LWP is still evident, but lower than for just the aerosol increase, 16.7 W/m^2 . This is because of the precipitation caused by convection due to increased surface temperatures and increased surface heat fluxes. The changes in radiation down at the surface is 1.8 W/m^2 in the LW, and -8.6 W/m^2 in the SW. Thus indicating a cooling effect at the surface.

In the results presented in this thesis the LWP in the control run was already high, with $40\text{-}150 \text{ g/m}^2$ for most of the study area and values up to 200 and 300 g/m^2 at the most. This means that the clouds were saturated with respect to LW radiation for much of the study area. Thus the warming effect from enhanced downwelling LW radiation is overpowered by the cooling effect by reflection of SW radiation. Therefore a positive feedback between Arctic stratus and changes in Arctic sea ice extent can not be confirmed based on this study.

Using a weather research model, as opposed to a climate model, allows for a detailed study of the low clouds, with high resolution both in the horizontally and vertically. This resolution is also better than many observations. Although there have been field campaigns focusing on clouds (see Chapter 1), observations in the Arctic can be challenging and costly, due to a long dark season and a lot of open water, often meaning that air planes or ships must be involved in collecting the data. When that is said, observations do at least show real life changes, whereas a model can only simulate the changes.

Bibliography

- Aguado, Edward, & Burt, James E. 2010. *Understanding Weather and Climate*. 5th edn. Pearson Prentice Hall.
- Albrecht, Bruce A. 1989. Aerosols, Cloud Microphysics, and Fractional Cloudiness. *Science*, **245**(4923), 1227–1230.
- Alterskjaer, K., Kristjánsson, J. E., & Hoose, C. 2010. Do anthropogenic aerosols enhance or suppress the surface cloud forcing in the Arctic? *Journal of Geophysical Research: Atmospheres*, **115**(22), 1–19.
- Curry, Judith A., Schramm, J L, & Ebert, E E. 1995. *Sea-Ice Albedo Climate Feedback Mechanism*.
- Curry, Judith A., Schramm, Julie L., Rossow, William B., & Randall, David. 1996. Overview of Arctic Cloud and Radiation Characteristics. *Journal of Climate*, **9**(8), 1731–1764.
- Curry, Judith A., Hobbs, P. V., King, M. D., Randall, D. A., Minnis, P., Isaac, G. A., Pinto, J. O., Uttal, T., Bucholtz, A., Cripe, D. G., Gerber, H., Fairall, C. W., Garrett, T. J., Hudson, J., Intrieri, J. M., Jakob, C., Jensen, T., Lawson, P., Marcotte, D., Nguyen, L., Pilewskie, P., Rangno, A., Rogers, D. C., Strawbridge, K. B., Valero, F. P J, Williams, A. G., & Wylie, D. 2000. FIRE arctic clouds experiment. *Bulletin of the American Meteorological Society*, **81**(1), 5–29.
- Eastman, Ryan, & Warren, Stephen G. 2010. Interannual variations of arctic cloud types in relation to sea ice. *Journal of Climate*, **23**(15), 4216–4232.
- Eckhardt, S., Hermansen, O., Grythe, H., Fiebig, M., Stebel, K., Cassiani, M., Baecklund, a., & Stohl, a. 2013. The influence of cruise ship emissions on air pollution in Svalbard – a harbinger of a more polluted Arctic? *Atmospheric Chemistry and Physics*, **13**(16), 8401–8409.
- ECMWF. 2015. *European Centre for Medium-Range Weather Forecasting*.
- Graversen, Rune G, Mauritsen, Thorsten, Tjernström, Michael, Källén, Erland, & Svensson, Gunilla. 2008. Vertical structure of recent Arctic warming. *Nature*, **451**(7174), 53–56.

- Grell, Georg a. 2002. A generalized approach to parameterizing convection combining ensemble and data assimilation techniques. *Geophysical Research Letters*, **29**(14), 10–13.
- Hansen, J. E., & Travis, L. D. 1974. Light scattering in planetary atmospheres. *Space Science Reviews*, **16**(1957), 527–610.
- Herman, G. F. 1980. Thermal radiation in Arctic stratus clouds. *Quarterly Journal of the Royal Meteorological Society*, **106**(450), 771–780.
- Hobbs, Peter V. 1993. *Aerosol-Cloud-Climate Interactions*. Academic Press.
- Hong, Song Y., & Dudhia, Jimy. 2004. Testing of a new nonlocal boundary layer vertical diffusion scheme in numerical weather prediction applications. *Bulletin of the American Meteorological Society*, **2**(1), 2213–2218.
- Iacono, Michael J. 2003. Evaluation of upper tropospheric water vapor in the NCAR Community Climate Model (CCM3) using modeled and observed HIRS radiances. *Journal of Geophysical Research*, **108**(D2).
- Iacono, Michael J., Mlawer, Eli J., Clough, Shepard a., & Morcrette, Jean-Jacques. 2000. Impact of an improved longwave radiation model, RRTM, on the energy budget and thermodynamic properties of the NCAR community climate model, CCM3. *Journal of Geophysical Research*, **105**(D11), 14873.
- Iacono, Michael J., Delamere, Jennifer S., Mlawer, Eli J., Shephard, Mark W., Clough, Shepard a., & Collins, William D. 2008. Radiative forcing by long-lived greenhouse gases: Calculations with the AER radiative transfer models. *Journal of Geophysical Research: Atmospheres*, **113**(13), 2–9.
- Kay, Jennifer E., & Gettelman, Andrew. 2009. Cloud influence on and response to seasonal Arctic sea ice loss. *Journal of Geophysical Research D: Atmospheres*, **114**(18).
- Klein, S. A., & Hartmann, D. L. 1993. The seasonal cycle of low stratiform clouds. *Journal of Climate*, **6**, 1587–1606.
- Liou, K. N. 1992. *Radiation and Cloud Processes in the Atmosphere*. Oxford University Press.
- Liou, K. N. 2002. *An Introduction to Atmospheric Radiation*. 2nd edn. Academic Press.
- Lohmann, U., & Feichter, J. 2005. Global indirect aerosol effects: a review. *Atmospheric Chemistry and Physics Discussions*, **4**(6), 7561–7614.

- Martin, G. M., Johnson, D. W., & Spice, A. 1994. The Measurement and Parameterization of Effective Radius of Droplets in Warm Stratocumulus Clouds. *Journal of the Atmospheric Sciences*, **51**(13), 1823–1842.
- McDonald, James E. 1958. *The Physics of Cloud Modification*.
- Mlawer, Eli J., Taubman, Steven J., Brown, Patrick D., Iacono, Michael J., & Clough, Shepard a. 1997. Radiative transfer for inhomogeneous atmospheres: RRTM, a validated correlated-k model for the longwave. *Journal of Geophysical Research*, **102**(D14), 16663.
- NSIDC. 2015. *National Snow and Ice Data Center*.
- Palm, Stephen P., Strey, Sara T., Spinhirne, James, & Markus, Thorsten. 2010. Influence of Arctic sea ice extent on polar cloud fraction and vertical structure and implications for regional climate. *Journal of Geophysical Research*, **115**(D21), D21209.
- Reisner, J., Rasmussen, R M., & Bruintjes, R T. 1998. Explicit forecasting of supercooled liquid water in winter storms using the MM5 mesoscale model. *Quarterly Journal of the Royal Meteorological Society*, **124**(548), 1071–1107.
- Rogers, R. R., & Yau, M. K. 1989. *A Short Course in Cloud Physics*. 3rd edn. Butterworth-Heinemann.
- Schweiger, Axel J., Lindsay, Ron W., Vavrus, Steve, & Francis, Jennifer A. 2008. Relationships between Arctic Sea Ice and Clouds during Autumn. *Journal of Climate*, **21**(18), 4799–4810.
- Screen, James A., & Simmonds, Ian. 2010. The central role of diminishing sea ice in recent Arctic temperature amplification. *Nature*, **464**(7293), 1334–1337.
- Shupe, Matthew D., & Intrieri, Janet M. 2004. Cloud radiative forcing of the Arctic surface: The influence of cloud properties, surface albedo, and solar zenith angle. *Journal of Climate*, **17**(3), 616–628.
- Skamarock, W.C., Klemp, J.B., Dudhia, J., Gill, D.O., Barker, D.M., Duda, M.G., Huang, X.-Y., Wang, W., & Powers, J.G. 2008. A Description of the Advanced Research WRF Version 3. *Technical Report*, 113.
- Skamarock, William C., & Klemp, Joseph B. 2008. A time-split nonhydrostatic atmospheric model for weather research and forecasting applications. *Journal of Computational Physics*, **227**(7), 3465–3485.
- Stevens, Bjorn, & Feingold, Graham. 2009. Untangling aerosol effects on clouds and precipitation in a buffered system. *Nature*, **461**(7264), 607–613.

- Stevens, Björn, & Seifert, Axel. 2008. Understanding macrophysical outcomes of microphysical choices in simulations of shallow cumulus convection. *Journal of the Meteorological Society of Japan*, **86A**(August 2006), 143–162.
- Tewari, Mukul, Chen, F., Wang, W., Dudhia, J., LeMone, M. A., Mitchell, K., Ek, M., Gayno, G., Wegiel, J., & Cuenca, R. H. 2004. Implementation and verification of the unified NOAH land surface model in the WRF model. *Pages 11–15 of: 20th conference on weather analysis and forecasting/16th conference on numerical weather prediction*.
- Thompson, Gregory, & Eidhammer, Trude. 2014. A study of aerosol impacts on clouds and precipitation development in a large winter cyclone. *Journal of the Atmospheric Sciences*, 140507124141006.
- Thompson, Gregory, Rasmussen, Roy M., & Manning, Kevin. 2004. Explicit Forecasts of Winter Precipitation Using an Improved Bulk Microphysics Scheme. Part I: Description and Sensitivity Analysis. *Monthly Weather Review*, **132**, 519–542.
- Thompson, Gregory, Field, Paul R., Rasmussen, Roy M., & Hall, William D. 2008. Explicit Forecasts of Winter Precipitation Using an Improved Bulk Microphysics Scheme. Part II: Implementation of a New Snow Parameterization. *Monthly Weather Review*, **136**, 5095–5115.
- Twomey, S. 1974. Pollution and the Planetary Albedo. *Atmospheric Environment*, **8**, 1251–1256.
- Twomey, S. 1977. The Influence of Pollution on the Shortwave Albedo of Clouds. *Journal of the Atmospheric Sciences*, **34**, 1149–1152.
- UCAR. 2015. *Home page for NCAR Command Language*.
- Uttal, Taneil, Curry, Judith A., Mcphee, Miles G., Moritz, Donald K. Perovich Richard E., Maslanik, James A., Guest, Peter S., Stern, Harry L., Moore, James A., Turenne, Rene, Heiberg, Andreas, Serreze, Mark. C., Wylie, Donald P., Persson, Ola G., Paulson, Clayton A., Halle, Christopher, Morison, James H., Wheeler, Patricia A., Makshtas, Alexander, Welch, Harold, Shupe, Matthew D., Intrieri, Janet M., Stamnes, Knut, Lindsey, Ronald W., Pinkel, Robert, Pegau, W. Scott, Stanton, Timothy P., & Grenfeld, Thomas C. 2002. Surface heat budget of the Arctic Ocean. *Bulletin of the* ..., 255–276.
- Vavrus, Steve, Holland, Marika M., & Bailey, David A. 2010. Changes in Arctic clouds during intervals of rapid sea ice loss. *Climate Dynamics*, **36**, 1475–1489.

- Verlinde, J., Harrington, J. Y., McFarquhar, G. M., Yannuzzi, V. T., Avramov, a., Greenberg, S., Johnson, N., Zhang, G., Poellot, M. R., Mather, J. H., Turner, D. D., Eloranta, E. W., Zak, B. D., Prenni, a. J., Daniel, J. S., Kok, G. L., Tobin, D. C., Holz, R., Sassen, K., Spangenberg, D., Minnis, P., Tooman, T. P., Ivey, M. D., Richardson, S. J., Bahrmann, C. P., Shupe, M., DeMott, P. J., Heymsfield, a. J., & Schofield, R. 2007. The mixed-phase arctic cloud experiment. *Bulletin of the American Meteorological Society*, **88**(2), 205–221.
- Wallace, John M., & Hobbs, Peter V. 2006. *Atmospheric Science, An Introductory Survey*. 2nd edn. Academic Press.
- Wang, Wei, Bruyère, Cindy, Duda, Michael, Dudhia, Jimy, Gill, Dave, Kavulich, Michael, Keene, Kelly, Lin, Hui-Chuan, Michalakes, John, Rizvi, Syed, Zhang, Xin, Berner, Judith, & Smith, Kate. 2015. *WRF ARW Version 3 Modeling System User's Guide*. Mesoscale & Microscale Meteorology Division, National Centre for Atmospheric Research.
- Wu, Dong L., & Lee, Jae N. 2012. Arctic low cloud changes as observed by MISR and CALIOP: Implication for the enhanced autumnal warming and sea ice loss. *Journal of Geophysical Research: Atmospheres*, **117**(D7).